Master Thesis

Structural design of a VTOL twin-tiltwing drone concept with a distributed hybrid electric propulsion system.

R. Boerma

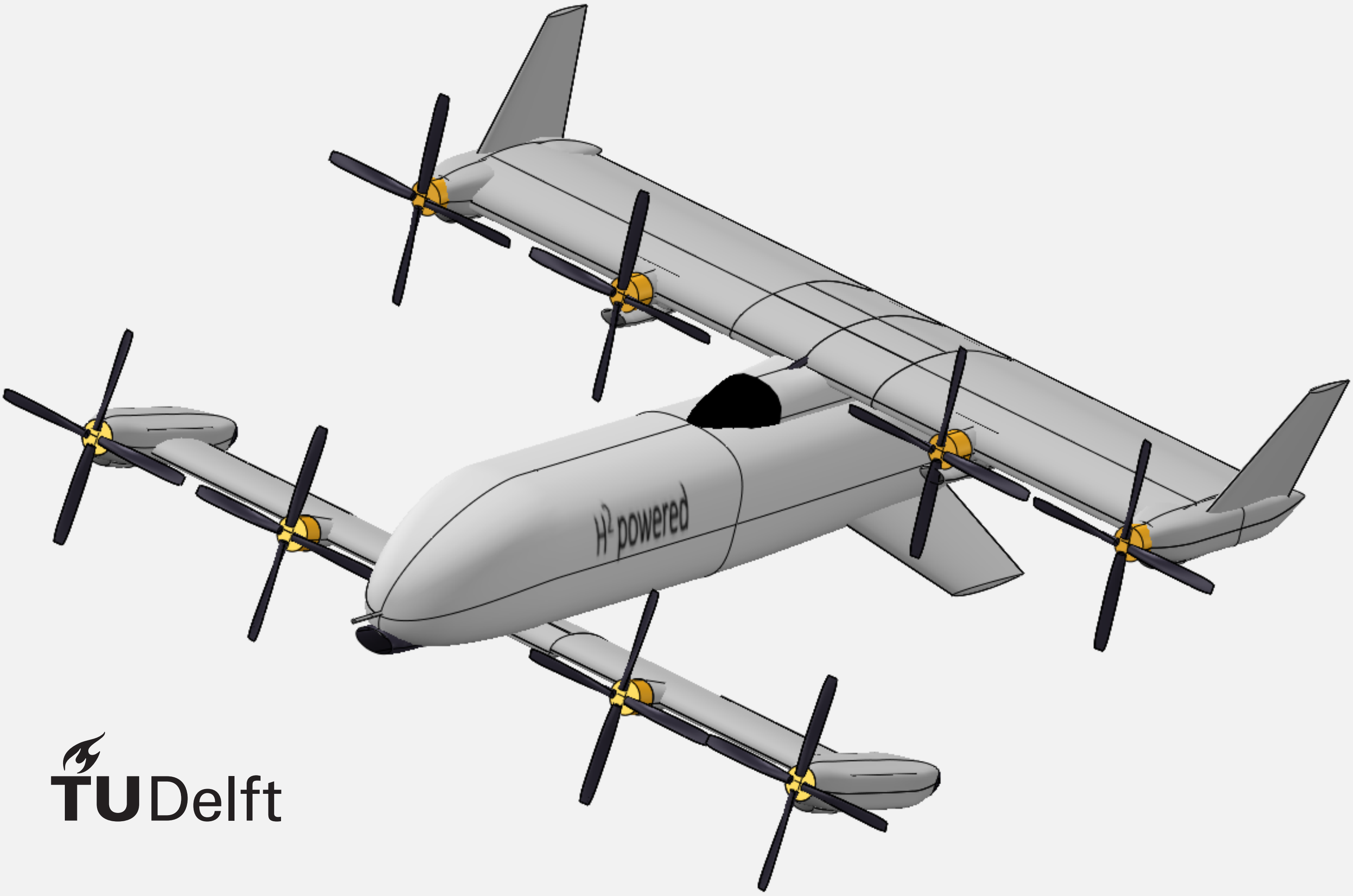

TU Delft

Master Thesis

Structural design of a VTOL twin-tiltwing drone concept with a distributed hybrid electric propulsion system.

by

R. Boerma

in partial fulfilment of the requirements for the degree of

Master of Science

in Aerospace Structures and Materials

at the Delft University of Technology.

to be defended publicly on April 17, 2020 at 13:30

Thesis committee:	Prof. C.A. Dransfeld	TU Delft
	Ir. J. Sinke,	TU Delft
	Dr. Ir. O.K. Bergsma	TU Delft
	Ing. W. van de Waerdt,	Fokker Aerostructures
Supervisors:	Ir. J. Sinke,	TU Delft
	Ing. W. van de Waerdt,	Fokker Aerostructures
	Ing. P. Lantermans,	HyFly

This thesis is confidential and cannot be made public until April 17, 2023.

TU Delft

Preface

During my internship at Fokker Aerostructures I was lucky enough to be working on an internal challenge design challenge set out by the CTO of GKN Aerospace. The challenge was to design a vehicle capable of VTOL operations with a payload and range capability of 100 kg and 100 km respectively, while not exceeding a 5 meter span and length. The design was partially successful as team was declared as one of the propulsion group winners for the proposed hydrogen fuel cell based system. Contrary to my studies, where I focus on aircraft structures, my job was to estimate the performance of the concept. This gave me in-depth insight in the performance of tandem wing VTOL aircraft. After my internship I was able to further investigate the structural requirements for a scaled down proof-of-concept version as part of my final thesis.

I am very grateful that I was allowed to work on both the performance estimation, and the design of proof-of-concept under the wing of Fokker Aerostructures. I would specifically like to thank my supervisor Wydo van de Waerdt, Pieter Lantermans and Andries Buitenhuis for this great opportunity. Furthermore I would like to express my gratitude towards Luuk Koster and Sander Luders, who helped me with the production of the material test samples and the material testing respectively. I would like to thank Peter Koning and my fellow students for the great working atmosphere. I also would like to thank my parents for their patience and their support during my studies.

With this thesis I end my studies at the Delft University of Technology in the field of Aerospace Engineering & Aerospace Structures and Materials. During this time, and my time at the student foundation Lambach Aircraft in particular, my interest in aircraft design grew to new highs. For this I am forever grateful, and I look forward to the future in which I will be working on some cool sustainable aviation projects. Such as the continuation of the hybrid VTOL cargo drone and the development of an electric race aircraft.

R. Boerma
Hoogeveen, April 2020

Contents

List of Figures

List of Tables

Nomenclature

List of symbols

Symbol Latin	Definition	Unit
A	Area	[mm^2]
b	Wingspan	[m]
b	Wingbox width	[mm]
c	Chord length	[mm]
C	Coefficient	[-]
d	Distance	[m]
E	Young modulus	[GPa]
F	Force	[N]
G	Shear modulus	[GPa]
GK	Torsional Stifnness	[Nmm^2]
g_0	Gravitational constant	[m/s^2]
h	Height	[m] [mm]
I	Second moment of inertia	[mm^4]
k	spring stiffness	[N/m]
l	length	[m]
L	Length	[mm]
M	Moment	[Nm]
N	distributed load	[N/mm]
Q	First moment of area	[mm^3]
R	Range	[km]
Re	Reynolds number	[-]
RF	reserve factor	[-]
S	Shear strength	[MPa]
S$_{max}$	Maximum shear force	[N]
T	Torsion	[Nm]
T	Thrust	[N]
T	Torsion ratio	[-]
t	thickness	[mm]
V	Speed	[m/s]
W	Weight	[kg] or [N]
W	Width ratio	[-]
X	Strength in x-direction	[MPa]
Y	Strength in y-direction	[MPa]

List of symbols

Subscripts

Coefficients

Abbreviations

Symbol Greek	**Definition**	**Unit**
α	Angle of attack	[deg] or [rad]
Δ	Change or deflection	- or [deg]
δ	displacement	[mm]
ϵ	Strain	[-]
θ	Angle	[deg]
κ	Curvature	[1/deg]
ν	Poisson' ratio	[-]
γ	Shear strain	[-]
ρ	Density	[kg/m^3]
σ	Stress	[MPa]
τ	Shear stress	[MPa]
ϕ	Angle	[deg]

Symbol	**Definition**
ail.defl	Aileron deflection
c	Canard
c	Compressive
c	Core
cg	Centre of gravity
cr	critical
d	drag
f	facesheet
i	iterator
m	Moment
n	normal load
pl	Payload
r	Resultant
s	Stall
SC	Shear centre
t	Tensile
w	Wing

Symbol	**Definition**
$C_{cl_{maxps}}$	maximum post stall lift coefficient
C_D	Drag coefficient
$C_{D_{max_{poststall}}}$	Maximum post stall drag coefficient
C_L	Lift coefficient
C_{L_0}	Zero angle of attack lift coefficient
$C_{L_{max}}$	Maximum lift coefficient
$C_{l_{max_{poststall}}}$	Maximum post stall lift coefficient
C_m	Moment coefficient
C_R	Resultant coefficient

Symbol	**Definition**
ASTM	American Society for Testing and Materials
BID	Bi-direction ply or weave
BVLOS	Beyond Visual Line of Sight
CFD	Computational Fluid Dynamics
CofA	Certificate of airworthiness
CNC	Computer Numerical Control
CS-LUAS	Certification Specifications for Light Unmanned Aeroplane Systems
CS-LURS	Certification Specifications for Light Unmanned Rotorcraft Systems
CS-UAS	Certification Specifications for Unmanned Aircraft Systems
CTO	Chief Technology Officer
EASA	European Aviation Safety Agency
EPS	Expanded Polystyrene
EU	European Union
IL&T	Inspectie Leefomgeving & Transport
IML	Inner Mould Line
JARUS	Joint Authorities for Rulemaking on Unmanned Systems
HS	High Strength
MS	Margin of Safety
MTOM	Maximum Take-Off Mass
MTOW	Maximum Take-Off Weight
NAA	National Aviation Authorities
NACA	National Aeronautics Committee for Aeronautics
NASA	National Aeronautics and Space Administration
OEW	Operating Empty Weight
OML	Outer Moldline
PET	Polyethylene terephthalate
PMI	Polymethalcrylimidi
PUR	Polyurethane
PVC	Polyvinyl Chloride
ROC	RPAS Operator Certificate
RPA	Remoetely Piloted Aircraft
RPAS	Remotely Piloted Aircraft Systems
SAN	Styrene acrylonitrile
SF	Safety Factor
UAS	Unmanned Aircraft Systems
UHM	Ultra High Modulus
UND	Uni-directional ply or weave with the majority of fibres in the 0 direction
SORA	Specific Operations Risk Assesment
VLOS	Visual Line Of Sight
VTOL	Vertical Take-off and Landing
XPS	Extruded Polystyrene

1

Introduction

The drive for both manned and unmanned sustainable aviation is fuelled by the concern of global warming. In the urban air-mobility and UAV industry the focus on building a sustainable platform is almost adopted industry wide. However most concepts solely focus on battery powered vehicles which rely on the thrust produced by their rotors to stay airborne. As part of the CTO challenge of GKN Aerospace a VTOL tandem tiltwing drone concept with a distributed hybrid electric propulsion system capable of carrying a 100 kilogram payload was designed by a team of Fokker Aerostructures Hoogeveen employees. The use of a tandem tiltwing configuration enables the drone to take off vertically like a quadcopter and cruise like a conventional canard aircraft. The benefit of this configuration is that the functions of lift and thrust generation are separated such that both can be optimized and that a higher range and better cruise performance can be achieved while still having a small wingspan which is beneficial for landing in urban areas. Incorporating a hydrogen-electric propulsion system improves the systems energy density and hence improves the range considerably. A small scale 50 kilogram prototype will be designed which will be used to validate the feasibility of the concept.

As with all aircraft, but especially for vertical take-off vehicles, the penalty for weight is at a premium. The distributed hybrid-electric propulsion system in combination with a tandem tiltwing configuration has a profound effect on the structure aircraft. The design of the concept vehicle integrates the propulsion system into the structure such that the best compromise is found between aircraft performance, weight and system integration. The objective of this thesis is to design a structure for the drone prototype by analysing the expected loads and manufacturing concepts available and by performing a strength analysis on the designed geometry such that the structure will not fail under the expected loads. This thesis selects the best structural design based on a qualitative analysis. In order to perform the strength analysis on the structure of the vehicle, a large number of topics will have to detailed such as manufacturability, material choice, structural design and certification specifications will have to be taken into account. See figure 1.1 for a graphical overview of the content.

The background information on the vehicle concept and the initial design of the prototype is presented chapter 2 and 3. Chapter 4 describes the available construction and manufacturing techniques that could be used for the construction of the prototype. The structural design, i.e. the layout of the structure and components, is detailed in chapter 5. Chapter 6 describes the material choice and the material testing performed on test samples. Next the loads that can be expected on the airframe during the different flight phases (hover, transition, cruise and landing) are determined in chapter 8. With the loads, the materials and structural layout known, the structural analysis of

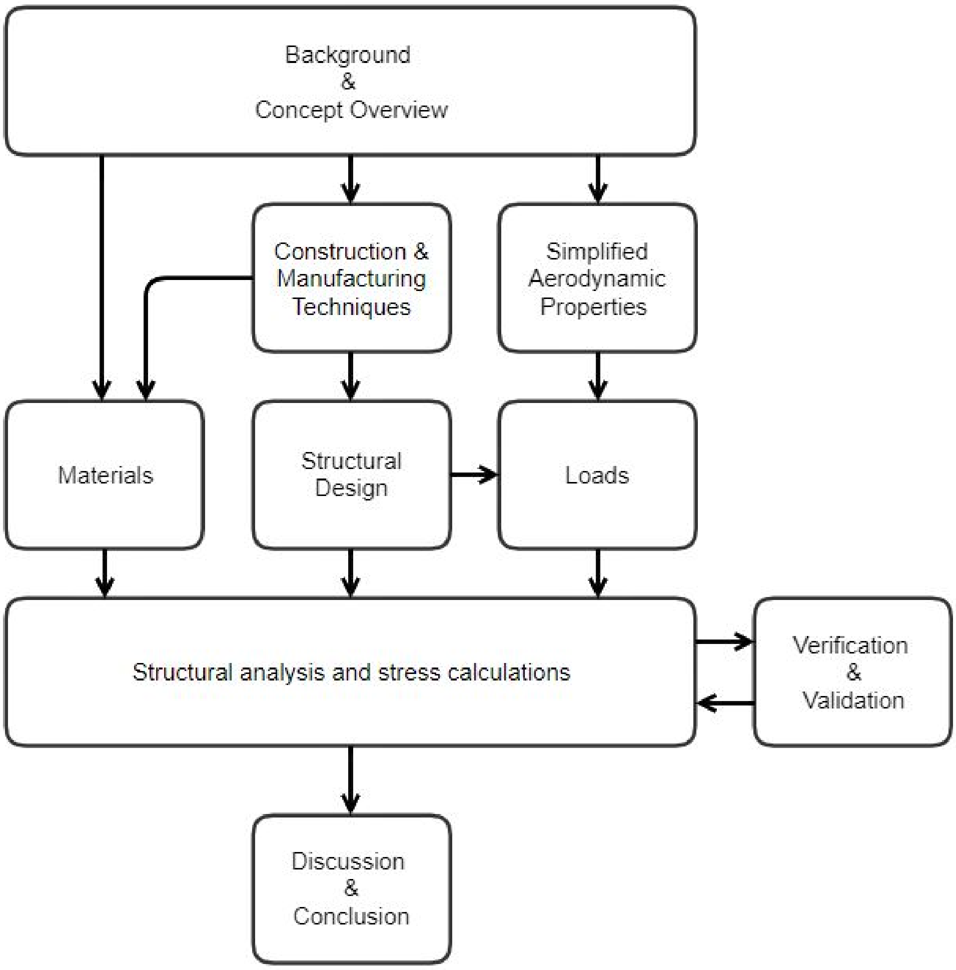

Figure 1.1: Report overview

the vehicle can be performed in chapter 9. For the structural analysis a tool is developed to analyse multiple load cases in order to analyse and determine the final wing layup. In chapter 10 the developed tool is verification and validation after which the discussion and conclusion end this thesis report.

2

Background

This chapter presents the reader with background information on the project. In section 2.1 a brief summary is given on the project and how it came about. Section 2.2 covers the background of tiltwing and reference aircraft. An important consideration in the design of a vehicle and its structure is the certification, as this will determine how it will be proven that the structure is safe for its intended purpose, this is detailed in section 2.3. The final section of this chapter presents the objective of this thesis and the accompanying research questions.

2.1. Background information

As part of the CTO challenge of GKN Aerospace a VTOL tiltwing drone concept with a distributed hybrid electric propulsion system capable of carrying a 100 kilogram payload was designed by a team of Fokker Aerostructures Hoogeveen. I assisted the team, as part of my internship, by developing a tool for the performance analysis of the concept. A further investigation of the concept beyond the challenge was started by developing a 5.2 kW prototype to prove the feasibility of the concept.

2.2. Reference aircraft

This section describes the aircraft that share similarities with the proposed concept. The first section describes the conventional tiltwing aircraft followed by a section on tandem tiltwing reference aircraft. These reference aircraft can be used to find literature concerning the research. Tilt rotor reference vehicles are not considered.

2.2.1. ’Conventional’ tiltwing aircraft

The concept of an aircraft with a single tiltwing in conjunction with a conventional tail exists already for a while. The idea of a tiltwing dates back from before the second World War, when in 1938 the Zhuchenko Vertoplane was built. However the next year when the aircraft was tested it hardly took off and due to the start of the second World War further development was cancelled[1].

It took until the 1950s for tiltwing aircraft to take-off, when the Vertol model 76 VZ-2 was designed for the U.S. Army. The first flight of the aircraft was made in 1957 and the first transition from vertical flight to horizontal flight was made on the 15th of June 1958 [33]. A list of tilt wing aircraft that have flown and the year of introduction can be found below:

• 1939 - Zhuchenko Vertoplan[1]	see figure 2.1
• 1957 - Vertol VZ-2 [33]	see figure 2.2

---

[1] Zhuchenko Vertoplan `https://sites.google.com/site/stingrayslistofrotorcraft/zhuchenka-vertoplan`

• 1959 - Hiller X-18 [33]	see figure 2.3
• 1964 - LTV/Hiller/Ryan XC-142A [33]	see figure 2.4
• 1974 - Canadair CL-84 [33],	see figure 2.5
• 2014 - NASA Langley GL-10 Greased Lightning,	see figure 2.6

Figure 2.1: Zhuchenko Vertoplan, 1939

Figure 2.2: Vertol VZ-2 Model 76, 1957

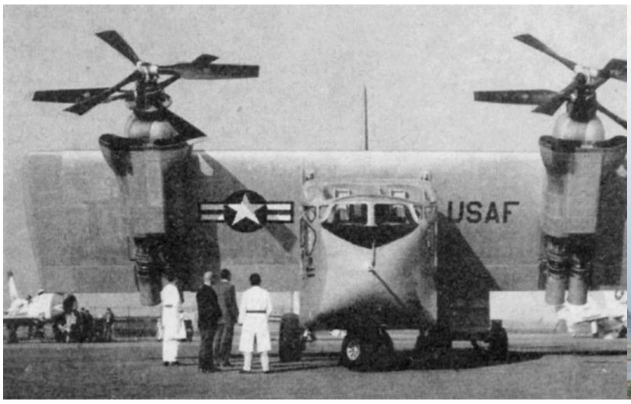

Figure 2.3: Hiller X-18, 1959

Figure 2.4: Ling-Temco-Vought XC142A, 1964

Figure 2.5: Canadair CL-84, 1974

Figure 2.6: NASA Greased Lightning GL10, 2014

As can be seen in the list above, a large gap is present from the 1974 until 2014. This gap can be explained due to the success of the tiltrotors in the form of the Bell-Boeing V22 Osprey and its predecessor the Bell XV-15. In this time also the Harrier was designed, one of the few successful VTOL jet fighters. The main advantage of a tiltrotor over a tiltwing aircraft is better hover performance.

This can be accounted to the larger rotors used on tiltrotor versus tiltwing. A tiltwing however is usually able to land like a conventional aircraft while tiltrotor aircraft usually cannot due to their large rotors. The tiltrotor is limited in maximum speed however, as its large rotor diameter causes the tip speed of the blade to be close to the speed of sound at relatively low airspeeds.

2.2.2. Tandem tiltwing aircraft

In the 2000's with the rise of cheap artificial stabilization, the first electric quadcopters were built. Many different new configurations and prototypes spun off by this technology. The concept of a tandem tiltwing can be seen as a combination between a tiltwing aircraft and the quadcopter. The first technical report of a tandem tiltwing was by the Japan Aerospace Exploration Agency with their QUX-02 quad tilt wing aircraft, which flew for the first time in 2008 [31]. The QUX-02, see figure 2.7, still had a conventional tail next to the two tilting wings. In 2010 the Sabanci University (Turkey) also created a quad tilt wing, the SUAVI [12]. The SUAVI, see figure 2.8, did not have tail surfaces. All control was performed by the engine trust and the tilting of the wings.

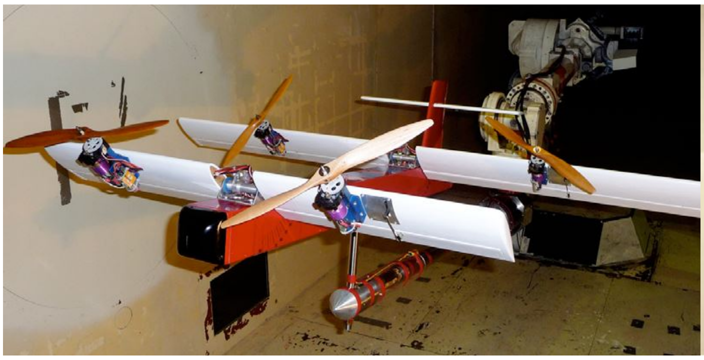

Figure 2.7: JAXA's QUX-02 in the windtunnel [31]

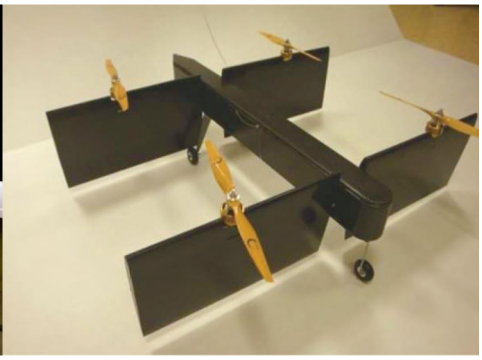

Figure 2.8: SUAVI, 2010. [12]

The Airbus Vahana is the first full size tandem tiltwing aircraft that took flight (on 31 January 2018)[2]. The Vahana, figure 2.9, is fully electric. The Beta Technologies AVA XC also took first flight in 2018 and it a combination between a tiltwing and a conventional aircraft as it has a fixed wing and tail, combined with two rotating boom on which the motors are located. The AVA XC is the only tiltwing concept that was piloted. The final tandem tiltwing aircraft is the NASA Langley Aerodrome #8 which is still in development. A summary of all the tandem tiltwing aircraft:

Figure 2.9: Airbus Vahana, 2018

Figure 2.10: Beta Technologies AVA XC, 2018

- 2008 - JAXA (Japan Aerospace Exploration Agency) QUX-02 [31] see figure 2.7
- 2010 - Sabanci University Unmanned Aerial VehIcle (SUAVI) [12] see figure 2.8

- 2018 - Airbus Vahana [2] see figure 2.9
- 2018 - Beta Technologies AVA XC - [3] see figure 2.10
- 2019 - NASA Langley Aerodrome #8, [4] see figure 2.11

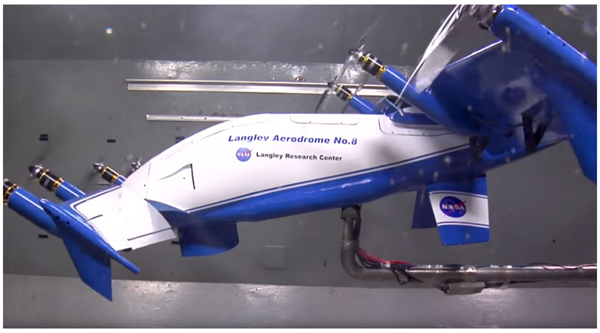

Figure 2.11: NASA Langley Aerodrome #8, not flown yet.

All of the tandem tiltwing aircraft above are fully electric,in contrary to the older tiltwing aircraft which are all powered by reciprocating or by turboprop engines.

2.2.3. Structures

Looking at the reference aircraft two main structural configurations can be seen. The conventional tilt wing aircraft, except for the Vertoplan, have a continuous wing box structure. While the most tandem tilt wing configurations, which all are smaller vehicles, such as the Airbus Vahana and the NASA LA-8 only have a continuous spar-tube on which the wing hinges.

Having a continuous wing box is structurally more efficient as only shear loads or a differential moment need to be transferred to the fuselage. Depending on the internal geometry the of the spar-tube the moment remains in the tube or needs to be transferred from the left to the right tube. The wing box can be made larger than the spar-tube which increases the inertia and hence reduces bending loads. To increase the height of the spar-tubes a larger and more heavy hinge needs to be selected.

2.3. Certification

Each aircraft requires a certificate of airworthiness in order to be allowed to fly. As drones are being used more and more for commercial use there is a need for European wide regulation and certification. However the regulations of drones are lagging behind on the technology that is currently available. This chapter presents a brief summary on the certification of drones and what rules can be expected to be put into place in the upcoming years. These rules are important as they dictate what certifications specification the drone must comply with. This selected regulation in this chapter determine the load cases that must be analysed, see chapter 8.

In the current state the rules of the National Aviation Authorities (NAA) apply, this is detailed in section 2.3.1. The applicable rules that are proposed by the European Aviation Safety Agency (EASA) are detailed in section 2.3.2. The last section (2.3.3), on the certification and rule-making regarding drones, covers the Joint Authorities for Rulemaking on Unmanned Systems (JARUS). Jarus is an international body consisting of NAA's and experts who propose rule-making for countries to implement. Looking at the JARUS documents gives an indication of the upcoming regulations that can be expected within Europe. The final section 2.3.4 summarizes the regulations presented and

---

[2] Airbus Vahana first flight: `http://www.vahana.aero/vahanas-first-flight-a-success-ade26d26ba02`

[3] Online article by thedrive.com

[4] `https://www.nasa.gov/feature/langley/langley-aerodrome-created-to-explore-urban-air-mobility`

proposed how to use these regulations in the design of the prototype.

2.3.1. Dutch regulations

At the moment of writing, September 2019, the legislation by the Dutch NAA is still in effect. Hence up until the moment that the European legislation come into effect the Dutch law on Remotely Piloted Aircraft Systems (RPAS) will be leading. This regulation is the "Regeling op afstand bestuurde luchtvaartuigen"[5] (Regulation remotely piloted aircraft). To pilot a RPAS between the mass of 25 and 150 kilogram a special licence has to be obtained called the RPAS Operator Certificate (ROC) or the RPA-L. A list of operation limitations applies to the (commercial) RPAS operator. Since the operation is not of interest in this research no further details are elaborated upon.

The RPAS itself also has to comply to regulations as well. A special Certificate of Airworthiness (S-CofA or S-BvL in Dutch) is required for the RPAS itself. In comparison to Experimental aircraft (which also require a S-CofA) the requirements for the RPAS are much more simplified for this weight category up to 150 kilograms. For the approval of the RPAS, only a statement of an accepted company is required that states that the RPAS is technically sufficiently safe to perform the missions conform the operational manual, as stated in Appendix 3.8 of the regulation.

During the inspection of the RPAS the following topics concerning the build quality and construction of the RPAS will be investigated [5]:

- Used materials
- Assembly
- Impression of the build quality of the airframe
- Determination of mass and centre of gravity

The application of the mechanical system will be judged according to the desired mission of the system.

Compared to the EASA and JARUS regulations, as described in section 2.3.2 and 2.3.3 respectively, this regulation is the most easy to comply with.

2.3.2. EASA regulations

The European Aviation and Safety Agency is responsible for the legislation and its implementation in the field of civil aviation with its primary objective, safety [44]. As the number of drones has risen sharply the last couple of years, the urge to have a European wide legislation increased. As of the creation of the EASA the regulation of RPAS that have an MTOM of less than 150 kilogram need to comply with the regulation issued by their respective Member States [44].

On the 22nd of December 2017 the agreement between the Council and the European Commission and Parliament was reached that the legislatory power of the EU would be extended to "*cover regulation of all civil unmanned aircraft systems (UAS), regardless of their maximum take-off masses(MTOMs)*" [14]. This means that after the rules come into effect, the NAA's regulation will no longer be valid. The proposal has been put forth for adoption by the European Commission and was passed on the 11th of June 2019 [43].

Two categories of drones will be implemented (as described in Section 2.3.1.6 in [13] & in the Annex of [14]):

- Category A ('Open')
  Weight $\leq$ 25 kg, maximum allowed height of 120m, in Visual Line Of Sight (VLOS).

---

[5] ENM/BSK-2015/11533, `https://wetten.overheid.nl/BWBR0036568/2019-04-01`

- Category B ('Specific')
  Weight ≤25 kg for any operation that does not fall within the Open category.

The third category is not covered by the new regulation proposal, which is the certified category (as described in Section 2.3.1.6 in [13]).

- Category C ('Certified'), the following operations are classified as certified-category operations:
  - "large or complex UAS operating continuously over open assemblies of people;"
  - "Large or complex UAS operating BVLOS in high-density airspace;"
  - "UAS used for transport of people; and"
  - "UAS used for the carriage of dangerous goods, which may result in high risk for third parties in case of crash."

This means that certifying a RPAS in the weight category of 25 kg to 150 kg can not be expected to be possible under the upcoming European regulation proposal. Hence the National Aviation Authorities (IL&T in the Netherlands) stipulate the requirements for this category for the moment, as described in section 2.3.1.

The new European regulations have been published on the 11th of June 2019 by the European commission (regulation 2019/945 and 2019/947 in [43]), these regulations will come into effect in June 2020. However these regulations only cover the operations of drones and not the design requirements. The certification specifications are expected to be published in late 2019.

2.3.3. JARUS

The Joint Authorities for Rulemaking on Unmanned Systems (JARUS) is an international body of NAA's and other experts that has the objective to unify the regulations and guidance material such that each NAA or authority can write their own requirements on UAS. The JARUS publishes both operational regulations and certification specifications as well.

CS-LUAS The Certification Specifications for Light Unmanned Aeroplane Systems (CS-LUAS) for fixed-wing UAS up to 750 kg are available [23] as of 2016. These specifications only cover fixed wing aircraft, the CS-LURS [24] counterpart covers rotorcraft. Tiltwing and other convertiplanes are not covered. As the CS-LUAS specifies other specifications may follow to cover aircraft that do not fall in the fixed- or rotary-wing category. The CS-LUAS is written for the certified category (see section 2.3.2) in mind.

CS-UAS The Certification Specification for Unmanned Aircraft Systems (CS-UAS) is a set of design-independent objective requirements which specify the objectives that must be met in order to certify unmanned aircraft systems that fall under these certification specifications [25]. The CS-LURS and CS-LUAS are the Airworthiness Design Standards which comply with the CS-UAS, and hence they can be used to certify the prototype in the 'C' or 'Certified ' category. However the CS-UAS by JARUS is not yet in effect in Europe, but it is expected to come into effect in the upcoming years. The CS-UAS was released in October 2019. The CS-UAS depicts the regulations that can be expected for EASA certified category of UAS and has a larger applicability up to 3175kg and 8618 kg for UAS with and without VTOL capability respectively.

2.3.4. Concluding remarks

The current state of the regulations is a state of transition. In this transition the regulations change from a state regulations to European wide regulations. Three categories will be introduced in the new European regulations; namely the Open, Specific and Certified categories. The new regulations in the Open en Specific categories will come into effect by June 2020, the Certified categories will come into effect a couple years later. For now it is recommended to design the vehicle for the Specific category as this will reduce cost and reduces the time to market. However for Beyond Visual Line Of Sight (BVLOS) operations over populated areas it is likely that the vehicle will be placed in the certified category due to the increased risk assessment in the SORA (Specific Operations Risk Assessment) by JARUS. Hence it is advised to take the loads section of CS-LUAS subpart 'C - Structure' and 'D - Design and Construction' into account during the design of the prototype. Such that the step towards the certified category will be less of a hurdle.

2.4. Research objective

Based on the proposed concept of the CTO challenge, a smaller prototype will be developed to prove that a hydrogen hybrid VTOL vehicle will be possible. In the development of vehicle multiple topics require investigation such as: vehicle sizing, stability & control, the hybrid propulsion system, airframe design. This thesis focusses upon:

The development of a lightweight structure for a prototype of a VTOL tandem tiltwing drone concept with a distributed hybrid electric propulsion system.

The objective is to *design a structure for the drone prototype by analysing the expected loads and manufacturing concepts available and by performing a strength analysis on the designed geometry such that the structure will not fail under these expected loads.* The primary focus of the design in this research will lay on the wing structure including the rotating mechanism.

In fulfilling the objective the following research questions will be answered:

- What is the **most suitable manufacturing method** for the drone prototype with respect to lightweight construction and ease of manufacturing?
- What is the **best structural layout** considering the load requirements, ease of manufacturing and weight?
- What are the **critical load cases** for the vehicle?
- What are the **required skin thicknesses** to prevent failure under the imposed loads?
- What will the **weight** of the proposed drone structure be?

3

Concept overview

This chapter provides informations on the evolution of the tandem tiltwing concept. The chapter consist of three sections which describe the initial design (section 3.1), the improved designs (section 3.2) and a design description 3.3 of the current version.

3.1. Initial design

The initial layout of the concept did not feature much details as can be seen in figure 3.1, only the outer geometry was defined. The concept exists of a fuselage, a canard and a main wing. For clarity; the canard may be referred to in this report as: canard or front wing. The wing, may be referred to as wing, main wing or rear wing. The plural, wings, will be used to refer to both the canard and wing.

The canard and wing rotating mechanisms were initially planned as tubular wing spar which would be mounted on bearings. Both wings would be separable by removing the left and right wing section. No specific landing gear was thought up yet. Due to the low thickness of the canard, which is only four centimetres thick, embedding the inner fuel cell into the canard cannot be performed without complicating the structure of the canard. The spar needs to be located around the fuel which would require a complex bulkhead. This would unnecessarily complicate the manufacturing process. The fuel cell dimensions are roughly 196 mm in length by a width of 88 mm and a height of 60 mm. Hence, to improve the ease of manufacturing of the canard the pods were moved upwards to make room for the wing structure underneath. Moving fuel cells upward also meant, moving the propeller slip stream upwards which increases the lift during cruise slightly. Yaw stability is provided by means of two winglets located on the outer motor pods on the main wing. Except for the rotating mechanisms of the wings no specific control surfaces were planned.

3.2. Improved designs

Further design improvements were made to the design of the concept as detailed in this section. In the design process more variants were created but for brevity only three concepts are shown with the most significant changes.

3.2.1. Concept 2

The improved layout of concept 2 included design considerations with respect to the fuel cells, the landing gear and the wing structure, see figure 3.2,

The most notable change is that the canard and wing are relocated to the bottom and top of the

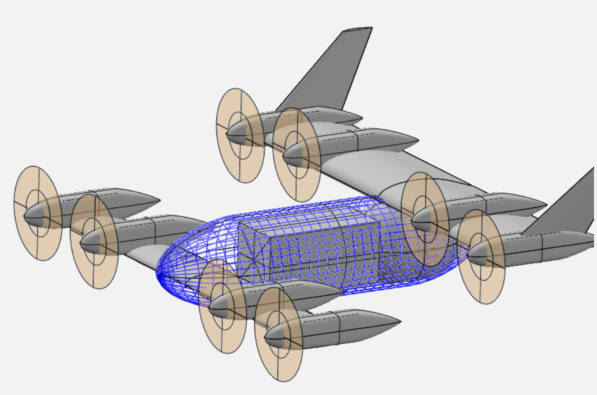

Figure 3.1: Concept 1

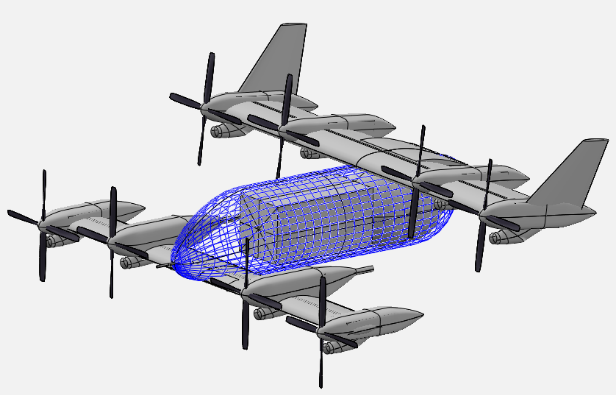

Figure 3.2: Concept 2

fuselage respectively. This was done such that a continuous wingbox could be used, instead of a tubular spar. This is the same as for most tiltwing reference aircraft described in section 2.2. The continuous wing eliminates the requirement to transfer the bending loads from one wing half into the tubular spar and back to the other wing. This reduces both the stress concentrations in the wings and the amount of parts. Two bearings at centre section will be used to transfer the shear forces to the fuselage, and as rotation axis. Another change to the design is the implementation of the landing gear on the inner motor pods of the canard. A tail skid on the rear of the fuselage provides the third point of contact with the ground.

3.2.2. Concept 3

In the third concept more design changes were implemented and more detail was added. First of all a specific commercial available fuel tank was selected which had a smaller diameter but was longer in length. This required an extension of the fuselage rearwards.

As the inner fuel cells on the canard would interfere too much with the structure without having a very large nacelle sitting on top of the wing, it was decided to relocate the fuel cell into the nose of the aircraft. This required an extension of the nose to make enough space for the fuel cells. With a nose extension, the centre of gravity was moved forward. This improved stability as the neutral point was found too near to the centre of gravity of the aircraft.

A benefit of the tiltwing concept is that the neutral point can actually be adjusted by changing the incidence angle on the wing and canard. This allows for a larger centre of gravity envelope than regular canard aircraft have. Ventral fins were added to the rear of the fuselage to improve the directional stability and decrease the roll stability, the ventral fins are also used as landing gear. This decreases the risk of damage to the fuel tank during hard landings.

During the rotation of the wings from horizontal to vertical large forces will act upon on the wings. The shear will be transferred by the attachment points and the twisting moment of the wing has to be taken up by he actuators. Linear actuators were chosen above a worm gear mechanism, as the total force on the actuators would be lower due to the larger moment arm. Actuators with a spindle should be used such that the actuator only needs to drive the mechanism when a movement is required.

The inner main wing motor pods have been moved downwards to leave a clean upper surface. A fairing on top of the fuselage was added to house the main wing actuator. This increased the height of the main wing. This allowed the diameter of the propellers to be increased from 406 mm (16 inch) to a maximum of 432 mm (17 inch). Which improves the thrust that can be generated by the

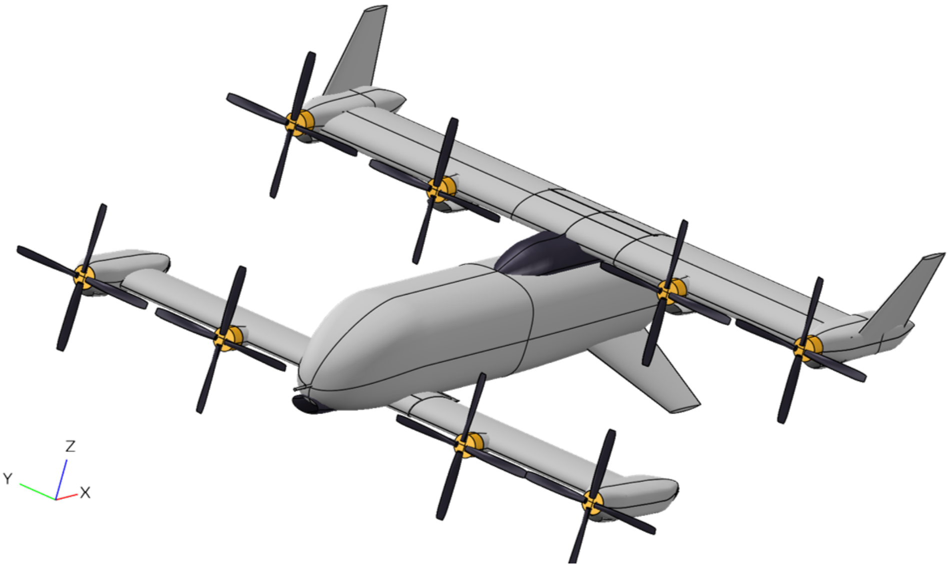

Figure 3.3: Concept 3: Further improvements. Note the removal of the inner canard pods, lowered motor pods on the main wing and the addition of the ventral fins.

propellers required for take-off.

Full span elevons were added to the canard to provide pitch and roll control during cruise, as well as yaw control during hover. A visual representation of the third concept can be seen in figure 3.3 and 3.4.

Figure 3.4: Concept 3: Sitting on the ground in hover configuration.

3.3. Concept description

This section describes the different components of the aircraft in more detail. The three main components are the fuselage, the canard and the wing which are described after the general introduction in the following section.

3.3.1. General

The concept is a tandem tilt wing aircraft powered by a hybrid electric propulsion system. The sizing of the aircraft is a challenging task. The goal is to create a functional platform that is capable of carrying a 10 kilogram payload over a range of at least 100 kilometres while not emitting greenhouse gasses such as CO_2 and CH_4, and being capable of vertical take-off and landing capabilities. The use of a hydrogen fuel cell system increases the energy density of the propulsion system, which results in a larger range. The system comes with some disadvantages though, the first is that the hydrogen system requires a large volume, both the fuel tank and the fuel cells are bulky, which increases the fuselage in size and increases drag. A second disadvantage is that contrary to the energy density, the power density is decreased and hence booster batteries are required to deliver short bursts of high power during take-off for example.

The requirements for VTOL operation require a large propeller diameter to ensure that enough thrust can be generated during hover. The wing size however, can remain rather small since no stall speed requirement is present. This results in an aircraft with a small wing which is efficient for cruise flight.

Table 3.1: General vehicle properties

Parameter	**Symbol**	**Value**	**Unit**
Maximum take-off weight	MTOW	50	[kg]
Empty weight	OEW	40	[kg]
Range	R	180	[km]
Payload weight	W_{pl}	10	[kg]
Cruise speed	V_{cruise}	32	[m/s]
Stall speed	V_s	25	[m/s]
Canard			
Span	b_c	1.50	[m]
Chord	c_c	0.30	[m]
Wing			
Span	b_w	1.50	[m]
Chord	c_w	0.35	[m]

3.3.2. Fuselage

The fuselage is a 1610 mm long rounded rectangle with a width and height of 260 mm and it is made of fibre reinforced composites. Two bulkheads separate the fuselage in three sections. In the front section two fuel cells are located, together with the autopilot, control hardware and the canard actuator. In the centre section the payload bay is located as close to the centre of gravity of the vehicle as possible. The rear section houses the hydrogen tank, which is sized for HES A20 tank by HES Energy Systems . The wing actuator is located in the fairing above the fuel tank. See figure 3.5 for the layout of the components in the fuselage.

On the rear of the fuselage on the bottom two ventral fins are located which are angled 45 degrees downward such that they function as aerodynamic surface and as landing gear.

3.3.3. Canard

The canard is an un-tapered wing with a chord of 300 mm and a span of 1500 mm (1600 mm when the motor pods are included). Four motors are located on the canard. The motor pods located on the canard tips house a fuel cell, a battery, motor and landing gear each. The canard will rotate approximately around its quarter chord point and is rotated by the linear actuator located in the fuselage. On the canard two elevons are located to provide the control which are powered by servos embedded in the canard. The canard will be held in place by two pivot points in the front and the actuator on trailing edge of the canard.

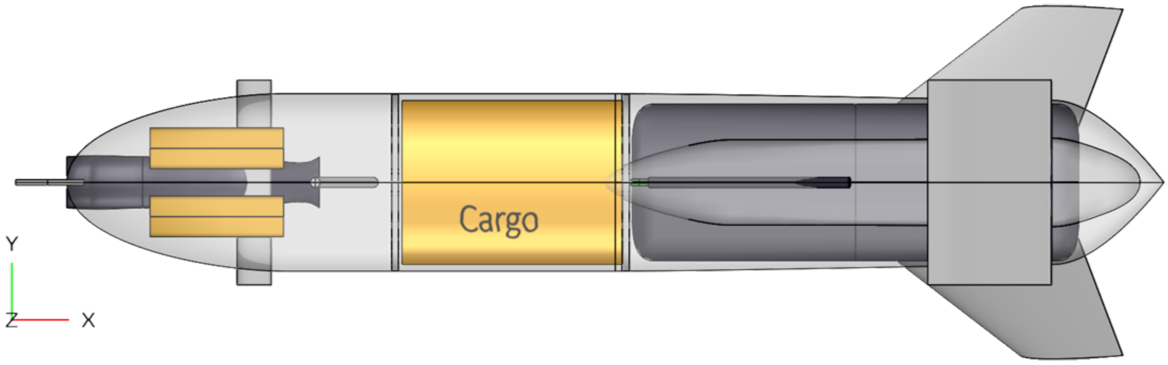

Figure 3.5: Fuselage top view of the concept with internal components.

3.3.4. Wing

The wing is an un-tapered wing with a chord of 350 mm and a wingspan equal to the canard. On the main wing four motor pods are located which all house a fuel cell, a motor and a battery. On the outer motor pods the winglets are mounted to provide directional stability and to decrease the effect of wingtip vortices. The wing is supported by two pivot points behind the rotating wing and the actuator which attaches to the front of the main wing. The front part of the wing is hollow and can be detached since the batteries and motor electronics are housed here.

3.3.5. Sub system description

The landing gear arrangement, propulsions system and actuator system are described in this section.

Landing Gear The complete landing gear system consist of two small wheels located in the outer canard motor pods and the ventral fins located on the aft fuselage. This layout provides low drag without the need for a retraction mechanism. It does however induce large forces on the canard during a landing impact. More on this topic will be dealt with in section 8.2.3.

Hybrid propulsion system The aircraft will be powered by eight electric motors and eight propellers. To increase the efficiency of the aircraft it requires that the energy density of the propulsion system is as large as possible. Battery power alone does not provide enough energy as the energy available is not more than 150-200 Watt hour per kilogram on a system level. Hydrogen has a much higher energy of 33 kWh per kilogram. However to convert the chemical energy to electrical energy a fuel cell is required. This fuel cell increases the weight of the system and lowers the system energy density. The current design is able to yield an energy density of 670 Wh/kg, however the fuel cell is only able to supply the cruise power. Hence a booster battery is required to supply peak power demands. This booster battery reduces the system energy density to 600 Wh/kg. This is still three to four times the energy density than that of a pure battery powered propulsion system.

A drawback of hydrogen is that it has an extremely low density and even under a high pressures it requires a large volume to store the energy. Another point of attention is that the fuel cells require air for the chemical reaction but also for the cooling of the stack itself. The choice was made to use one fuel cell per motor pod instead of a single large fuel cell. This simplifies the cooling systems as plenty of cooling air passes along the wing. Furthermore by placing the fuel cells near the motors the need for long high power electrical cables reduces. The drawback of the rather large fuel cells is that they complicate the canard and wing structure.

Actuators The canard and wing require actuators to change their respective angles. The actuators selected are linear actuators. The reason for selecting linear actuators over gear driven systems is that the force on the wings cannot rotate the motors and hence the wings will be locked in position. A worm gear mechanism also prevents the actuator from being rotated by a force on the wing, however due to the small moment arm, high shear forces on the teeth of the gear are present. As the lead screw type linear actuator will not load the motor when a moment is acting on the wing, the motor of the actuator can remain unpowered when the wing is not moving. This increases the lifespan of the actuator and reduces energy consumption.

4

Construction & manufacturing Techniques

Different construction and manufacturing techniques can be used to create the structure of the aircraft. This chapter describes which construction type and which manufacturing techniques are chosen for the prototype structure. The choice of a construction and manufacturing technique, material choice and geometry is interrelated. The structural geometry will be discussed in chapter 5, the material choice will be described in chapter 6.

4.1. Construction concepts

Three main construction concepts are used in composites: monolithic, stiffened and sandwich laminates. A good comparison between the three concepts can be found in the book of Kassapoglou [26, Ch.13]. In this comparison the three concepts are designed for two loading conditions, one in-plane loading and one out of plane loading.

Monolithic panels are only an adequate design when only an in-plane tensile loading is present or when the allowed thickness of laminate is limited. When buckling criteria or out of plane loads play a factor both the stiffened and the sandwich panel perform much better. This can be easily seen because to increase the buckling load of a panel its bending resistance must increase. By just adding more plies, in case of the monolithic design, very little bending stiffness is added while the weight substantially increased. The simple panel geometry requires little labour to manufacture, see figure 4.3. The costs of a monolithic panel are therefore low.

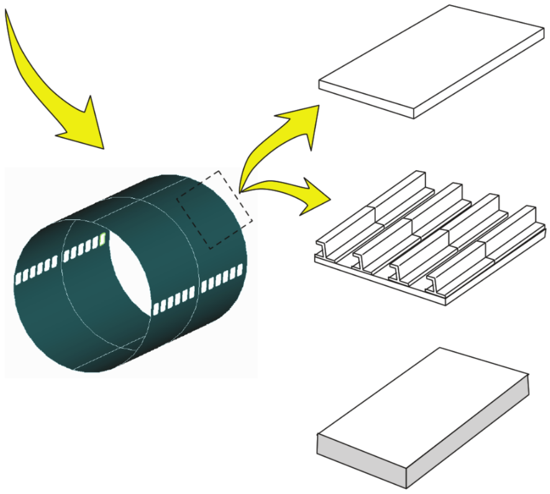

Figure 4.1: Typical composite construction concepts. Figure from the Kassapoglou comparison ([26, Fig 13.1]). From top to bottom; monolithic, stiffened and a sandwich panel construction.

In a **stiffened skin**, stiffeners are added to a monolithic panel, they take up a part of the load and provide a lot of bending stiffness. This reduces the load in the skin. A reduced load in the skin means that the skin can become thinner. Which lowers the total weight of the panel. The addition of stiffeners also allow for post-buckling of the skin without a collapse of the panel. The stiffened panel is lighter than the monolithic panel, see figure 4.2, but it has substantially higher costs compared to the other two panels due to complex geometry, as described in the example of Kassapoglou. A variant of the stiffened skin is a grid stiffened panel in which the stiffeners are connected in a grid pattern.

A **sandwich** panel increases its bending stiffness by separating the facesheets by a low-density core. This simple geometry allows a large increase in bending stiffness while the labour cost are almost equal to the monolithic laminate [26]. This results in a cheap and light panel, see figures 4.2 & 4.3. Common core materials that are used are: foams, woods, and honeycombs. The drawback of sandwich constructions are the additional failure modes such as skin wrinkling, core failure and adhesive failure. Attaching the sandwich panels to other parts of the structure requires care as well as ramp downs and inserts, which also introduce additional failure options.

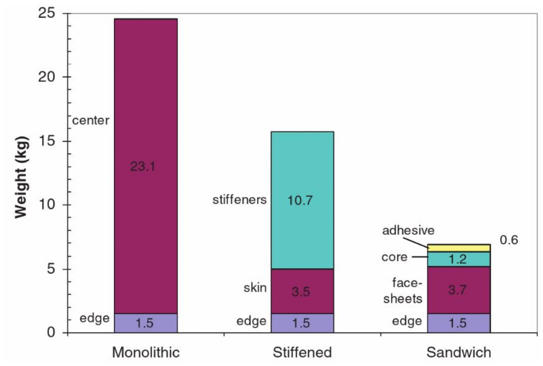

Figure 4.2: Panel weight comparison. From Kassapoglou [26, Fig.13.11]

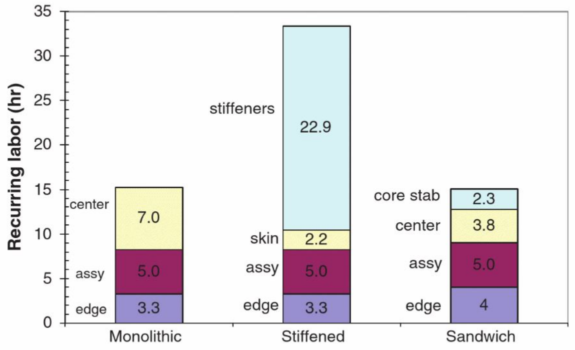

Figure 4.3: Panel cost comparison. From Kassapoglou [26, Fig 13.12].

An alternative to the regular sandwich design is the mouldless composite construction. In this method a wing is created were the entire volume of the wing cross-section is filled with a foam core. The entire wing cross-section can therefore be seen as a sandwich itself. This construction method has interesting benefits during the manufacturing of parts. Contrary to the other methods, this method does not require special moulds. A foam core will be cut to shape and will be used as both a stabilizing core and as tooling. The next section describes the method in more detail.

4.1.1. Mouldless composite construction

The mouldless composite design method was developed by Burt Rutan and was frequently used on the aircraft he designed for homebuilders such as the Long-Ez, VariEze, Defiant and the Quickie. The construction method uses a foam core that can be shaped to any form, usually by means of hot wire cutting, sawing or sanding. Before the laminate is put on the surface of the foam, a coat of epoxy resin combined with glass micro balloons, is used to fill the pores of the foam created by the cutting process. Next the fibre reinforcements are laid up and impregnated with resin. After the stacking is complete the laminate is left to cure. Multiple steps might be required to create the spar, shear web and skins. The entire process of is well documented in the booklet *"Moldless Composite Homebuilt Sandwich Aircraft Construction"* by Rutan [38].

During the process the core material is left in the part. The core is structurally only used to act as an elastic foundation which prevents buckling, as described in the following passage from the *"Structure.pdf"* from the Rutan Aircraft Factory CD-ROM Encyclopedia [39]:

"All primary structure is on the surface, not buried and insulated in the interior, so that there are no internal stresses generated by rapid temperature changes. The composite sandwich is designed such that no loading exists that could stress the foam core or cause its separation from the glass structure. The solid foam core

eliminates all ribs from the flying surfaces. Peel loads are minimized and internal inspection is not required." [39]

The structural benefit of this method is that the skins can remain thin but they have a much higher buckling load due to the stabilization. Other benefits as given in the document are:

- Higher strength to weight ratio
- Quieter than an aluminium airplane
- It provides thermal insulation
- Higher fatigue margin due to lower stress concentrations
- Easier construction of complex shapes
- Easy to build due to fewer parts
- Better resistance to corrosion

The most important reason mentioned by Rutan for using this construction method is the reduced build time. This is mainly beneficial for the designer, who can quickly iterate by incorporating updates in the design without the need of creating moulds first. An important note must be made here that the afore mentioned reason is of course only valid for a single or low volume airplane production. When an aircraft can be produced in series this reason does not hold any more. The benefit also holds for the homebuilder who does not need specific tooling. This saves a lot of money and time in the prototyping phase.

It must be noted however that the manufacturing process requires a lot of intermediate curing steps. In the build manual of the Cozy Mark IV [10], which is a derivative of Rutan's Long-Ez, the canard requires at least ten cure cycles. The shear spar, top spar cap, bottom spar cap, top skin and bottom skin and the joining of the front and aft cores all require the part to cure before continuing. For a series production waiting for so many cure cycles is expensive. However creating moulds would still require a plug to creating the moulds from. This is a very time consuming process. For series production a construction methods based on moulds would be more advantageous.

An example of a wing cross-section made with the mouldless composite construction method can be seen in figure 4.4. In the figure a shear spar is visible which confirms that the foam is not used to carry the main shear loads of the wing. Another reason to use this manufacturing method is that is really easy to produce a very clean wing which is perfectly suitable for retaining laminar flows. Common materials used in the process are XPS foam, PVC foam, fibreglass and carbon fibre.

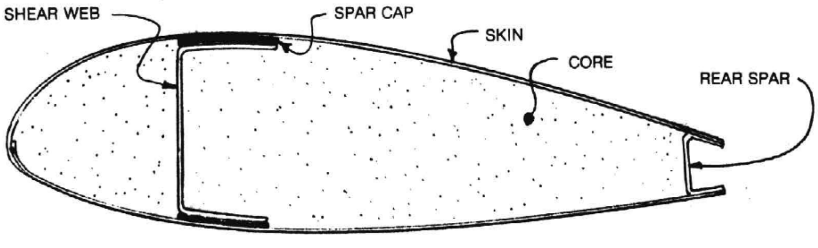

Figure 4.4: Typical wing structure made with the mouldless composite construction techniques from Rutan. No ribs are present. Figure from the Structure chapter from RAF Encyclopedia.[39]

4.2. The composite manufacturing process

This section contains all the steps required in the process of producing a composite part. It starts with pre-processing followed by fibre placement, debulking and consolidation, impregnation, curing, post processing and lastly assembly. Only thermoset production processes are considered as thermoplastic composites require expensive tooling which cannot be justified for single prototypes.

4.2.1. Pre processing

In the pre-processing step the preparations are made for the production of a composite part. The pre-processing is different for a moulded part compared to a mouldless part.

Moulded construction A tool or mould is required to support the fibres during the production process in order for the composite part to maintain its shape during the curing process. In the pre-processing step for moulded parts the moulds are prepared for production. First the mould needs to be cleaned of the residue that might be left from the production of the previous part. After cleaning, the mould needs a treatment with a mould release agent. This agent prevents that the part will adhere to the mould and that it can be easily remove from the mould.

For different manufacturing processes different moulds are required. Sometimes just a single mould will suffice, for example when a simple wing skin is laminated. For more complicated parts it might be necessary to split the moulds in multiple sections to aid in removal of the composite part. Depending on the required shape an OML (outer mouldline) or IML (inner mouldline) mould can be used. In an OML the mould has the shape of the outer geometry op the part. This has as a benefit that the part has an extremely smooth outer surface, something desirable for wing skin panels. However an IML mould determines inner geometry of the part. A benefit of an IML mould is that the tolerances between different parts that need to be joined can be much smaller resulting in a better fit.

Mouldless construction A less known construction method is to make parts and assemblies by means of mouldless composite design, as described in section 4.1.1. For the pre processing stage of the mouldless construction technique consists of shaping the foam. This can be performed manually by hand with the aid of templates and a hot wire cutter or by means of a CNC wire cutter. Hot wire cutting has the limitation that only straight (and tapered) sections can be cut. CNC milling could also be used to create a 3 dimensional core. However, joggles and cut-outs are mainly formed manually into the foam.

After the foam has been shaped, just before the fibres are placed on the core, a layer of epoxy filled with glass microballoons is put on the foam. This assures a good bond between the foam and the fibre reinforcements and prevents that resin is sucked out of the fibres leaving voids.

4.2.2. Fibre placement

The placement of fibres can be performed by hand or by machine. In this case only oriented continuous fibre composites are considered.

Hand layup In the hand layup process the fibres are put in place by hand. A big benefit of the hand layup process is that little up front cost is required with regard to fibre placement. Also the flexibility and the ability to laminate very complex shapes are benefits. A drawback of the hand laminating process is that the accuracy of the fibre orientation is lower than when a robot is used. By using an overhead laser projector the accuracy and speed of the layup can be improved. Furthermore for large series production the cost of labour are high. And hence automated processes show more advantages at larger series. Fibre handling is another point of attention. Especially using unidirectional fibres or non crimp fabrics the possibility of distorting the fibre orientation is a certain possibility. Hence parts made by hand layup can have a lower quality.

Sandwich panels can be created by adding the sandwich cores in the laminate during the stacking.

Automatic fibre placements Different processes are available to place fibres on a mould automatically. Automatic tape laying, automatic fibre placement, filament winding, braiding, resin transfer moulding and pultrusion are commonly used automated fibre placement options. The benefits are high accuracy and repeatability, and lower recurring costs. The upfront costs for these methods are always high and hence they can only be justified for large production quantities. The accuracy and repeatability is high, furthermore the compaction is good, and hence high quality parts can be made.

Debulking During prepreg lay-ups air is inevitably entrapped between the plies. When cured this entrapped air will result in a high void content. Therefore, to improve part quality after a certain amount of layers the laminate is debulked [42, p.395]. In this debulking process the laminate is compacted by a vacuum and hence voids are reduced. This debulking can take quite some time. In [22] a visual example of debulked laminate is given for a debulking period of 4 and 12 hours respectively. In the 12 hour debulked specimen the void content is substantially lower.

4.2.3. Impregnation

Different methods of fibre impregnation are available for non automated laminating processes. This section details wet layups, vacuum infusion and pre impregnated fibres or prepregs for short.

Wet layup In wet layup the fibres are impregnated during the layup process. After each layer of reinforcement the fibres are impregnated with resin. With rollers or squeegees the excess resin is rolled out of the plies in order to compact the laminate. The wetting of the glass fibres is rather easy as un-impregnated fibres show distinct white areas as properly impregnated glass fibres are more translucent. The wetted laminate usually has a slight green tint depending on the matrix material used. A uniform tint indicates a good impregnation. For other fibres such as carbon this visual confirmation of proper wetting does not occur. In this case special care must be given such that the laminate is thoroughly wetted. [9, P.20] After the laminating is complete the curing can start with or without a vacuum applied.

Vacuum infusion In vacuum infusion processing (VIP) the entire laminate is laid down after which a vacuum is applied. Checks for leaks are important as leaks can draw in air into the part and induce severe voids. When the vacuum bag is leak free, the resin is infused into the laminate due to the pressure difference between the vacuum and atmospheric pressure. As the resin must transfer through the laminate a low viscosity resin is required. Special attention must be given to the layout of the aiding materials such as flow mesh, infusion line and the vacuum bag. Improper layout of these components could cause runners, in such a case resin can race to the outlet ports while not all fibres are impregnated. This can cause dry spots leaving the part unusable. [9, Ch.16]

Sandwich panels with foam cores can be infused as well, sometimes grooves are created in the core to improve flow speeds. Honeycomb cores cannot be infused as the cells will fill themselves with resin, and dimpling might occur.

Pre-impregnated fibres The use of pre-impregnated fibres or prepregs come with the advantage that the right amount of resin is already present in each ply. Hence a higher fibre volume fraction can be achieved. However attention should be given to the debulking process to prevent air entrapment. The prepreg process can result in a better part quality however autoclave or oven curing is required. [9, P.17].

4.2.4. Curing

During the curing process the resin (usually epoxies) cross-links are created between the epoxy and the hardeners. A single large cross-linked molecule (thermoset) is formed during this process. In the curing process heat is generated, this could pose problems when the epoxy is kept for too long in large volumes [42]. The exothermic reaction could cause a fire when the heat build too much.

Autoclave curing After the final debulking step the curing process is started. In the curing process volatiles in the resin want to turn into their gaseous state when the pressure is lower than the vapour pressure. When these volatiles come free they form voids and reduce the properties of the laminate such as the shear strength, a reduction of 7% per 1% of voids is reported. Where void contents up to 4% are reported according to [42, p.399]. Therefore pressure needs to be applied to the resin to suppress the formation of voids and yield a high quality part. Pressure can be applied by means of a vacuum but most of the time higher pressures are required demanding an autoclave or press. Since the autoclave process is an expensive process other methods are sought such that out of autoclave curing can be performed.

Out-of-autoclave curing In out-of-autoclave curing the part is cured in an oven only, this can be performed under a vacuum. Therefore the largest pressure that can be achieved is atmospheric pressure or one bar. To prevent porosities low viscosity resins must be used.

A review of out-of-autoclave processes by Harshe [20] shows that progress is made in this field but still steps must be taken in order for autoclaves to become redundant.

A relative new concept is the 'Quickstep' process in which a part is cured out-of-autoclave. This process entails that the part is surrounded by flexible bladders which are filled with a heat transfer fluid. This heat transfer fluid allows higher heat transfer rates than possible in an autoclave. A heat transfer rate of around 15 $\mathrm{K\ min^{-1}}$ for the quickstep process is claimed versus 2-3 $\mathrm{K\ min^{-1}}$ for regular autoclave curing [30]. The benefit of the higher heat rate is that a lower viscosity of the matrix material can be obtained as the heating reduces the viscosity while the curing, which increases the viscosity, has not taken place yet as would have been during an autoclave process. The lower viscosity yields parts that have similar porosities as parts cured in an autoclave while reducing the cycle time. High cooling rates are also possible which can prevent a thermal runaway [40], hence thicker parts could be created. A more detailed explanation of the process can be found in [30] and [2].

Out-of-oven curing When a lower quality of the part can be acceptable the curing of a composite part without additional heat can be performed. This reduction in quality has the advantage of lower costs. But as common with epoxy resins the cure time can be fairly long until the final strength of the part is achieved.

A study published in 2009 [1] investigated the out-of-oven curing of 10 epoxy systems and 2 vinyl ester resin systems. The rate of cure was determined after a day of cure and after almost a year (360 days). The rate of cure at 1 day varied from 70 to 85% and after one year 90 to 98% curing was reached. The X-40 resin system by Applied Polymeric reached the second highest rate of cure after one day and highest rate of cure after one year.

A study on the post curing on sandwich panels made out of extruded polystyrene and aramid honeycomb, T300 carbon fibres and Poly Epoxy was published in 2013 [29]. The study showed a significant increase in the bending and compressive strength of the sandwich panels while the stiffness (deflection), crash energy absorption and core shear strength showed no significant difference.

From both studies an increase in properties can be expected by performing a post cure cycle or by room temperature curing for a longer period of time. Nevertheless the specific effect of the increase of the rate of cure over time or the effect of post curing is dependent on the specific matrix material chosen.

4.2.5. Post processing

After the curing is completed a couple of post processing steps are required. The part has to be de-bagged and removed from the mould. Sometimes the part that comes out of the mould still has rough edges and requires trimming to clean up the edges or milling of pockets and holes where fasteners might be required.

If further steps are required such as in the mouldless composite construction technique the surface need to be prepared for a new bonding stage. Proper sanding is required, alternatively a layer of peel-ply can laid over the last layer. When the part is cured and the peel ply is removal the surface is directly ready for secondary bonding.

Most parts will by painted to provide protection from UV-radiation, to prevent water ingestion, to prevent (galvanic) corrosion and are used to make parts more aesthetically pleasing. Before paint can be applied the surface needs to be prepared. The steps required are surface cleaning, surface roughening, applying primers and applying the paint or coating required.

4.2.6. Assembly

In an assembly multiple parts are joined. Assembling the different parts can be performed by two main methods: using fasteners or using adhesive bonding. A combination of both methods can be also be used in situations where a single solution would not yield the right properties. For example when a stringer could have the tendency to peel off, in such a case a mechanical fastener can be the solution. But as Campbell [9] states in the subtitle of chapter 12: "The best assembly is no assembly required". And that is one of the benefits of composite design, it is easier than in metal design to produce more complex shaped parts which would otherwise require a sub assembly of parts when build with metals.

Fastening The most used joining method is aircraft design in fastening. Fasteners constrain the structure from movement by transferring the load between parts. Fasteners joints can be designed to handle shear, tensile and/or compressive loads. The types of fasteners used in aircraft are rivets, blind fasteners and threaded fasteners. The latter category is used for joints that must not be permanent.

The holes created for fastening cause stress concentrations in the material. Especially for composites the stress concentrations can become very large for unidirectional laminates. Another issue with fastening, and mainly in carbon composites, is galvanic corrosion. Due to the dissimilarity in materials a galvanic couple can be created which promotes corrosion. A notorious combination which causes severe corrosion problems is the combination of carbon and aluminium. Hence frequent use is made of titanium fasteners.

Joining sandwich panels by means of fastening requires the tapering of the panel to a monolithic structure or creating a reinforcement around the fastener. The reinforcement is required since the core is unable to take up the load and could get damaged. This can be performed by inserts or by filling the area around the fastener by potting compound.

Further considerations concerning fastening are hole deformation, failure modes of fasteners, preloading, sealing and corrosion protection.

Adhesive bonding Adhesive bonds are mainly used in shear as out of plane loading lead to peel loads which tear open the bond. Since adhesives have lower strengths than metals a large bond area is required. Due to the absence of holes the stress concentrations due to the bonding is substantially lower. Therefore the fatigue properties are a lot better than fastened joints. One important fact to remember is the shear stress in an adhesive bond is not constant along the cross-section. In a lap-shear bond the edges of the bonded area experience a higher maximum shear stress than the portion in the middle. This 'bathtub' curve is due to the finite stiffness of the adherend. Tapered adherends can reduce the bathtub curve to a nearly constant shear stress. Peel stresses in the lap shear specimens are due to the eccentricity between the adherends cause secondary bending in the joint.

A benefit of using adhesive bonding is the large reduction in parts compared to the amount of rivets that would be required. Corrosion is a lesser problem although attention should be paid to water ingress into the adhesive bond lowering the performance. A disadvantages of adhesive bonding is that the bond cannot be removed easily. Another important aspect is the time required for curing. This is an important aspect for the mouldless composite design as many cure cycles are required to produce a complete structure. Furthermore adhesive bonding requires proper preparation and processes to assure the quality of bonds.

The knowledge presented in this section is based on the 'Adhesive Bonding' lectures series: [34].

Other joining methods Another methods for joining is mechanical interlocking. This is used a lot in the interior of cars where a elastic deformation of a clip holds most parts of the dashboard in place. The benefit of this method that the parts can be joined very fast by simply clicking it in place. Although this option cannot be used for structural applications it is an option for inspection hatches which can be easily opened.

Welding is a joining type that can be used to join metals but also thermoplastics can be welded. Welding thermoplastic is used a lot on parts made by Fokker Aerostructures Hoogeveen. Welding thermoplastics is a fast process but it requires more complicated equipment. Hence it is deemed unsuitable for the prototype.

4.3. Construction and manufacturing process trade-off

In this section the most suitable construction and manufacturing methods are selected. The construction types mentioned in section 4.1 are the monolithic, the stiffened, the sandwich and the mouldless construction technique. The material of choice, which is detailed in chapter 6, is a thermoset composite made out of fibreglass impregnated with epoxy.

The main factors that are important in the choice of the construction and manufacturing trade-off are:

- Low product volume
- Small physical size of components
- Have design flexibility by being able to quickly implement design changes
- Economical

The requirement of low volume, low cost and quick design iterations, rule out automated design processes due to their high setup costs. Hence a hand layup process is therefore the only viable option. The amount of tooling should be kept as low as possible with as few moulds as possible. As described in Kassapoglou [26, Ch. 13], the sandwich construction provides the lowest weight for the lowest cost for a composite panel. Hence a regular sandwich construction will be preferred. The mouldless composite construction is especially interesting in small structures, as the volume required for the foam is not as large compared to larger vehicles. As volume scales with the power of three compared to length, the mouldless composite construction becomes less interesting for large aircraft.

The canard, wing and ventral fins all are small in chord length and therefore the added weight due to a fully filled foam core wing would be rather small. Hence, in combination with the easy and quick manufacturing process, the mouldless composite construction technique is selected for the canard, wing and ventral fins.

The fuselage, the motor pods and some fairings feature double curved surfaces and cannot be filled with foam. Hence a moulded skin, supported by bulkheads, would be required. For the motor pods and fairings the curvatures will provide enough stiffness and they can therefore be made as a monolithic shell. The fuselage barrel and bulkheads requires more bending stiffness in order to prevent buckling and hence either stiffeners or a core material would be required. As described in Kassapoglou [26, Ch. 13], the sandwich construction provides the lowest weight for the lowest cost, hence a regular sandwich construction will be chosen for the fuselage. By using a thin or preformed foam core the shells can be manufactured in a single process by applying a vacuum pressure. Preforming the foam could be performed by thermoforming.

5

Structural Design

The choice of the structural layout, the materials and the manufacturing techniques are all interrelated. The choice of the mould-less construction manufacturing method, described in chapter 4, combined with the materials choices presented in chapter 6, combines into a structure optimized for these methods. This chapter introduces the reader to the structural layout of the airframe. In the first section the global structure is introduced after which the consecutive sections deal with the structure of the canard, the wing and the fuselage respectively.

5.1. Overview

The aircraft consist of tree main sub-assemblies, being the fuselage, the canard and the wing. As described in section 3.2.1, the configuration was changed from separate wing sections connected via a tubular spar to a single wing with a continuous spar. This simplifies both the structure and rotation mechanism of the wings, and makes the wings easier to remove. The canard and wing are both connected to the fuselage by three bolts. Two bolts act as the rotation axis and transfer all the shear loads from the wing to the fuselage. The third bolt connects to the linear actuator. See figure 5.1 for a sketch. The axis of rotation of the wing coincides with the aerodynamic centre such that the aerodynamic moment created will be transferred by the third bolt. Figure 5.3 shows a see-through model of the vehicle geometry.

The design of the vehicle integrates the distributed propulsion system in the wing and canard where possible. This frees up space in the fuselage which is required for the large fuel tank which. The distributed propulsion system has a large effect on loads and on the structure of the wings. To reduce the drag the fuel cells are embedded into the wing.

5.2. Canard

The canard will be a full core composite wing with only a rear spar. This greatly reduces the amount of steps required in the manufacturing process compared to when a main spar would be used. Without a main spar the skins are load carrying members. The shear will be carried by the leading edge, the shear spar, and a tiny amount by the core. A short shear spar on the loading edge is required for transferring the shear loads from the main attachments to the leading edge. For the main wing attachments self aligning bearing will be used to prevent the transfer of any moments to the fuselage.

The motor pods house the motors, the fuel cells and the motor control. As the fuel cells are large components, the integration of the fuel cells is difficult. There are four different fuel cell pods; the

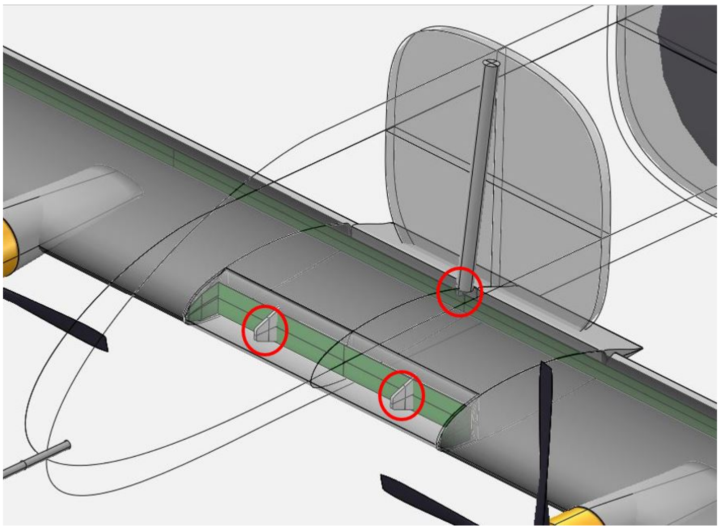

Figure 5.1: Attachment locations of the canard.

canard wing tip pods, the left and right wing pod, and the wing inner pods. The inner motor pods on the canard do not house a fuel cell as the effect on the structure was estimated to be too large. Hence these units were placed in the nose of the vehicle.

5.2.1. Canard manufacturing

The canard will be build in four steps. First the foam core with the right airfoil shape is cut by hot wire cutting, after which the skins are laid up. The next step is to cut out the ailerons and the cut-outs for the attachment. On the exposed foam core the fibreglass will be placed to build up the shear spars. The following steps are to drill holes through the core for cabling and to bolt the tip pods to the end ribs of the canard. In these ribs popnuts or nut plates will be placed. The inner motor pods will bonded to the wing after after a hole for the cabling is drilled to the hole running from the tip to the root. The attachment brackets will be bonded into place after which reinforcement plies will be placed onto the shear spar and the bracket. To aid in the transfer of tensile loads on the brackets, straps will be joined on the top wing skin wrapped over the brackets, and joined to the bottom skin. The servo controls for the elevons will be added after which the wing is ready for painting and all the components can be assembled.

5.3. Main wing

The main wing is the slightly larger version of the canard and also features the same full core composite design, however the layout of the components is quite different. Where the canard had a leading edge cut-out for the wing attachment brackets, the main wing has a trailing edge cut-out for the attachment brackets.

Four fuel cells are located in the wings. Two in the tip motor pods and two in the inner motor pods. The biggest structural issue is with the inner pods of the wing. These pods are embedded in the wing and protrude through the bottom skin where a fairing is used to guide the airflow. The area above and below the wing cannot be used for a structure due to the in and outflow of cooling air through the fuel cells. Therefore a load carrying support structure is required to carry the shear and bending moment around the fuel cells. Fortunately the stresses on the main wing are lower due to the lower loads and larger structural thickness.

The main wing will be build differently form the canard. The full foam core structure is the same but the embedded shear spar complicates the process a bit. In stead of removing the cut-outs after the

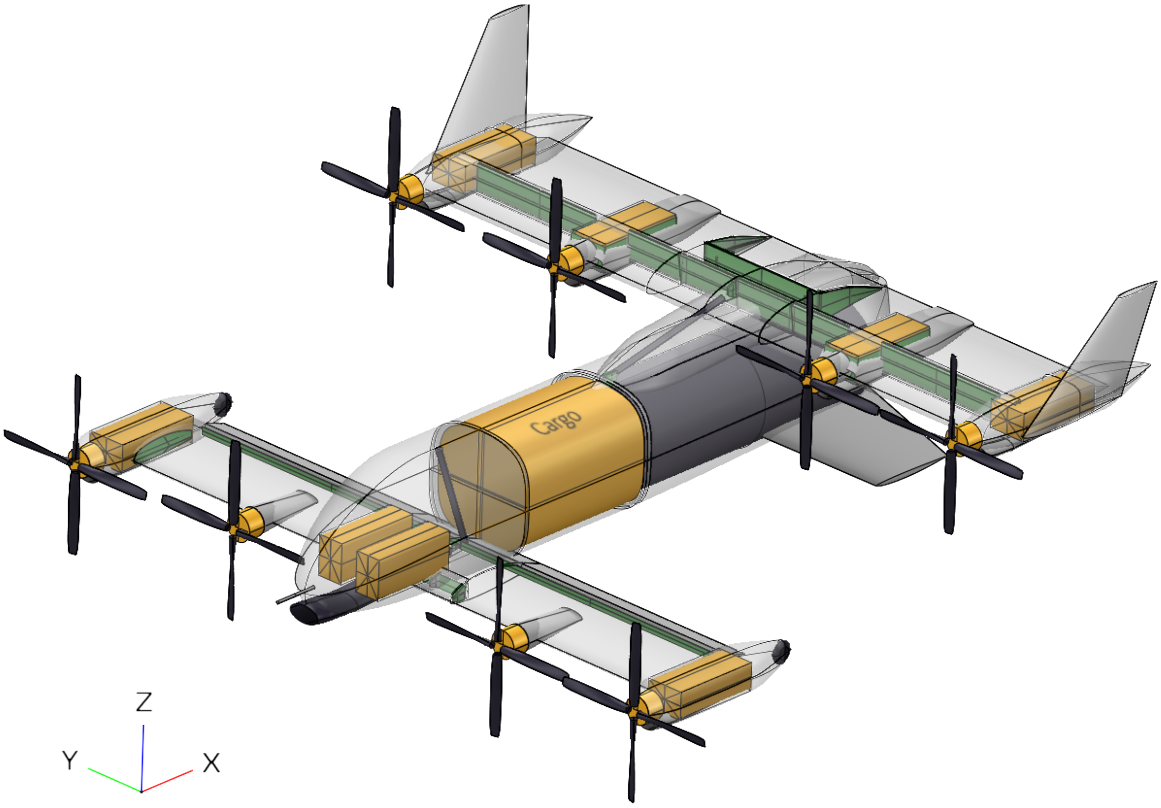

Figure 5.2: Overview of the conceptual drone structure

skins have been laminated, the cut-outs need to be removed before the laminating process. First the shear spars will be laminated. After a curing cycle the laminate will be trimmed and the trailing edge foam core will be glued in place. Now the skins can be laminated. After the skin is completed the cut-outs for the embedded motor pods will be cut and the local reinforcements and wing end ribs will be laminated. After a final trimming procedure, the wing is ready for bolting on the tip motor pods and winglets.

5.4. Fuselage

The fuselage construction will be different from the wings. As all volume in the fuselage will be required for systems such as the fuel tank, the payload area, fuel cells and control electronics, no full foam core can be used. Instead a sandwich skin will used which will be reinforced with bulkheads. The skin halves need to be laminated in moulds, and can be reinforced by thin foam core. For this process a mould is required which needs to be constructed from a master plug. This master plug can be made with the mouldless composite construction techniques or by milling out the shape. For the final design it should be taken into account that also some hatches are required to access the various components inside. The tail cone needs to be removable in order to access the fuel tank, also the payload bay, and control bay require access hatches.

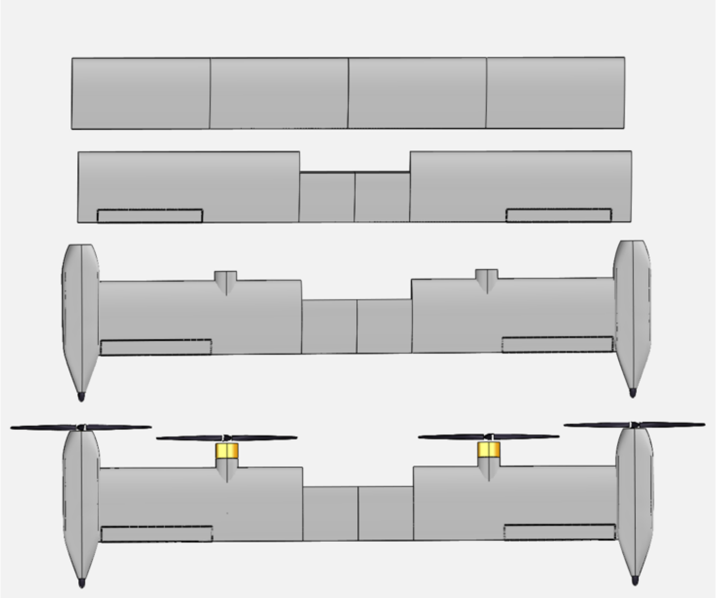

Figure 5.3: Four steps in constructing the canard.

Figure 5.4: Overview of the wing structure

6

Materials

This chapter describes the materials that will be used for the structure and the choices that were made in the selection process. Section 6.1 describes the choices of the material that will be used, followed by section 6.2 which describes the testing of the material samples in order to obtain representative material data that can be used during the structural analysis.

6.1. Material choice

In contrary to metallic structures a composite material is created when the structure itself is created. The material strength and stiffness are dependent on the reinforcement material, the matrix material, the layup used, but they also depend on the manufacturing methods used. In chapter 4 the different construction methods were presented.

The mouldless composite design method was chosen as a construction technique for the canard and wing structure. The mouldless manufacturing method uses a thermoplastic foam core which can be cut by means of a hot wire. After cutting the core, it can be covered with the face sheets with the aid of a thermoset epoxy. The face sheets provide the strength and stiffness, while the core provide the stability of the face sheets and is used to support the face sheet during the manufacturing. Suitable core and face sheet materials must be chosen such that they can be used in the manufacturing process.

6.1.1. Core material

The core material serves several different purposes. Firstly it serves as the shape to laminate upon, this requires the core to be rigid enough during the layup. Secondly it provides an elastic support which can delay buckling of the skin. The benefits of the mouldless composite construction were presented in section 4.1.1. To prevent ingress of resin and hence an unwanted increase in weight, the core material should have a closed cell structure and have a low density. Furthermore it should be able to cut the core by means of hot wire cutting in order to easily create the wing foam cores.

Common core materials can be subdivided into three groups; honeycombs, light woods and foams. Honeycombs are frequently used as core material in composites due to their low density combined with good mechanical properties. However common honeycomb cores such as Nomex or aluminium cores cannot be cut by a hot wire and can take-up a lot of resin if improper methods are used. Woods such as balsa and cork are higher density cores of which the balsa core has very good compressive properties. However the wood cores are rather heavy and cannot be formed easily. The group of structural foams has a large domain and a wide variety of polymers (and sometimes even metals) are used as a base material. Common structural foams are PVC, PMI, SAN, PUR. Polystyrene in expanded form (EPS) and in extruded form (XPS) are also used as sandwich cores but they are not seen often in the aerospace industry. Reasons why EPS and XPS would not be used in the aerospace industry, even though it is one of the lowest density foams, can be attributed to the inferior mechanical properties and poor chemical stability. In the homebuilt aircraft scene mainly XPS, PVC and PUR foams are used. XPS is used since the foam can be easily cut by a hot wire, thereby the builder can quickly make a core for a wing for example. The foam serves as a core material and as a support during the curing of the material such that no mould is required. EPS is not used due to the voids between the expanded beads.

In figure 6.1 and 6.2, the shear modulus versus density and the shear strength versus density of common core materials are given respectively. The goal is to reach the upper-left corner, the highest shear modulus/strength with the lowest density. As can be seen the honeycomb materials perform a lot better then the foams and woods. ROHACELL 31A outperforms almost all foams on shear strength and stiffness.

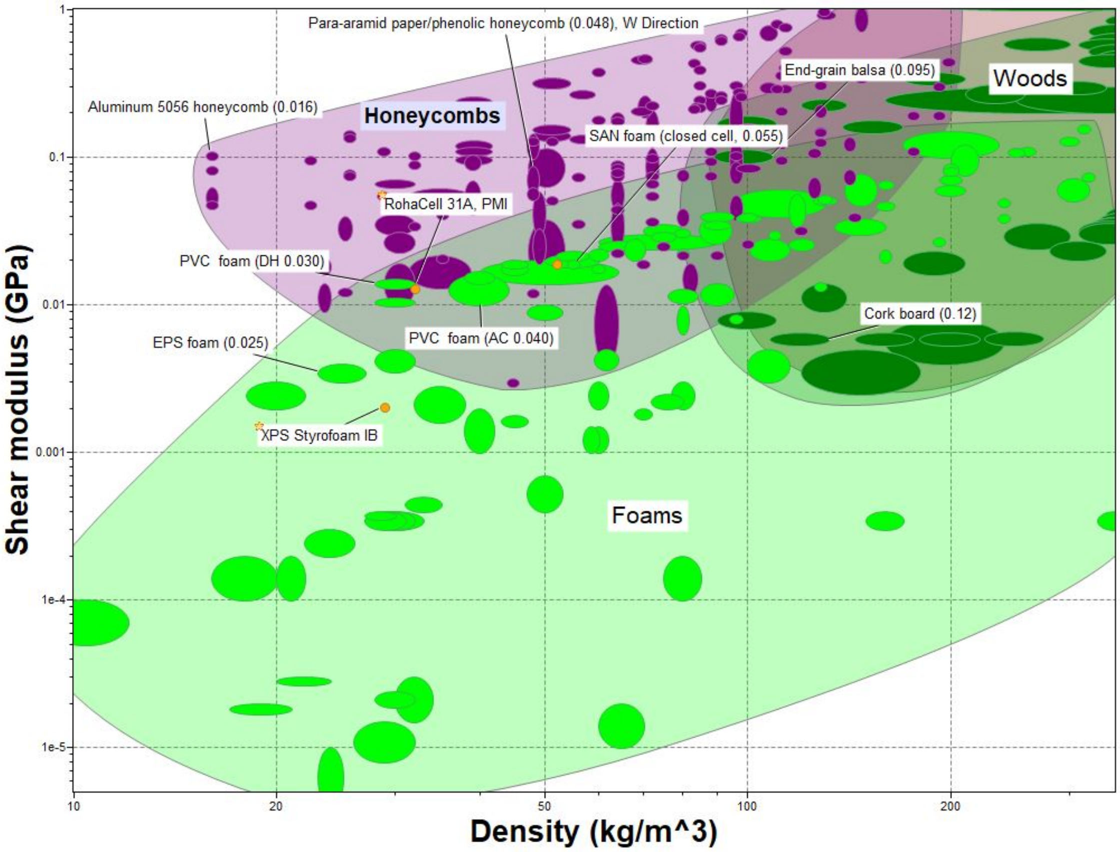

Figure 6.1: Shear modulus versus density of common core materials, created with CES Edupack 2019 data. The numbers behind the names are the density of the respective material in tonne per metre.

A promising relatively new type of foam is PET foam which was introduced around 10 years ago. It is a thermoplastic foam which is a thermoformable foam and it can be produced from recycled PET drink bottles [4]. PET foams are usable with all common resin types. The density of the foam ranges from 60 kg/^{3} and upwards. This is roughly twice the density from common XPS foams. PET foams should also be hot wire cuttable. Although when both Armacell and Gurit were contacted, they estimated that it will be harder to cut properly than XPS. For building full foam core wings the lightest density foam is the most beneficial if enough resistance against buckling can be provided. With an increase in density of a foam the strength and stiffness properties improve. Most other

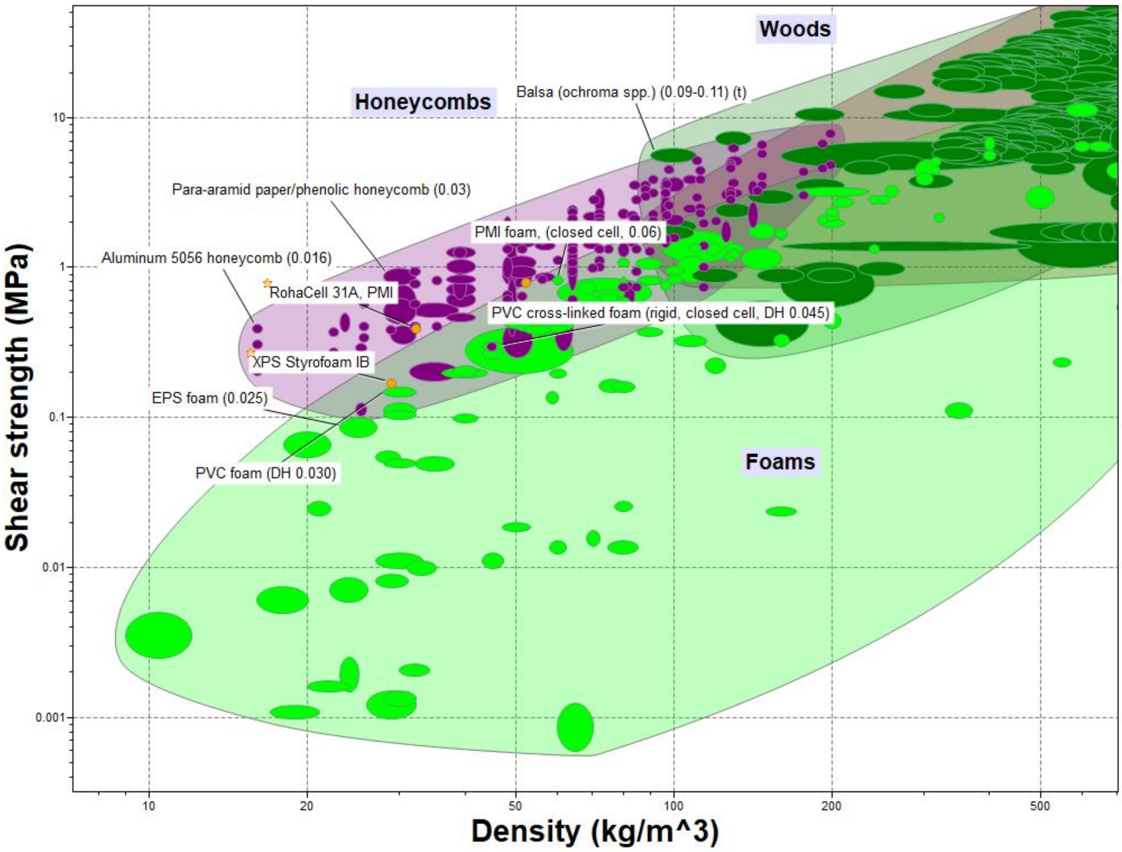

Figure 6.2: Shear strength versus density of common core materials, created with CES Edupack 2019 data. The numbers behind the names are the density of the respective material in tonne per metre.

structural foams such as thermosets cannot be cut with a hot wire since they burn instead of melt. Doing so will release toxic fumes.

Table 6.1: Foam core properties

Material Name	XPS StyroFoam Panel Core 20	PVC Gurit PVC40	PET DivinyCell P90	PMI Rohacell® 31A	Unit
Density	29	40	65	32	[kg/m^3]
Tensile strength	0.344	0.71	1.2	1.0	[MPa]
Tensile modulus	10.3	68	-	36	[MPa]
Compressive strength	0.14	0.52	0.6	0.4	[MPa]
Compressive modulus	10.3	34	47	-	[MPa]
Shear strength	0.172	0.47	0.45	0.4	[MPa]
Shear modulus	2.06	15	13	13	[MPa]
Hot wire cuttable	++	- - [1]	+	+ [2]	[++/+/-/- -]
Thermoformable	yes	yes	yes	yes	[yes/no]
Source	Dow [11]	Gurit [18]	Diab [16]	Evonik[15]	[-]

In table 6.1 the properties of some XPS, PVC, PET and PMI foams are given. Of all foams the prop-

---

[1] Emits Chlorine gass

[2] One source on Youtube shows hot wire cutting of ROHACELL 71 to be possible, but no further information could be found.

erties of the lowest density of each foam type is given. It can be seen that XPS, the lowest density foam, has the lowest stiffness and strength properties. Only a little bit heavier is the PMI or ROHACELL ®31A foam. It has excellent and mechanical properties, and some variants are even self-extinguishing. Hence PMI or ROHACELL is frequently used in aerospace structures. A drawback of PMI is the price as it is more expensive than XPS.

Concerning the usability with a moldless composite design XPS is the first choice, due to low cost and proven compatibility. Structurally PMI and PVC are better contenders than XPS, hence for flat bulkheads or locations where thermoforming could be applied PMI and PVC cores are better. Honeycomb cores can increase the performance even more, as can be seen in figure 6.1 and 6.2, however due to the open cell structure a multi step process would be required to create a honeycomb sandwich compared to a foam core sandwich.

6.1.2. Skin material

The skins are the load carrying members of the structure, therefore strong and stiff materials must be selected. The choice of the material is dependent on performance (i.e. strength, stiffness and density of the material), the cost, ease of manufacturing, and other properties. Composite laminates consists of load carrying fibres and a supporting matrix material. Common fibre reinforcements are carbon, aramid or glass fibres. Common matrix materials are epoxies and polyesters. Thermoplastic matrix materials are being used more and more in the high performance aerospace industry, which have the benefit that welding parts together becomes an option in joining. Thermoplastics are not deemed practical for quick prototyping, due to the requirement of rigid moulds, and are therefore not considered. The choice between epoxies and polyesters is mainly performance based, polyesters lack the strength and stiffness compared to epoxies and shrink during curing, therefore epoxies are the matrix material of choice.

Table 6.2: Material data for carbon, glass and aramid fibres. Data from CES Edupack 2018 Aerospace database, range of typical values.

Property	Glass E grade	Glass S-grade	Carbon Ultra high modulus	Carbon High strength	Aramid 49	Units
Density	2.55 -2.60	2.49 - 2.5	2.05 - 2.16	1.8-1.84	1.44-1.45	[kg/dm^3]
Tensile strength	1950 - 2050	4700 - 4800	2300 - 2400	4500 - 4800	2500-3000	[MPa]
Compressive strength	4000-5000	4000 - 5000	2200-5200	4900 - 5000	200 - 300	[MPa]
Young's modulus	72 - 82	86 - 93	690-830	225-245	117-130	[GPa]
Shear modulus	30 - 36	35 - 39	310-370	100 - 110	1-1.3	[GPa]
Poisson's ratio	0.21 - 0.23	0.21-0.23	0.01-0.2	0.01 - 0.2	0.35-0.36	[-]
Price	1.38 - 2.76	16.5 - 27.6	113-125	21.2 - 28.4	59.4-168	[€/kg]
CO_2 footprint	2.85-3.14	2.85-3.14	19.3-21.3	19.3-21.3	16.4-18.2	[kg/kg]

The choice for the fibre reinforcement is a bit more complicated. Strength, stiffness, price and manufacturability all play a roll. In table 6.2 five fibre types are compared: E-glass, S-glass, carbon UHM, carbon HS and aramid fibres. By far the cheapest option is E-glass, this comes with the poorest mechanical properties. It has a relative high density with low stiffness and low tensile strength. S-glass performs much better but the price is almost as high as the high strength carbon fibres. The ultra high modulus carbon has as its name implies a very large Young's modulus, but with a lower tensile strength. The price of this fibre is very high. Aramid 49 is also an expensive fibre, it has reasonable strength and stiffness except for its compressive and shear properties, these are very low. Aramid fibres are therefore not used in composite load carrying structures. Due to its superior toughness aramid is used on structures that deal with impact such as safety cockpits or bullet proof vests. Aramid fibres are tough to cut and hence manufacturing with Aramid fibres is a little more difficult.

Price comparison The difference in the price between glass and carbon fibres are not always as clear. In Fundamentals of Composites Manufacturing by Strong [42, P.242], an indication is given for the price of common fibres:

- Glass fibre $2.2/kg
- Carbon fibre $ 17.6/kg (General)
- Carbon $ 33.0 /kg (Aerospace)

These prices are in the same range as given in table 6.2. This is a price ratio of 8 for glass versus general carbon fibres (and 15 when compared to aerospace grade fibres). A more practical indication of the fibres price can be made by looking at comparable weaves at the store. Prices of plies, available at R&G Faserverbundwerkstoffe GmbH, with roughly equal thickness were compared see table 6.3. The glass weave is made of Interglas 92145 fibres, and the carbon weave is made of Tenax HTA 40 fibres. It can be seen that carbon fibres are roughly four to five times as expensive as glass fibres.

Table 6.3: Comparison between glass and carbon weave pricing for 100^2 at R&G Faserverbundwerkstoffe GmbH (pricing: September 2019) for roughly equal ply thickness. Prices including VAT.

Property Material	E-Glass weave Interglas 92125	Carbon weave Tenax HTA 40	Units
Weave	Twill	Twill	[-]
Areal weight	280	200	[g/m^2]
Thickness V_f=0.35	0.308	0.327	[mm]
Price per area	5.81	22.20	[€/m^2]
Price ratio w.r.t. area	1	3.82	[-]
Price per weight	20.75	111.00	[€/kg]
Price ratio w.r.t. weight	1	5.3	[-]
R&G Article nr:	190138	190229	

Selection Due to its inferior compression strength and its high price, aramid fibres will not be used. Hence the choice is between glass fibres and carbon fibres. S-glass is clearly superior to E-glass, but its rather expensive. It is almost as expensive as the standard carbon fibres but it lacks the stiffness of carbon fibres. Therefore S-glass will also not be selected. Ultra high modulus carbon is a lot stiffer than normal HS carbon but it lacks the strength, it is just slightly stronger than E-glass. UHM carbon is only interesting when use can be made of the superior stiffness, as that is not the case UHM carbon is also discarded. This leaves E-glass versus HS carbon fibres.

As seen in the comparison between Interglas 92125 and the Tenax HTA40 weave. Carbon is at least four to five times as expensive, but it is also three times as stiff and twice as strong in tension and has a 29 percent lower density. This results in a lighter structure made from carbon, especially since the buckling is less of an issue due to the support of the foam. A property of glass fibres that gives it an advantage during manufacturing is that the fibres are translucent. During the laminating process it can be easily verified if there are any areas with air entrapment, this simplifies manufacturing.

In combination with the lower price, and its proven use on the Rutan aircraft, the E-glass fibre reinforcements is the material of choice during the prototyping phase. Weight is less of an issue during this phase as a slight penalty in weight can be paid by a decreased payload. But pays back in decreased cost and slightly easier manufacturing. For a second iteration or production version it should be investigated if the lower vehicle weight is worth the more expensive carbon fibre.

6.2. Material characterisation

In order to perform a structural analysis the material allowables need to be known. This section describes the material characterisation tests that have been performed on the coupons to determine the material properties of three different E-glass weaves. The material properties that need to be known for the classical lamination theory, see section 9.3.2, are:

- X_t, tensile strength in fibre direction (0 degrees)
- X_c, compressive strength in fibre direction (0 degrees)
- Y_t, tensile strength in transverse direction (90 degrees)
- Y_c, compressive strength in transverse direction (90 degrees)
- S, shear strength

Furthermore the stiffnesses E_x, E_y and G_{xy} and Poisson's ratios need to be known. With these properties the lamina can be modelled by making use of the classical lamination theory, see chapter 9.

Three different testing methods were used to determine the in-plane properties of the composites. The tests were:

- ASTM D3039M [6] Tensile testing
- ASTM D6641M [5] Compression testing
- ASTM D3518M [7] In-plane shear testing

Three glass fibre weaves were chosen as candidates:

- BID - Interglass 92110 - 163 g/m^2
- BID - Interglass 92125 - 280 g/m^2
- UND - Interglass 92145 - 220 g/m^2

The selected E-glass weaves are all made per aviation standards. The selected weaves consists of two bi-directional weaves and one uni-directional weave. The uni-directional weave has the majority of the fibres in the zero degrees direction and the small amount of fibres in the 90 degree direction to improve handling of the fibres. The fibres were impregnated with an epoxy resin system made with the Hexion EPIKOTE LR285 epoxy combined with the EPIKURE LR285 hardener. The resin and hardener were mixed in the weight-ratio 100 to 40 respectively. Four laminates were made by hand layup and were cured at room temperature. No vacuum pressure was applied during the curing of the laminates, as this is not used with the mouldless manufacturing method.

The material properties are therefore considered to be an absolute minimum of the quality that is obtainable. By using better manufacturing methods, such as curing under a vacuum, higher strengths and therefore lower weights could be obtained.

The properties of the bi-directional weaves were assumed to be equal in x- and y-axis, and hence the tension and compression tests were only performed in the x-direction. This saves 50 percent of the samples that must be tested. For the unidirectional weave the tensile and compressive properties were tested in both x- and y-direction. A total of 62 coupons were cut from the laminates. The amount of coupons per test is given in table 6.4. The tensile specimens and in-plane specimens were of 5 plies thick (6 plies were used for the UND in-plane-shear specimens). The laminates for the compressive specimens were thickened to 2.1 mm to prevent buckling during the test.

During the tests no strain gauges and no tabs were used. In the tensile and in-plane-shear test use was made of a bi-directional extensometer to measure the strain. The extensometer was removed before failure and the specimen was tested until failure without accurate strain measurement. A more detailed explanation of the methodology followed during the tests can be found in appendix A.

Table 6.4: Coupons per material and test type

Material	Weave type	Tensile ASTM 3039M	Compression ASTM 6641M	In-plane-shear ASTM 3518M
Interglass 92110	BID	4	6	5
Interglass 92125	BID	4	5	4
Interglass 92145	UND	5+5	8 + 9	6
Sub total:		18	29	15
Total tests:				62

The obtained mean and minimum properties of the materials tests are given in table 6.5. Statistical A- and B-basis values were determined with the help of the "STAT17E2.xls" excel file. In this file the statistical methods of the MIL-HDBK-17-1E are implemented. Due to the low batch sizes the A- and B- material properties were reduced substantially compared to the means. For the A- and B- basis strength values refer to table **??** in appendix A. For proper A- and B- basis values batch sizes around 30 specimens would be required. As it was not possible to test the amount of samples required, due to cost and machine availability, a smaller batch size was selected.

Table 6.5: Material mean and minimum test values

	Mean values			Minimum values			Units
Material	Interglass 92110 BID	Interglass 92125 BID	Interglass 92145 UNI	Interglass 92110 BID	Interglass 92125 BID	Interglass 92145 UNI	
X_t	270.6	235.4	437.7	263.2	222.6	414.9	[MPa]
X_c	244.7	355.7	438.2	200.3	345.3	391.0	[MPa]
Y_t	270.6	235.4	32.6	263.2	222.6	28.0	[MPa]
Y_c	244.7	355.7	96.4	200.3	345.3	87.4	[MPa]
S	88.9	104.3	76.6	82.1	98.6	68.8	[MPa]
E_{x_t}	17.3	18.3	25.1	16.8	18.1	24.2	[GPa]
E_{x_c}	22.8	26.7	36.4	17.5	25.1	34.2	[GPa]
E_{y_t}	17.3	18.3	6.13	16.8	18.1	6.1	[GPa]
E_{y_c}	22.8	26.7	17.1	17.5	25.1	10.9	[GPa]
G	2.44	2.83	2.60	2.41	2.78	2.5	[GPa]
ν_{xy}	0.12	0.15	0.29	0.11	0.14	0.3	[-]
ν_{yx}	-	-	0.08	-	-	0.1	[-]
ν_{45}	0.59	0.58	0.57	0.57	0.56	0.5	[-]

7

Simplified aerodynamic properties of tandem tiltwing aircraft

This chapter provides the reader some background information on the aerodynamics of tandem tiltwing aircraft which are important for understanding the loads that act on such aircraft.

The difference between conventional aircraft and tiltwing aircraft is that tiltwing aircraft have the ability to take-off vertically and transition into a cruise flight. For the tandem tiltwing aircraft the following flight phases can be identified:

1. Take-off, hover and vertical climb
2. Transition
3. Cruise flight
4. Reverse transition
5. Hover, decent and landing

The sizing of a twin wing design for these flight conditions have some specific issues as detailed in section 7.1.

The transition flight phases are the most interesting flight phases as a lot is happening in a short time. The velocity, the wing tilt angle and the thrust level of the engines change continuously throughout the manoeuvre and hence the loads also change continuously during this flight phase. The different flight phases are detailed in the section 7.2 to 7.6. An example of the transition from stand still to cruise flight is represented in figure 7.1.

7.1. Canard & tandem wing sizing issues

The tandem tiltwing configuration poses some interesting design problems in the sizing and positioning of the canard and main wing.

The centre of gravity of the aircraft is required to be approximately in the centre of the canard and wing positions in order to provide adequate VTOL performance. In order to place the motors symmetrically on the wing and canard, the span of both wings must be equal. Hence only the chord length can be used to change the surface area of the lifting surfaces. The surface area of the lifting surfaces is critical for stability and control.

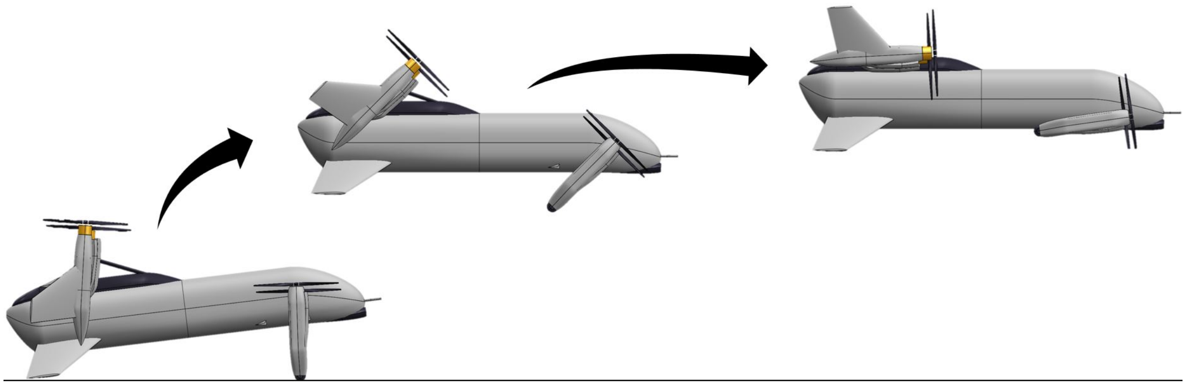

Figure 7.1: Three flight phases: 1. Take-off, hover and climb, 2. Transition, 3. Cruise flight phase.

To have stability the aerodynamic centre or neutral point of the aircraft should lay behind the centre of gravity on the aircraft. Therefore it would make sense to locate the main wing as far aft as possible. However next to the shift in the aerodynamic centre it also pulls the centre of gravity more rearwards. If the wing is placed too far aft, the canard position will start to interfere with the cargo compartment. Hence the wing cannot be placed maximally to the rear of the aircraft.

A canard, or foreplane, is placed in front of the aerodynamic centre and is by definition destabilizing. This moves the aerodynamic centre more forward and reduces the stability margin. Hence it is required that the canard should have the smallest surface area as possible to reduce this effect.

Depending on the velocity of the aircraft, the lift of the canard is 30 to 50 percent higher than that of the main wing. Therefore a higher tilt angle is required on the canard to provide more lift, this increases the tilt angle between the wing and canard which lowers the aircraft maximum lift coefficient. This in turn increases the aircraft's stall speed, which pushes the cruise speed to a higher velocity and therefore more power will be required. This power is limited by the maximum continuous power that the fuel cells can supply. Another reason to have the canard stall before the main wing is to provide a nose-down pitching moment when the aircraft stalls. In figure 7.2 it can be seen that the pressure coefficient on the canard is substantially higher than on the main wing.

Selecting a larger canard surface area therefore reduces the required amount of power, but it decreases stability. The canard position also effects the stability. The canard is placed just in front of the cargo bay such that the best compromise between size and position and between stability and required power is obtained.

Another factor in selecting a suitable canard chord length is a structural reason. A shorter chord length means a lower absolute thickness of the wing, this lowers the moment of inertia and hence the bending stiffness. A thinner wing will therefore require more reinforcements and is therefore heavier than a thicker wing. Since the canard is has more load than the wing and the thickness is lower, the canard is of main interest in the structural investigation.

7.2. Take-off, hover and vertical climb

During take-off no airflow except the propeller slipstream is acting on the airframe. The elevon on the canard trailing edge is submerged in this flow and can be used for yaw manoeuvring while in hover. Compared to the load cases during cruise this load case is very small and hence this load case is not analysed specifically.

During flight testing with a smaller model it became apparent that the elevons have reduced effec-

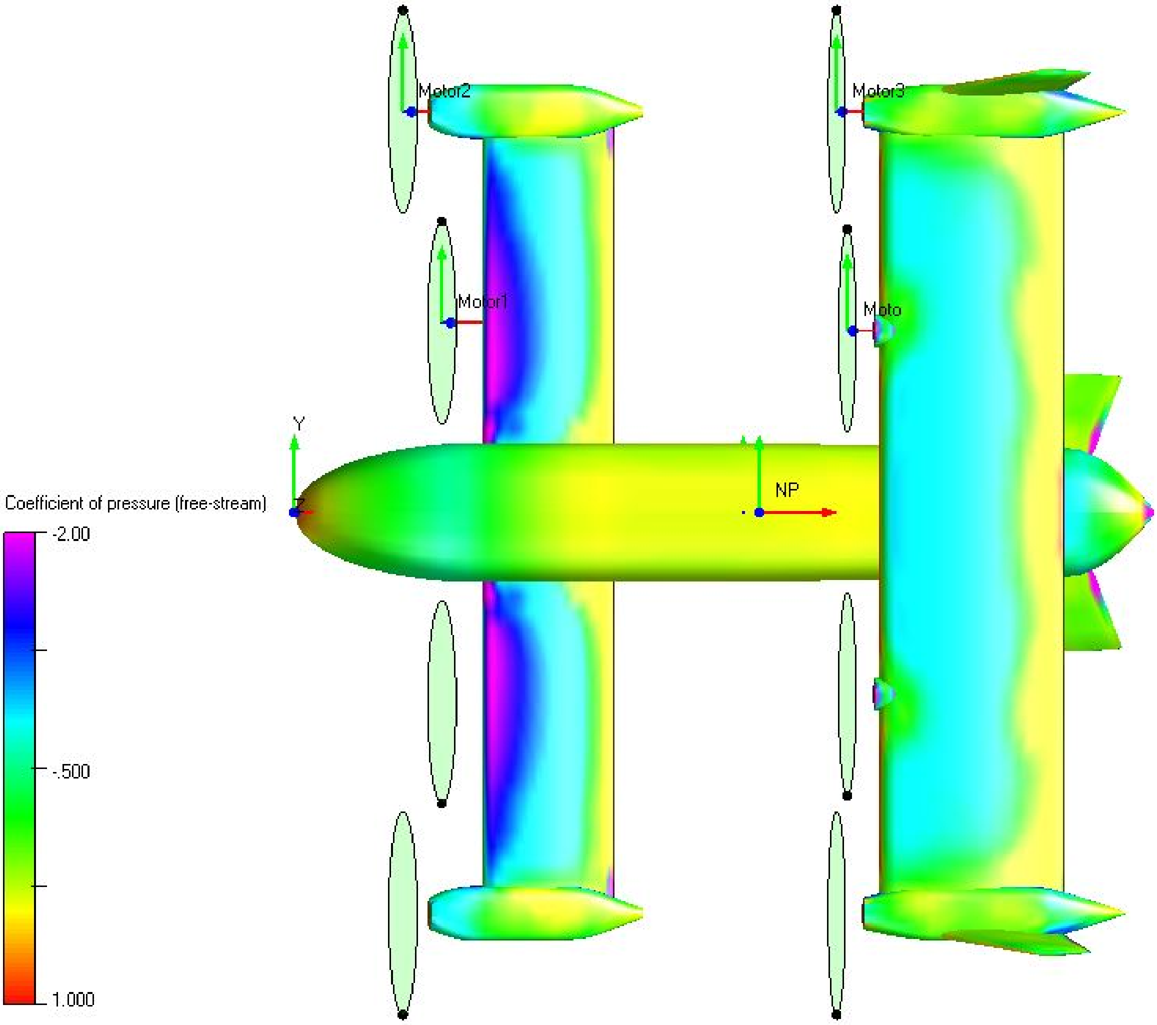

Figure 7.2: CFD analysis performed in FlightStream. Showing a higher pressure coefficient present on the canard.

tively when near the ground due to the disturbed airflow due to the ground effect.

7.3. Transition

In the transition flight phase the wings rotate from their vertical position to the stall tilt angles. The forward component of the thrust of propellers will pull the aircraft forward. However as the wings rotate to a lower tilt angle the vertical component of the thrust decreases, and an increase in thrust is required keep the same altitude. As the aircraft picks up horizontal speed and the wings are rotated further, the wings start to produce lift and simultaneously a lot of drag. As a consequence the tiltwing aircraft will need to increase its power when it goes through a transition phase. The power required will drop drastically as the flow on the wings will become attached. This increases lift and decreases the drag, hence less power is required. This is opposite from helicopters which required most power in hover and require less power at a higher forward velocity albeit much more than fixed wing aircraft.

During the transition the airflow around the aircraft is highly non-linear, due to the separated flow over the wings and the rotational flow due to the propellers. In section 8.4 simplifications are made to estimated the magnitude of the loads during this transition. During the thesis use was made of the FlightStream Vorticity solver. The software was still in development and mainly the post stall load analysis was not correctly captured by the software. No further analysis with FlightStream is made.

7.4. Cruise flight

In the cruise phase both wings are rotated to their respective cruise angle which is almost horizontal (± 10° & 5° for the canard and wing respectively). The wings provide the lift while the motors provide forward thrust. The tilt angles can be used to control and trim the aircraft. For faster reaction the elevons will be used. During cruise the power required by the motors is drastically reduced. In this phase all power will be provided by the fuel cells and the batteries can be charged with the excess power.

7.5. Reverse transition

The reverse transition requires the aircraft to transition from cruise flight back to hovering flight. The velocity should be decreased and the wings are rotated. When the flow will separates the control of the aircraft fully mainly on the motors. The motors will have to keep the aircraft stable during this flight phase even when the wings are not in the vertical position.

Generally speaking the reverse transition is more difficult for VTOL aircraft as the power must remain low to decelerate. One cannot simply power itself through this flight phase as in the forward transition is possible.

Entering the reverse transition to fast and rotating the wings up to stall does increase the loads on the wings. However when the wing stalls this load decreases again, see section 8.4.

7.6. Hover, descent and landing

The aerodynamics during the descent and landing is the same as during take-off. One effect can occur during decent which also troubles helicopters, which is the vortex ring state in which the aircraft flies in its own downwash. This significantly reduces lift and increases the descent rate. This effect is dangerous and cause an uncontrolled impact with the ground.

8

Loads

This chapter introduces the reader to the loads on the airframe of the drone concept. The loads are required to be known in order to perform a successful structural analysis. Where the loads on a fixed wing aircraft are dependent on the speed and angle of attack of the aircraft, the loads on a tilt wing aircraft also depend on the tilt angle of the wing itself. Next to the cruise phase, where the wing is in an equal angle to fixed wing aircraft, two other phases must be analysed which are specific for vertical take-off and landing vehicles. Section 8.1 introduces the different load cases that will be investigated based on the JARUS certification specifications for light unmanned aeroplane systems (CS-LUAS). Section 8.2 describes the VTOL specific load cases and section 8.3 describes the loads during the cruise flight. The transition flight phase is described in section 8.4. Next the torsion loads are described in section 8.5, the chapter is concluded by a section that describe the most critical loads 8.6.

8.1. Introduction

During the lifetime of an aircraft a wide variety of loads act on its airframe. The goal of the load analysis is to determine the most critical load cases such that the airframe can be designed to withstand all the loads that it can expect during its lifetime. Aircraft loads can be subdivided into thee groups: aerodynamic loads, inertia loads and operational loads ([17] & [32]).

The aerodynamic, or manoeuvring, loads are induced by the pressure field on the aircraft which is created by the geometry of the aircraft and the flow conditions present. Different flight conditions within the flight envelope must be analysed. The flight envelope is a diagram that describes the loads that can be expected for each airspeed, this is further detailed in section 8.3.

Inertia loads or dynamic loads are induced by the acceleration of the aircraft. As by Newton's second law each acceleration of mass requires a force in order to induce that acceleration. Components of mass in the airframe therefore induce loads in opposite direction of the acceleration. For example, if the aircraft makes a 5g pull-up manoeuvre the motor will require a force to accelerate with the same amount. The force on the motor is upwards and is transferred from the structure to the motor. With respect to the structure's frame of reference this force by the motor can be seen as a downwards force on the structure. Each upward acceleration therefore induces a downward force on the structure and vice versa. By placing a mass such as the motor pods on the wing tips the induced inertia loads relief the bending moment induced by the aerodynamic loads.

Operational or handling loads occur due to the use of the structure and include loads such as loading, unloading, transportation, handling and other loads that are induced during the lifetime of the structure [17]. This chapter focuses only on the aerodynamic and inertia loads.

8.1.1. Load cases

Each load or a combination of loads can be seen as a load case. Often thousands of load cases must be analysed in order to determine the most critical load cases. It is useful when the amount of load cases that must by analysed is reduced such that a more manageable sub-set of load cases is left in order to reduce the computational time required to analyse the load cases. During the reduction of the set of load cases one must be careful that only load cases are removed which are not critical anywhere in the structure. For example, an inertial load of the tip motor pod might only induce a small bending moment on the wing root. But on the tip the shear load will be larger than the aerodynamic loads, hence this load case must not be neglected for that area.

The certification specification states which load cases *must* be investigated, however these specifications might not include all load cases. It is therefore the job of the designer or load specialist to find the most extreme loads such that the structure can deal with all the loads during the life of the structure.

The load cases that will be looked at in this thesis are:

• Hover	CS-UAS.2215 [25]
• One engine off- conditions	CS-UAS.2215 [25]
• Landing	CS-LUAS.471 [23]
• Maximum positive and negative load factor	CS-LUAS.333 [23]
• Rolling conditions & aileron deflection	CS-LUAS.349 [23]
• Transition loads / high lift devices	CS-LUAS.345 [23]

From these load cases the most critical load cases will be determined. Each load case can induce a combination of five principle loadings on the wings: three moments and two shear loads. The sixth load, the load in the y-axis direction (along the length of the wing) is assumed to be small and is therefore neglected. The five principle loadings are:

- Bending due to thrust and drag around the z-axis
- Bending due to lift and mass around the x axis
- A torsion around the y-axis.
- A shear load due to thrust and drag in x-direction
- A shear load due to lift and mass in z-direction

The axis system used is fixed with respect to the wings and assumes the x-axis to be in chord-wise direction, the y-axis in span-wise direction and the z-axis to be in the out-of-plane direction. The origin is located on the leading edge of wing at the symmetry plane. In figure 8.1 the positive directions of the loads (shears and moments) on the canard are indicated.

The main focus of this chapter will be on the loads on the canard, as canards will have a higher wing loading while having a lower structural thickness. This higher wing loading follows from two design requirements: the canard must stall before the main wing does, and the canard or foreplane must be as small as possible as a larger size has an increased destabilizing effect on the aircraft.

8.2. VTOL configuration

In the VTOL configuration the wings are pointed upwards to provide vertical thrust for take-off, hover and landing. See figure 8.2 for a basic diagram of the forces and moments acting on the airframe during hover.

The main loads in this configuration act in the x-direction inducing a bending moment around

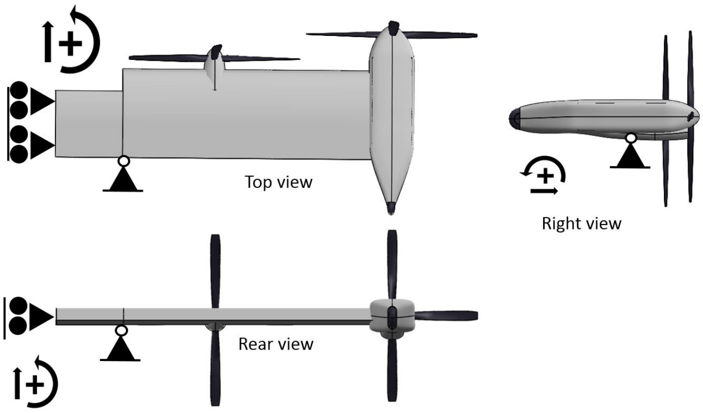

Figure 8.1: Top, rear and right side view of the canard indicating the positive directions for bending, shear and torsion loads.

the z-axis. A small bending moment around the wings x-axis is present due to engine torque of the motors. In steady flight the torque cancels and no resultant is present hence the load will be neglected.

The flight conditions covered in this section are the hover & climb, one engine off conditions and landing conditions.

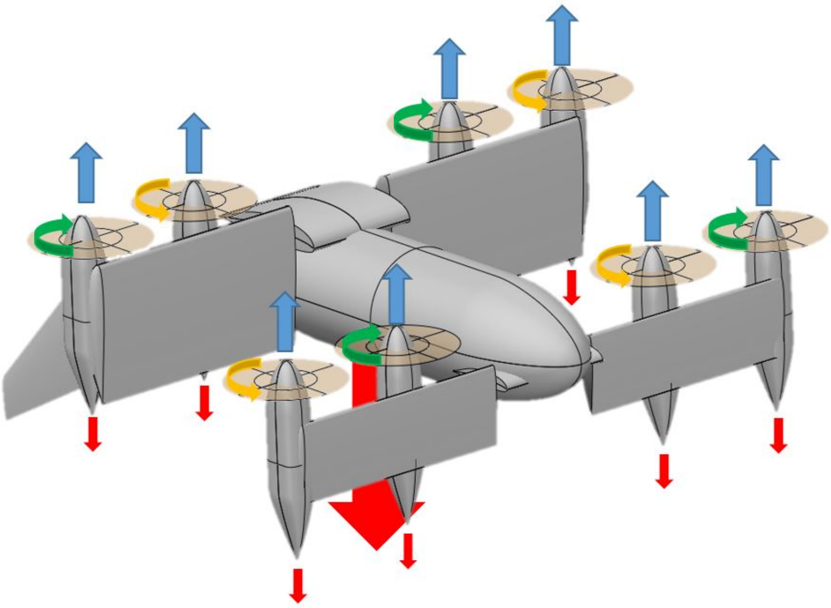

Figure 8.2: Loads and moments due to motor power during hover. Blue (thrust), red (reaction force due to mass), green (torque -), yellow (torque +).

8.2.1. Hover & climb

In the hover flight phase the entire weight of the aircraft is supported by the thrust generated by the propellers. The pressure loads acting on the aircraft surfaces are the static pressure due to the absence of flow velocity. As the static pressure force is present on all sides the net effect is zero. However, in the prop wash a velocity is present and pressures are generated. Some propellers are offset slightly from the wing. Therefore a small pressure differential acts across the wing in hover. Resulting in a small shear force in z-direction. This effect is small and hence it can be neglected in a structural perspective. For a flight dynamics perspective it cannot.

The effect of torque of the motors have to be taken into account for the design of the motor mounts but are negligible compared to the wing bending moment in cruise. The mass of the wings themselves are neglected but the mass of the motor pods are included, this mass acts as a load alleviation.

When the elevons are deflected on the canard during hover the airflow over the control surface will induce a small force on the wing. This force depends on the deflection of the control surface but will mainly be used in asymmetrical mode to improve control in yaw. Figure 8.2 shows the forces acting on the aircraft during the hover flight phase. Note that the torque on each motor mount acts in the opposite direction compared to the rotation of the propeller.

Firstly, lets look at the equilibrium in longitudinal direction, see figure 8.3. The only forces acting on the aircraft are the thrust of the propellers and the mass of the aircraft. As the state is in equilibrium statics can be used. The required thrust on the canard and wing can simply be calculated by summing up the forces and moments and setting them equal to zero.

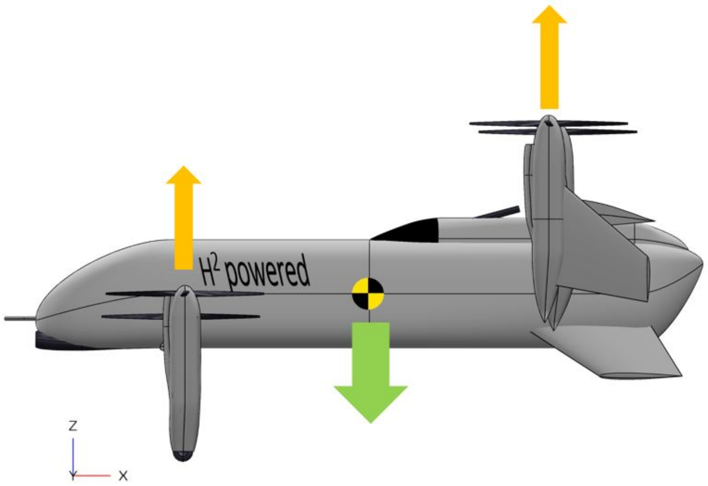

Figure 8.3: Simplified free body diagram in longitudinal direction.

If T_c and T_w are the total thrust of the canard motors and wing motors respectively and L_c and L_w are the distances between the centre of gravity and the canard and wing respectively. Then force equilibrium dictates that:

$$\sum F = 0 = T_c + T_w - \text{MTOW} g_0 \tag{8.1}$$

Moment equilibrium dictates that:

$$\sum M = 0 = T_c L_c - T_w L_w \tag{8.2}$$

Solving these two equation with two unknowns results in:

$$T_w = \frac{\text{MTOW} g_o}{\left(\frac{L_w}{L_c} + 1\right)} \qquad \& \qquad T_c = \frac{\text{MTOW} g_o}{\left(\frac{L_c}{L_w} + 1\right)} \tag{8.3}$$

As the centre of gravity is almost in the middle of the canard and wing the thrust from the motors are almost equal. As the vehicle must be able to climb vertically, a larger force is required than the hover thrust. Henceforth is the vertical climb load case more critical than the hover load case. It is assumed that the vertical climb thrust is a factor 1.2 of the hover flight phase. This results in an initial acceleration of $(1.2-1)\cdot 9.81 m/s^2 = 2.0 m/s^2$.

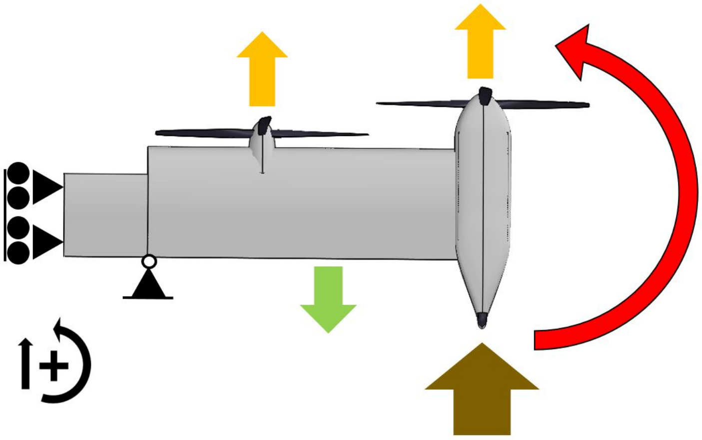

Figure 8.4: Top view of the canard with shear in X-direction due to thrust, mass and landing loads. Induced moment in red.

When looking at a single wing, the individual load per motor is assumed to be $1.2 \cdot T/4$. The maximum shear force in the wing during hover is therefore (neglecting mass effects):

$$S_{max} = 1.2 \cdot T/2 \tag{8.4}$$

At the attachment point a shear load acts in the opposite direction. As the wing is symmetric the moment remains constant between the two attachment points. The maximum moment in the canard is therefore:

$$M_{max} = 0.3 \cdot T_c \left(l_{\text{tip}} + l_{\text{inner}} - 2l_{\text{attach}}\right) = 0.3 \frac{\text{MTOW} g_o}{\left(\frac{L_c}{L_w} + 1\right)} \left(l_{\text{tip}} + l_{\text{inner}} - 2l_{\text{attach}}\right) \tag{8.5}$$

$$M_{max} = 0.3 \frac{50kg \cdot 9.81 \frac{m}{s^2}}{\left(\frac{0.47m}{0.48m} + 1\right)} (0.75m + 0.4m - 2 \cdot 0.1m) = 72.7 \text{ Nm} \tag{8.6}$$

For the shear and moment distribution, as given in figure E.1 & E.4, the effect of the motor pod mass, and acceleration were taken into account. Hence the total maximum moment reduced to 53.2 Nm.

8.2.2. One engine off conditions

The vehicle must be able to continue safe flight with one engine failing. In cruise flight this would pose little issues as the thrust can easily be generated by the other seven motors while maintaining force and moment equilibrium. During hover the loss of one engine is more critical. During the hover mode, the pitch, yaw and roll control of the aircraft are performed by the motors. By increasing or decreasing the rotational velocity of the propellers the trust and torque of the motor can be varied. Speeding up the clockwise turning propellers while simultaneously decreasing the speed of the counter-clockwise turning propellers results in a counter-clockwise moment while keeping the total thrust equal. This moment will cause the aircraft to yaw. Increasing the thrust on one side of the aircraft will cause the aircraft to roll, or pitch.

A failure of one motor means that the lift and torque of that motor is removed. The other seven motors must still provide equilibrium, this requires a state in which the power per motor is non-trivial. This rescheduling of the power is however, outside the scope of this thesis.

As the total thrust or shear must remain equal, it can be assumed that the tip motor must provide the thrust of two motors. This would be the most extreme loading, hence most conservative. The bending moment would be increased by the ratio $\frac{2L_{\text{tip}}}{L_{\text{inner}}+L_{\text{tip}}}$. Which is roughly 1.36 for the current configuration. The shear and bending diagrams of the canard and wing can be found in figure E.1, E.4, E.5 & E.8.

8.2.3. Landing conditions

During a normal VTOL landing the loads change gradually from the hover flight conditions to the static ground conditions. CS-LUAS.722.b (Landing Gear, general) specifies that "*the landing gear must be designed to prevent in normal operations any damage to the structure and systems of the RPA that could result in a subsequent catastrophic condition or reduce the required reliability of the RPA.*" The hard landing condition is required to ensure that the vehicle will stay intact during landings with a significant descent velocity, this is covered in CS-LUAS.471 General (Ground loads) and Appendix H of the CS-LUAS [23]. Appendix H can be used to determine the reaction loads for conventional gear configurations. The appendix is deemed applicable albeit the landing gears are on the tips of the canard and the ventral fins. It must be noted that the CS-LUAS is written for fixed wing aircraft and hence the landing procedure is substantially different,

The aircraft can touch down in three different attitudes:

1. A normal landing in which the canard and tail touch down simultaneously;
2. A horizontal landing in which the canard touches down first;
3. And a tail first landing.

As the aircraft approaches vertically with the fuselage in a horizontal position, a hard landing will most likely impact on the canard first, followed by a rotation after which the ventral fins will touch the ground. Therefore the main loading will occur on the canard gear. The impact on the landing gear creates shear in x-direction and a bending moment around the z-axis of the wings. A simplified free body diagram can be seen in figure 8.4 and 8.5. It is assumed that the canard gear will take-up all the load of the landing. The load is therefore overestimated and deemed conservative. Lower acceleration values can be used when a drop test is used to determine the actual limit landing load factor.

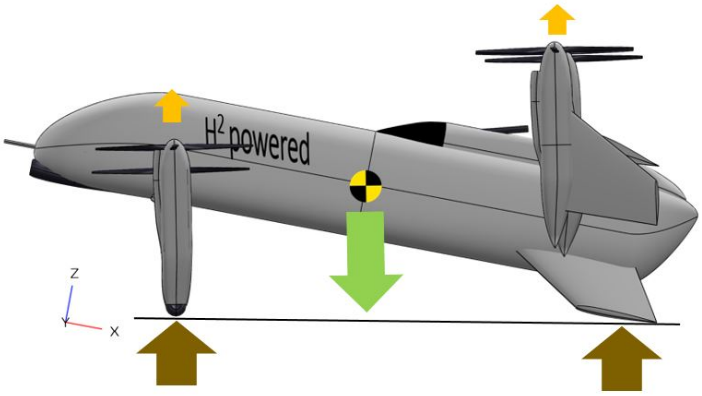

Figure 8.5: The aircraft in ground position. Loads acting on the aircraft during landing.

The static landing gear loads can be calculated by means of moment and force equilibrium:

$$F_{\text{can}} = \frac{\text{MTOW} \cdot g_0 \cdot d_{\text{cg-ventral}}}{d_{\text{can-ventral}}} = \frac{50kg \cdot 9.81m/s^2 \cdot 0.72}{0.95m} = 316\text{ N} \tag{8.7}$$

$$F_{\text{ventral}} = \text{MTOW}g_0 - F_{\text{can}} = 50kg \cdot 9.81m/s^2 - 316\text{N} = 174\text{ N} \tag{8.8}$$

8.2.4. Landing impact

To proof compliance with the regulations (CS-LUAS H.2 [19]) the landing gear must be able to withstand a drop test with the following descent velocity:

$$V = 0.51\left(\frac{Mg_0}{S}\right)^{0.25} = 0.51\left(\frac{50kg\cdot 9.81m/s^2}{0.98m^2}\right)^{0.25} = 2.41m/s \tag{8.9}$$

Where M is the mass, g_0 is the gravitational acceleration and S is the total wing surface area. The required descent speed is limited by 2.13 and 3.05 m/s in the regulations. The drop height to reach this descent velocity is equal to:

$$h_{\text{drop}} = 0.0132\sqrt{\frac{Mg0}{s}} = 0.0132\sqrt{\frac{50kg\cdot 9.81m/s^2}{0.91m/s}} = 0.296m \tag{8.10}$$

As given in [19]. Which equals a total energy of 145 Joules at the maximum take-off weight.

The method for estimating the limit load factor for the landing gear impact based upon the book of Gratton, Initial airworthiness, [19, Ch.7]. A spring mechanism will be installed in the tip pods to reduce the peak loads of the landing gear on the aircraft and canard. It is assumed that the spring behaves linearly with displacement, F = -K $\cdot\delta$. The energy stored in the spring should absorb most of the drop energy and then dissipate it in the dampers. Rewriting the spring equation results in a total deflection that the spring must compress in order to absorb all the energy, $E_s = k\delta^2$. With this equation the maximum displacement and load can be obtained by substituting the total kinetic energy and solving for the displacement.

$$\delta = \sqrt{mg_0h/k} \tag{8.11}$$

The obtained displacement is used to obtain the total load on the airframe. According to CS-LUAS H.2.c two thirds of the wing lift might be assumed to exist throughout the landing impact. As no lift is present the thrust will be substituted here in stead of lift. Hence the thrust can be subtracted from the total load resulting in:

$$F_{max} = k\cdot\delta - \frac{2}{3}mg_0 = \sqrt{mg_0hk} - \frac{2}{3}\text{MTOW}g_0 \tag{8.12}$$

It can be clearly seen that the spring stiffness is the main parameter that can be varied to influence the maximum load. Lowering the spring stiffness decreases the load but it also increases the required deflection. Inversely setting a maximum deflection results in a specified stiffness. A stiffness of 23.5 N/mm was chosen to limit the deflection to 79 mm and a peak load of 1522N. Selecting a larger deflection would reduce the impact loads however due to going to values beyond 79 mm deflection leads to very large sophisticated landing gear to allow the amount of travel. It must be noted that this load is for both gears hence the individual load at each gear is halved, also the spring stiffness of each individual gear is halved (761N and 11.8 N/mm). Table 8.1 shows the parameters for the landing gear loads at empty and maximum weight.

8.2.5. Canard shear and moment distribution due to landing loads

Now that the loads are known on the gear itself, the shear and bending moment distributions in the canard can be calculated. The only shear forces at play are inertial loads due to the motor pods masses, the motor thrust and the landing gear load. The shear and moment distribution can be calculated along the wing:

$$S_i = S_{i-1} + \frac{2}{3}T_c - m_{\text{pod}}\cdot g_0\cdot G_{\text{impact}} \tag{8.13}$$

$$M_i = M_{i-1} + S_{i-1}\cdot\delta_b \tag{8.14}$$

Table 8.1: Landing gear loads. Stiffness used 23.5 N/mm (11.8 N/mm per gear spring)

	MTOW	OEW	Units
Drop height	0.296	0.264	[m]
Impact speed	2.41	2.28	[m/s]
Energy stored	145	104	[J]
Deflection	0.079	0.066	[m]
G load	3.1	3.3	[G]
Load per gear	761	650	[N]
Average speed	1.92	1.84	[m/s]
Impact time	0.041	0.036	[s]

The moment is simply the integrated value of the shear of the span of the wing. As the shear only changes on the locations of the motor pods and the wing attachment, the resulting moment distribution is therefore bi-linear. The maximum shear load in the wing is 787 N which induced a bending moment peaking to 520 Nm. For a symmetrical loading the bending between the attachment points remain constant and the load on the attachment point is 787 N. The shear and bending moment diagram can be seen in figure 8.6.

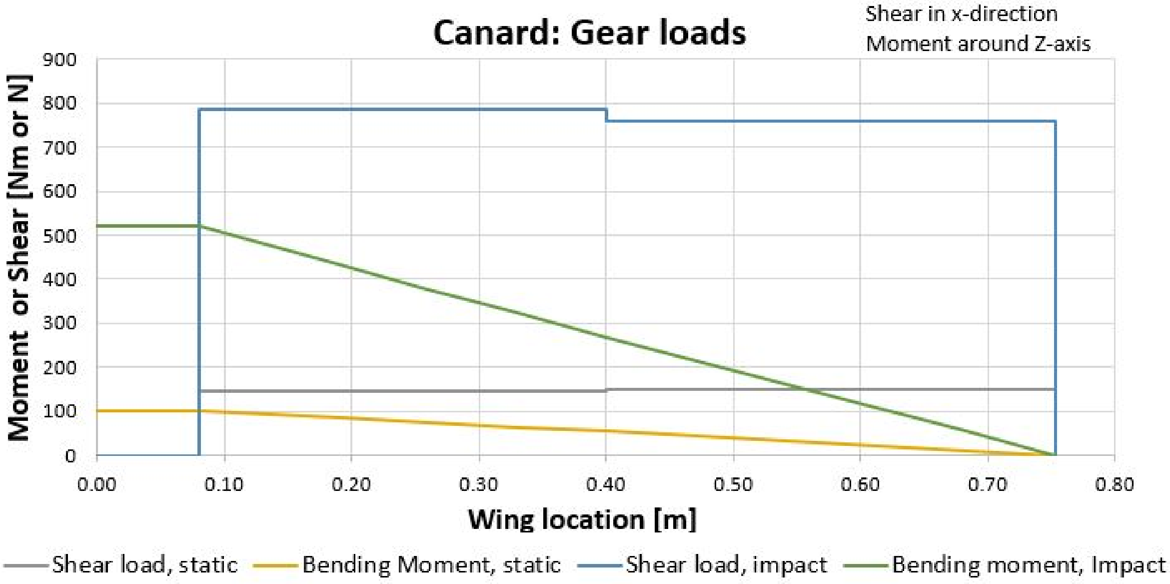

Figure 8.6: Shear and bending moment diagram of the static and symmetric impact loads on canard landing gear. The wing location of 0 metres represent the vehicles centreline.

The symmetrical load on the canard due to the landing impact, on both the left and right gear simultaneously, is not the most critical one. CS-LUAS H.6 describes the landing loads for one-wheel conditions. The same load as for the symmetric impact is used but it must only be applied to one side only, in this example we impact the right gear only. This results in a non-symmetric loading in the canard. The load of the gear must be put in equilibrium by the rotation and the loads on the main wing attachments. Hence large loads are induced at the attachment points.

In the calculation of this load case, the shear and bending moment induced by the motor thrust and the mass on the non impacted side are taken into account. This results in small shear and moment at left attachment, see figure 8.7. The loads are unchanged on the impacted side (attachment point 2). Hence the bending and shear distribution does not change between the impacted gear and the attachment point. In between the attachment points no load is applied and hence the moment changes linearly. Moment equilibrium around attachment the right attachment point and left attachment point respectively can be used to determine the reaction forces on the attachment points:

$$F_{left}F_1 = \frac{M_2 - M_1}{2 \cdot d} - S_1 = \frac{520Nm - 7.5Nm}{2 \cdot 0.080m} - 26N = 3.18kN \tag{8.15}$$

$$F_{right} = F_2 = -\frac{M_2 - M_1}{2 \cdot d} - S_2 = \frac{520Nm - 7.5Nm}{2 \cdot 0.080m} + 787N = -3.99kN \tag{8.16}$$

$$\tag{8.17}$$

The loads at the attachment point are given in table 8.2.

Table 8.2: Canard attachments: internal and external load. The external shear is the applied load on the main wing bolts acting from the wing onto the fuselage.

Load	Attachment 1	Attachment 2	Unit
Internal shear	26	787	[N]
Internal bending moment	7.5	520	[Nm]
Required external shear	3.18	-3.99	[kN]

It can be observed that the loads on the attachment points are significantly higher for the one wheel landing case than the symmetric case. The high loads become especially clear when looking at the shear diagram in figure 8.7.

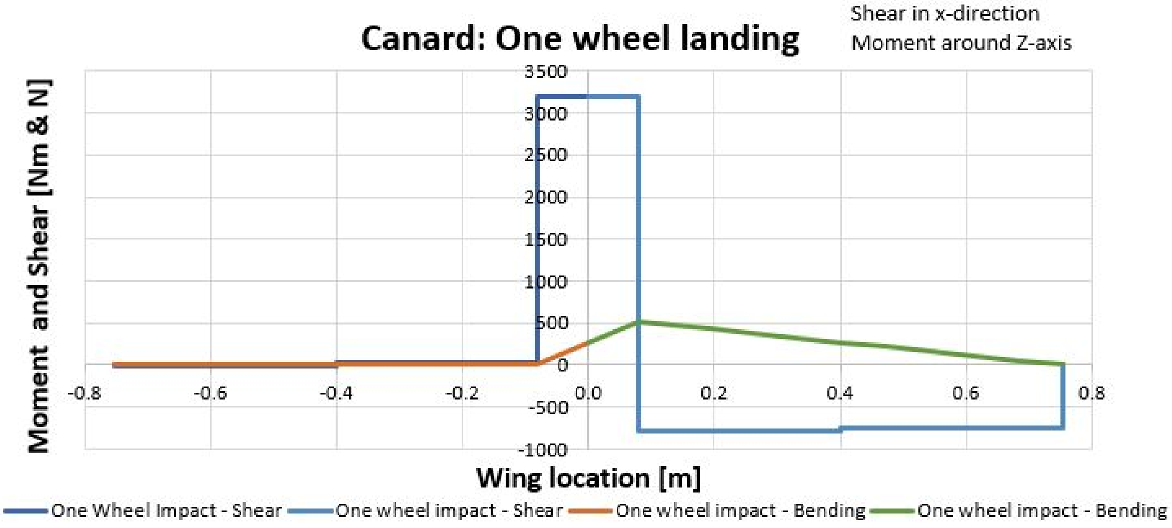

Figure 8.7: Shear and bending moment diagram of the canard during the landing on a single gear.

It is debatable if the landing impact loads on one gear are reasonable. Firstly the regulations are written for conventional landing aircraft in mind and hence the landing approach is completely different. Secondly the impact time would be longer than estimated as the vehicle starts to rotate when the canard landing gear is prevented from moving further down. The centre off mass will move further down until the tail gear(s) will touch the ground. Now that the rotational motion is stopped the full loads will develop albeit lower than if one landing gear is assumed to take up all the loads in a shorter time.

Other loads such as spin up and spring back are neglected as no landing with forward velocity would be possible with the current gear configuration. To decrease the loads on the canard the landing gear could be mounted to directly to the fuselage. This would require a long gear leg, which increases the weight and drag of the aircraft, and reduces the ground stability. One benefit of the tilt wing is that the landing loads are in the direction of the largest structural depth. The moment of inertia is a lot larger in x-direction compared to the z-direction hence the required stresses to handle the large bending moment are reduced.

Albeit no landing gear is present on the main wing, the acceleration would induce inertial loads on the wing structure. These loads are however much lower than the loads in the canard. See figure E.5 for the induced shear loads.

8.3. Cruise configuration

In cruise configuration the loads acting on a tandem tiltwing aircraft are almost similar to the loads on fixed wing aircraft. To first step to determine the loads on an aircraft is to construct a *flight envelope*. The flight envelope, as determined by CS-LUAS.333 Flight Envelope, graphically shows all the combinations of airspeeds and load factors that can be attained. The strength requirements of subpart C of the CS-LUAS must be complied with for the different corners of the flight envelope. All combinations of load and airspeed within the flight envelop should therefore not result in any damage. In figure 8.8 and 8.9 the flight envelope for operating empty weight and maximum take-off weight are given respectively.

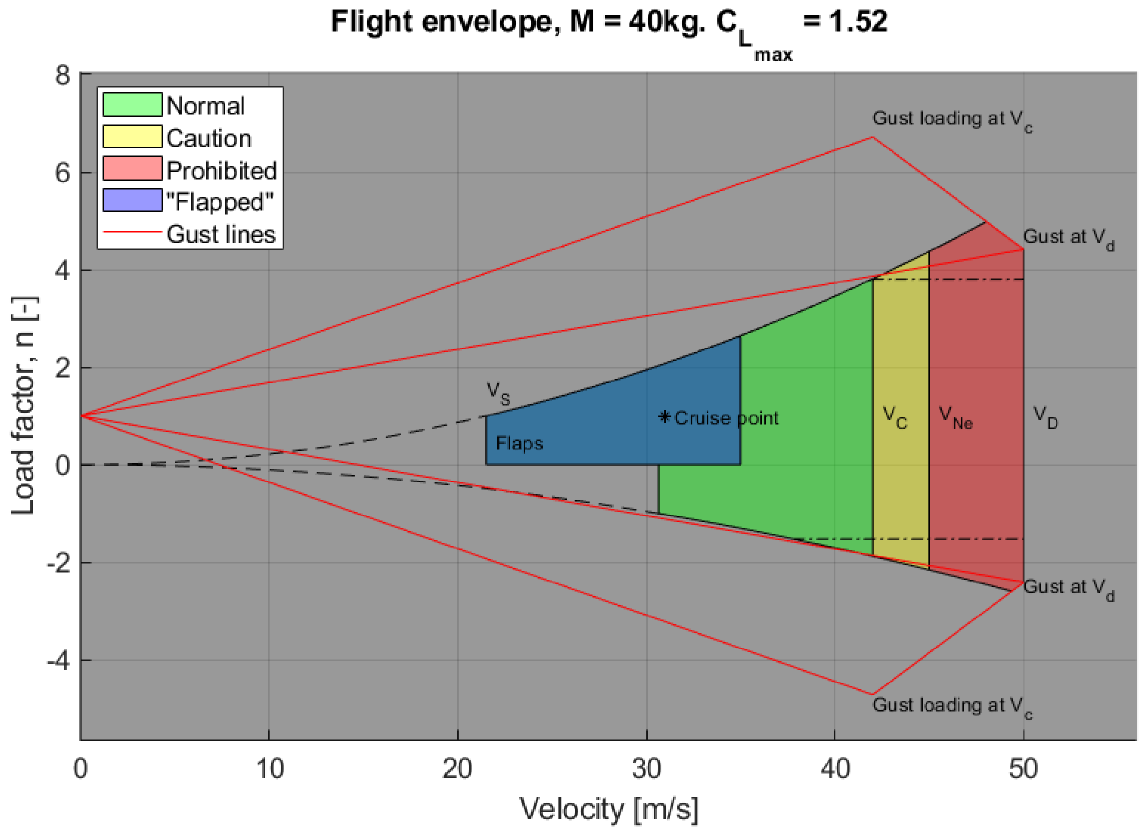

Figure 8.8: Flight envelope for empty weight. Including manoeuvring load diagram and gust loading diagram. Note the higher gust loading due to the decreased wing loading. N_{max} = 5.0, N_{min} = -2.6

Due to the absence of a stall speed requirement a special kind of flight envelope is obtained which might look weird or even incorrect without any explanation. The wings size of the vehicle is, unlike other concepts, not sized by the stall or landing distance requirements but only for the cruise speed

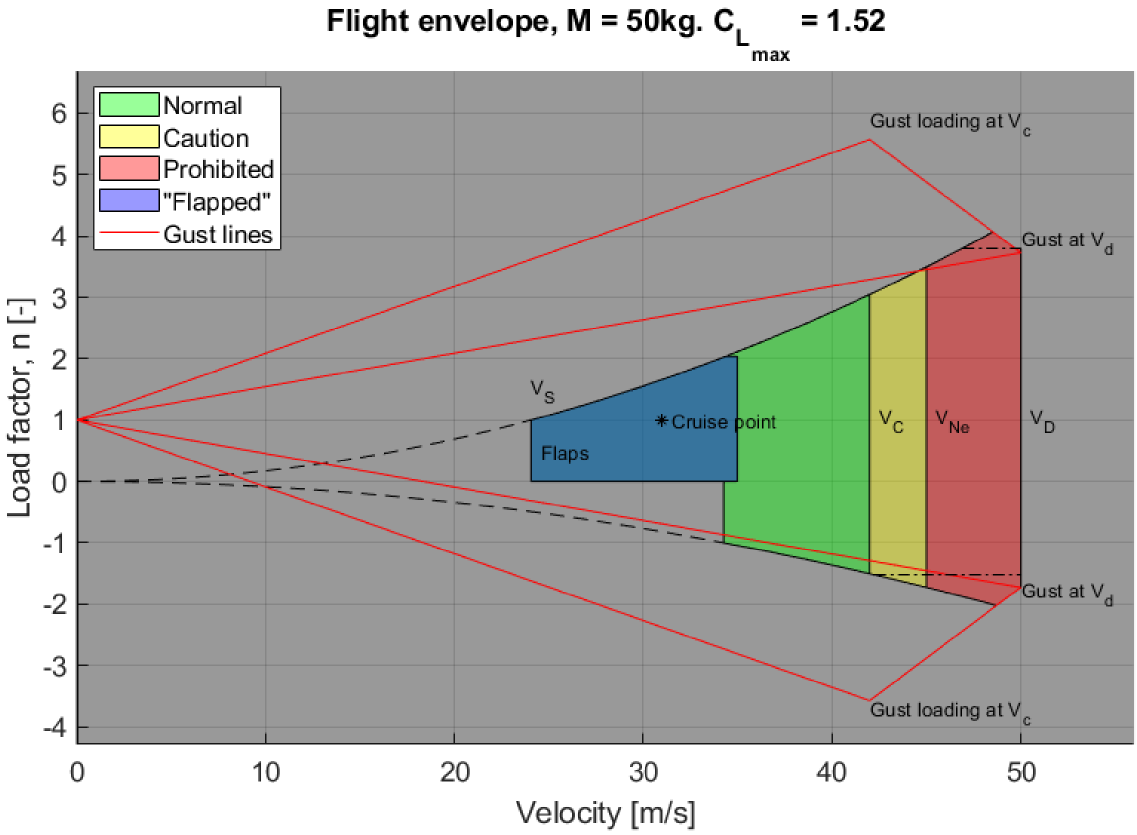

Figure 8.9: Flight envelope for MTOW. Including manoeuvring load diagram and gust loading diagram. N_{max} = 4.1, N_{min} = -2.0.

requirement. The wing is therefore just big enough to lift the aircraft during cruise flight. The result is an efficient airframe with low cruise drag. A structural benefit is that high load factors cannot be achieved at cruise speed as the wing will stall before such loads can develop. It can be observed in figure 8.8 and 8.9 that almost the entire flight envelope is limited by the high speed stall curves. This prevents the aircraft from being overstressed by gusts. Only at speeds above the never exceed speed are the gust load factors limiting and can the full loads be developed.

In the creation of the flight envelope the assumption is made that the maximum aircraft lift coefficient is 1.52. This is a result from the analysis performed with the performance sheet which was created during my internship [35]. Higher lift coefficients are attainable by the individual wings, but when the canard reaches it maximum lift coefficient the angle of attack reduces which limits the total attainable lift coefficient of the entire aircraft. More information on the manoeuvre diagram and gust envelope, and assumptions used to create the flight envelope can be found in appendix B.

The next three sections present the loads due to the maximum positive and negative load factors, rolling conditions and due to control surface deflection during the cruise phase.

8.3.1. Maximum positive and negative load factors

The maximum positive and negative load factors can be retrieved from the flight envelope. It can be noted that the maximum load factor for the OEW configuration is higher than for the MTOW configuration (5.0,-2.6) versus (4.1,-2.0) respectively. In a first glance the OEW condition looks therefore more critical. However, the total load is the load factor multiplied by the mass. The lower weight reduces the effect of the higher load factor and in the end the absolute loads are almost equal.

Another observation that can be made from the flight envelopes is that these load factors can only be attained when the aircraft flies faster than it would be allowed, above the never exceed speed. On cruise power the maximum speed that the aircraft can reach is around 35 m/s, which is well below V_c and V_{NE}. Hence only in a dive can these speeds and load factors be achieved.

For the calculation of the maximum and minimum loads, the load factors are rounded up to 4.5 and -2.5 at MTOW conditions based on the flight envelopes to allow for some increase in weight of the aircraft. The loads on canard and wing are calculated in the following way; during the sizing of the lifting surfaces the moment equilibrium requires the canard and wing to produce no moment. The size, location and wing incidence angles were changed to find equilibria at different airspeeds. For each speed a different combination of wing and canard incidence angles are found. At cruise speed the canard provides 63 percent of the total lift and the wing 37. For the maximum speed this changes to 66 versus 34 percent.

As the canard has a shorter chord length, and hence a smaller thickness the loads in the canard will be the most critical. The thickness of the canard is with a 17 percent thick airfoil only 42.5 mm. The resulting shear and moment diagrams for the maximum positive and negative load factors can be seen in figure E.2 & E.3 for the canard and figure E.6 & E.7. In the calculations the relief effect of the motor pod mass was taken into account.

The maximum shear force was found to be 598 N and 232 N for the canard and wing respectively, inducing bending moments of 205 Nm and 68 Nm respectively.

8.3.2. Rolling conditions

CS.LUAS-349 describes the requirements with respect to the rolling conditions. Asymmetrical loads must be assumed. Both the wing and its supporting structure must be able to handle these loads.

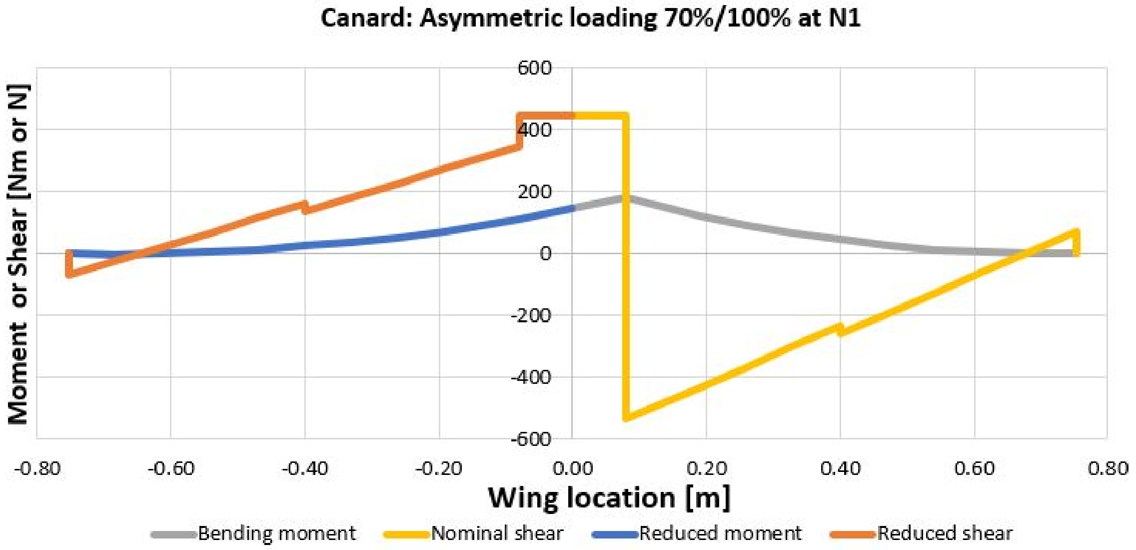

Figure 8.10: Canard: Shear(in z-direction) and bending moment diagram due to asymmetric loading 70/100% (left/right respectively) N1 = 4.5G's. No safety factor applied. Note the large shear loads on the wing attachment to transfer the moment to the fuselage.

The specifications states that one wing must carry 100 % of its load while the other wing carries only 70% with respect to the symmetrical loading condition at the manoeuvring speed determined in CS-LUAS.333. This results in a lower shear and bending moment than the load described in the previous section. However due to the asymmetry a large moment must be transferred to the fuselage this results in large loads at the wing attachments. See figure 8.10 for the shear and moment diagram for the asymmetrical loading. It can be seen that especially the loads at the attachment on the side of the fully loaded wing is substantially larger than the wing with the lower loading.

8.3.3. Aileron deflection

CS.LUAS.349.b specifies (via CS-LUAS 455.a.2.i) to analyse the load due to a sudden aileron deflection. These must be estimated at a load factor of at least two thirds compared to the maximum positive manoeuvring load factor at the manoeuvring speed (V_a). This load induces a significant differential load and a torsion moment which the wing attachment and rotation mechanism must handle.

As the manoeuvring speed (48.5 m/s) is much larger then the design cruise speed of 32 m/s, the load case seems unlikely to occur during normal operations. The aileron deflection is modelled as an increase and decrease of the local lift coefficient of the canard during a pull-up of two-third the limit manoeuvring load. An aileron effectiveness of $C_{l\delta a} = 0.015$ per degree is assumed, based on the example 23-1 in Gudmundsson [17]. This results in a local lift coefficient of $C_{l_{ail.defl.}}$, of 2.0 and 0.96 at 12 degrees down and 12 degrees up aileron respectively.

$$\begin{aligned} C_{l_{ail.defl.}} &= \text{MIN}\left(\frac{2}{3} n_{max}\left(C_{l_{Va}} + \delta_a \frac{\partial C_l}{\partial \delta_a}\right), C_{l_{max_{flapped}}}\right) \\ &= \text{MIN}\left(\frac{2}{3} 4.5\left(0.5 + 12 \text{ deg} \cdot 0.015 \text{ deg}^{-1}\right), 2.4\right) = 2.0 \end{aligned} \tag{8.18}$$

The instantaneous deflection of the ailerons results in an asymmetrical loading in which the vehicle is not in equilibrium. For analysis purposes it is assumed that the situation is quasi-static such that force and moment equilibria can be used. This is deemed conservative as the loads builds up slowly in time which result in lower forces. See figure 8.11 for the bending moment and shear diagrams for the canard. It can be observed that the side of the downward ailerons as the largest force on the wing attachment.

The torsion load due to the aileron deflection is estimated in section 8.5.

8.4. Transition configuration

The transition flight phase is the phase where the vehicle changes from vertical flight to horizontal flight, or from horizontal to vertical flight. The transition is not specifically described by the certification specifications. However under CS-UAS.2210 & CS-UAS.2215 the structural loads must be determined for all flight load conditions and hence also the transition flight phase.

The transition flight phase has a limited speed window in which the transition will be performed. This speed window is from zero velocity to the maximum speed at which the transition will be performed. This is set to 30 m/s, which is 5 m/s above the stall speed. The flight controller makes sure that this speed will not be exceeded. Due to the low wing area and the consequent high stall speed, the possible load factor that can be attained at this speed before the wing will reach its maximum lift coefficient is low. Refer back to the flight envelope, figure 8.9, for a visual representation of the load factors versus velocity. One can see that at the cruise speed a load of only 2 G's can be attained.

To model the loads during the transition flight phase two methods are used. In the first method, described in section 8.4.1, the post-stall resultant force coefficients are estimated for different angles based on interpolated wind tunnel data of airfoils. The second method, described in section

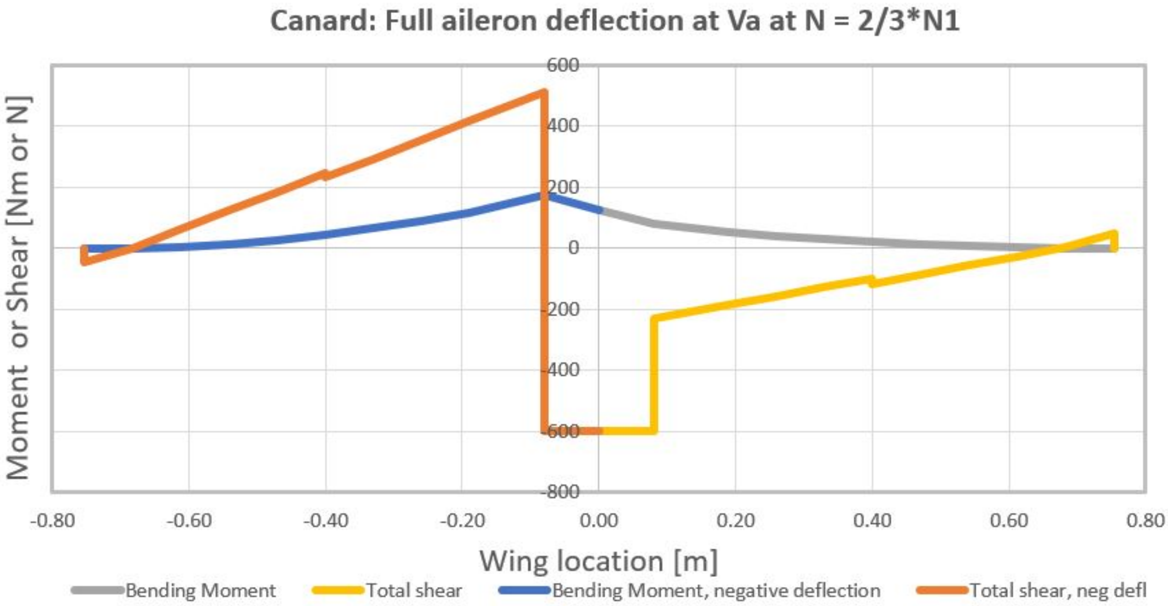

Figure 8.11: Canard: Shear and bending moment diagram due to aileron deflection -10/+10 degrees (left/right respectively) at 2/3 *N1 = 3G's. No safety factor applied. Note the large shear loads on the wing attachment to transfer the moment to the fuselage.

8.4.2, is to use the FlightStream flow solver to solve the pressure distribution and obtain the loads by integrating the pressure distribution.

8.4.1. Airfoil post-stall resultant force coefficient estimation

The lift and drag coefficients in the post-stall region for NACA 44xx airfoils was measured in the windtunnel by Naik and Ostowari [8, 1985] and for seven symmetric airfoils by Sheldahl and Klimas [41, 1981]. These reports were produced with the design of wind turbines in mind. This section estimates the lift, drag and resultant coefficient based on the NACA 4418 airfoil data from the report. This airfoil is comparable in thickness to the selected airfoil but it has a lower maximum lift coefficient.

Looking at the lift curves shown in figure 8.12 two segments can be identified; a 'linear' range until the maximum lift coefficient, and the post-stall range. The airfoil stalls after it has reached its critical angle of attack with its corresponding maximum lift coefficient. At stall angle of attack the lift drops from the 'linear' curve to the post stall curve. By further increasing the angle of attack the lift coefficient increases again in the post stall regime, where it peaks and gradually decreases to roughly zero as flow reaches 90 degrees angle of attack. For thick and cambered airfoils the post-stall maximum lift coefficient is lower than the linear maximum lift coefficient while for thin uncambered airfoils the opposite it true. The selected airfoil is 19 percent thick and hence the linear maximum lift coefficient is the absolute maximum. The drag coefficient does not show a two regime behaviour, the drag increases gradually to a maximum when the flow is perpendicular to the airfoil.

The effect of finite length wings lowers the amount of lift and increases the total amount of drag. As Naik and Ostowari summarize in their report: *"The lift and post-stall drag coefficients decrease with decreasing aspect ratio. The lift coefficient decreases with decreasing thickness ratio while the drag coefficient increases. In the post-stall region both lift and drag coefficient are relatively insensitive to Reynolds number effects and the range tested."* [8, 1985]

The lift curve can roughly be approximated by two parabola's, one from the zero angle of attack lift coefficient to the maximum lift coefficient, and one parabola approximating the post stall lift coefficient. The post stall parabola can be of the form:

$$C_L(\alpha) \approx \left(C_{l_{max_{poststall}}} - C_{L_0}\right)\left(\frac{\alpha - \alpha_{cl_{max_{ps}}}}{\alpha_r}\right)^2 + C_{L_0} \tag{8.19}$$

Where $\alpha_{cl_{max_{ps}}}$ is the angle of the maximum post stall lift coefficient and α_r is the half width (or radius) of the parabola at $C_l = 0$. Both angles seem to be roughly 45 degrees for most airfoils, but they can be tweaked to obtain a closer fit. In the same manner the linear lift coefficient was interpolated. The parameters used to describe the NACA 4418 airfoil with an aspect ratio around 9 are: $C_{L_{max}} = 1.3$, $C_{L_0} = 0.25$, $\alpha_{cl_{max}} = \alpha_r = 22$ degrees, $C_{L_{max_{ps}}} = 0.83$, $C_{L_0} = 0$, $\alpha_{cl_{max}} = \alpha_r = 44$ degrees. For the NACA 4418 airfoil and some other airfoils a linear interpolation from 70 degrees and higher seems to be more accurate then a parabola.

The drag coefficient reaches its maximum when the wing is perpendicular to the flow. The maximum post stall drag coefficient, $C_{D_{max_{poststall}}}$, varies per airfoil and is dependent on the wing aspect ratio and thickness of the airfoil. According to the test data $C_{D_{max_{poststall}}}$ varies between 1.3 (for low aspect ratio's and high thickness) and 2.1 (for high aspect ratio's and lower thickness). For the NACA 4418 airfoil 1.45 was used for an aspect ratio of 9. The post stall drag coefficient can be approximated by:

$$C_D(\alpha) \approx \frac{C_{d_{max_{poststall}}}}{2}\left(1 - \cos(\alpha)\right) \tag{8.20}$$

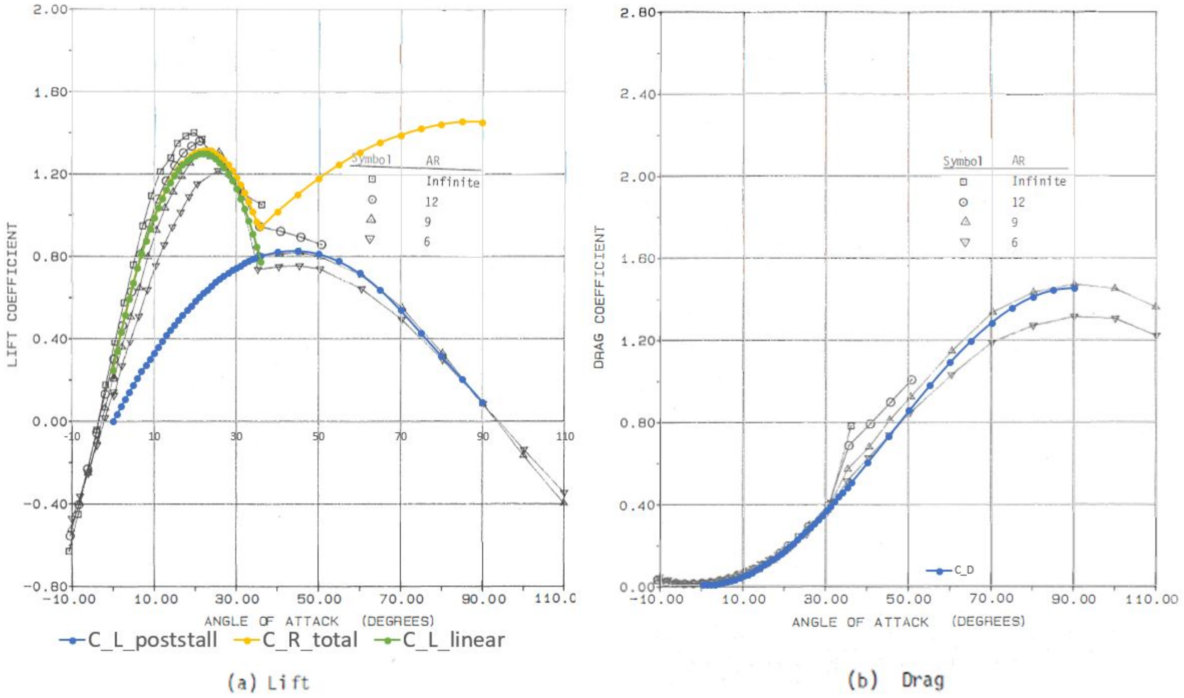

(a) Lift (b) Drag

Figure 8.12: Post stall, lift coefficient and drag coefficient interpolated on wind tunnel data [8, Fig. 35.A & 35.B] of a NACA 4418 airfoil, Re = 1e6. The resultant force coefficient is plotted in the subfigure (a).

The resultant force coefficient, is the combination of the lift and drag force. It can be obtained by simply applying Pythagoras' law: $C_R = \sqrt{C_L^2 + C_D^2}$. See figure 8.12 for the interpolated lift, drag and resultant coefficients versus angle of attack. It can be observed from the figure that the resultant coefficient has two maxima, one at the maximum lift coefficient and one at 90 degrees angle of attack. For the selected airfoil the maximum lift coefficient will be higher and hence the peak at stall will be the absolute maximum. The airfoil has a maximum lift coefficient of approximately 2.1. The lift coefficient of the entire wing was estimated to be 1.8 and the post stall lift coefficient was estimated to be 1.4 The wing and canard have an aspect ratio of 4.3 and 6.0 respectively. Now that the peaks of the resultant force coefficient are known, the total force induced on the structure must be estimated. The force on the structure scales with the dynamic pressure:

$$F_r = \frac{1}{2}\rho V^2 C_R S \tag{8.21}$$

During a normal transition the forward flight velocity is increasing while the wing and canard angle of attack are decreasing. Roughly speaking the angle of attack of the wings will decrease linearly with an increase in velocity. With a zero forward velocity the wing angle attack is 90 degrees while at stall speed the stall angle of attack will be achieved, ± 15 degrees.

If the resultant force and resultant force coefficient are plotted against the velocity, see figure 8.13, then it becomes clear that when the linear tilt schedule is used the peak of the resultant force coefficient does not induce any significant loads due to the low dynamic pressure. At higher speeds the loads increase and reach the 1G limit when the stall speed is reached. This load case will be the same as the one for the maximum positive load factor as described in section 8.3.1 albeit lower.

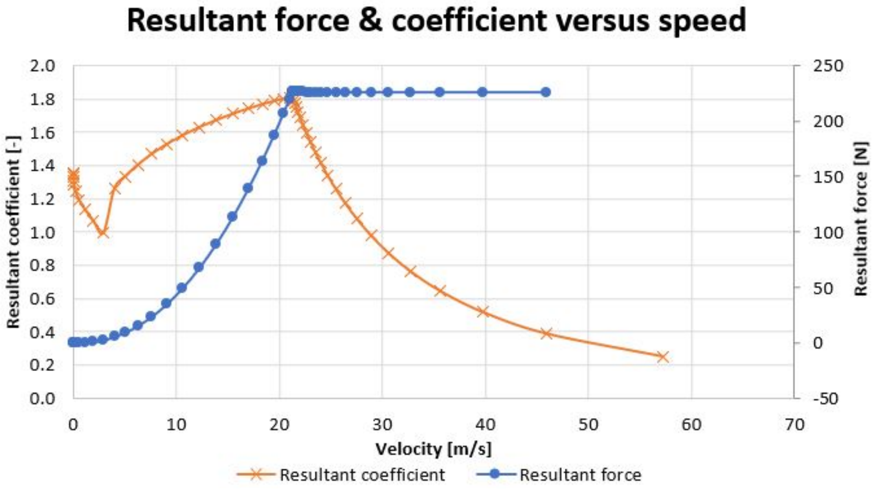

Figure 8.13: The resultant force on the entire aircraft obtained by $F_r = \frac{1}{2}\rho V^2 C_r(v) S_{total}$ plotted against airspeed for non accelerated flight. It becomes clear that when a normal tilt schedule is used no large loads occur due to the angle of the wings.

High lift device loads Due to elevon and the full rotation of the wing and canard, both lifting surfaces can be seen as a high lift device. CS-LUAS 345 high lift devices describes the certification specifications that must be met for such devices. The most important requirements are that the analysis must take into account a maximum deflection of the high lift device at the maximum flap speed, a limit positive load factor of 2, a positive and negative gust of 7.6 m/s acting normal to the direction of flight.

At this condition the load factor and the gust direction are in the vertical direction. As the wings are vertical as well no load can be induced due to the gust and hence only the airflow perpendicular to the wing is considered. The velocity is the maximum flapped speed set at 35 metres per second. This is a highly unlikely scenario as the wing need to rotate instantly to such a condition as the drag will reduce the velocity rapidly. Even though it is an unlikely load case, the load case is not critical as the maximum positive manoeuvring load induces higher forces. The drag coefficient for NACA 4418 wing with an aspect ratio of 6 with the comparable thickness is around 1.5 when the flow is perpendicular to the wing. This is lower than the maximum lift coefficient. Hence at the maximum manoeuvring load case from section 8.3.1 is higher than the load due to the perpendicular flow.

As the wing is rotated 90 degrees the only critical load from this load case is the load into the fuselage which is acting in the x-direction instead of in the z-direction. The load is therefore critical on the attachment structure. The load is incorporated as the 'Transition pure drag' case in figures E.2, E.3, E.6 & E.7.

8.4.2. Flow analysis

Another more detailed method to estimate the loads during the transition is by using a computational fluid dynamics package to obtain the pressure distribution on the geometry and integrating those pressures to obtain loads. The flow solver available is FlightStream. FlightStream is still in development and three different versions of the software were used; 11.2, 11.4 and during the last stages of this thesis the beta version of FlightStream 11.6. The version 11.2 was unable to perform flow separation analysis and was therefore unusable for estimating post stall performance. Version 11.4 already made it possible to estimate the stall angle as separation was modelled. Still not all effects such as vortex roll-up and spanwise flow are modelled and hence no accurate predictions can be made. These functionalities are being added on a contractual basis by NASA. Version 11.6 included many small improvements and a major improvement, which was the immersed boundary solver. This allowes unconnected meshes which intersect each other to be analysed. This simplifies the analysis of a wing fuselage intersection without the requirement or new meshes.

Both FlightStream version 11.2 and 11.4 have been used but with no good succes due to the software limitations. Refer to appendix C for an analysis of the applicability of FlightStream 11.2 and 11.4 for determining post stall load distributions and the differences between the two versions.

8.5. Torsion loads

Torsion is the loading on the wing that wants to twist the wing along it span-wise axis. The pressure distribution over an airfoil induces a moment. All airfoils, except symmetric and some speciality airfoils, produce a negative moment. The specific moment that the airfoil generates depend on the shape and orientation of the airfoil. The more camber an airfoil has the larger the absolute moment. The angle of attack, and hence also the tilt angle of the wing, influences the moment coefficient. Unfortunately no wind tunnel data is known for the selected airfoil. Therefore use should be made of an analysis tools or use wind tunnel data of comparative airfoils. As the NACA 4418 airfoil is roughly equal in thickness and camber, use is made of reported wind tunnel measurements to estimate the moment coefficient of the airfoil in the linear and post stall regime. The report of Naik and Ostawari [8] includes wind-tunnel measurements of in which the C_L, C_D and C_M were determined (among others) for a NACA 4418 wing with an aspect ratio of 6 rotated through -10 to 110 degrees angle of attack. The moment coefficient versus angle of attack curve, see figure 8.14, is slightly increasing in the linear regime. After stall the moment coefficient rapidly decreases linearly in value. The most negative moment coefficient of the airfoil is -0.08 in the linear regime and decreases to -0.4 at an angle of attack of 110 degrees in the post stall regime. The infinite aspect ratio wing has a value of -0.10 and -.65 for most negative values in the linear and post-stalled regime respectively, from [8, Fig. A.1.c]. The pitching moment of other wings and airfoils show the same behaviour in the post stall regime. The steepness of the moment curve slope depends on the aspect ratio of the wing.

The contribution of each wing section to the total moment is calculated by:

$$\begin{aligned}\Delta M_i &= \frac{1}{2}\rho V^2 C_{m_i} S_i C_i + \Delta_{M_{\text{Pods}}} \\ &= \frac{1}{2}\rho V^2 C_{m_i} (b_{i+1} - b_i) C_i^2 + \Delta_{M_{\text{Pods}}} \end{aligned} \tag{8.22}$$

Where $\Delta_{M_{\text{Pods}}}$ is the contribution to the torsional moment of the motor and is calculated by multiplying the mass of the motor pod times the distance from the shear centre times the load factor:

$$\Delta_{M_{\text{Pods}}} = m \cdot d \cdot n \tag{8.23}$$

As the mass is located in front of the shear centre the contribution will be negative if the load factor is positive. The total torsional moment can be calculated by summing up the moments contributions of each section, this is performed in a spreadsheet.

If a wing is not stiff enough multiple unstable modes can occur such as flutter and divergence. Flutter is a dynamic instability while divergence is a static instability. A flutter analysis is outside the scope of this thesis. However due to the low velocity, low aspect ratio and the skin carrying construction it is assumed that the torsional stiffness is large enough to prevent the aeroelastic phenomena from happening. This assumption has to be checked later during flight testing. In the following sections the torsion in the cruise phase and the worst case for the transition flight phase are estimated.

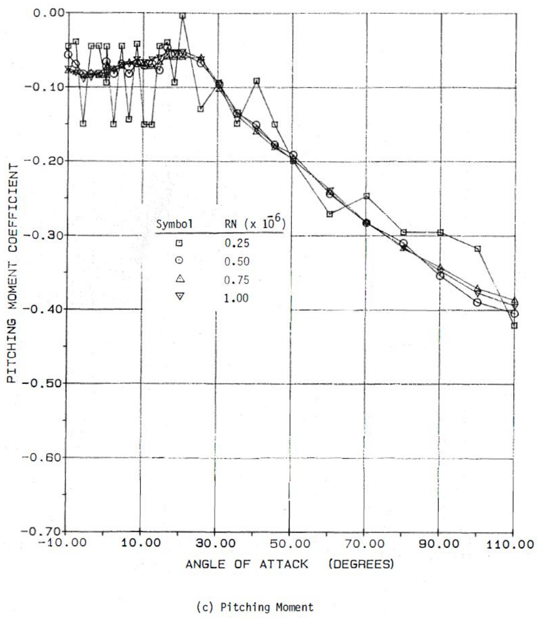

Figure 8.14: Pitching moment coefficient on a wing with aspect ratio 6 and a NACA 4418 airfoil [8, Fig. A.4.c]. A Reynolds number of $0.75 \cdot 10^6$ corresponds to cruise flight.

8.5.1. Shear centre offset

The location of the shear centre of the wing has a crucial influence on torsion and hence on the twist distribution of the wing. When the shear centre is located in front of the aerodynamic centre the lift induces a nose down pitching moment. This pitching moment reduces the angle of attack and reduces the load. This prevents aerodynamic divergence. The other way round when the shear centre is behind the aerodynamic centre the wing increases its angle of attack and hence increases its load. If the wing is not stiff enough in torsion divergence will occur. As described in section 9.2, the structure is idealized as a simple box. The aerodynamic centre is located at the quarter chord point while the shear centre is assumed to be in the centre of the rectangular wing box. See figure 9.1 for a graphical representation. Hence the increment of the moment due to the shear centre offset is:

$$\Delta M_{\text{SC offset}} = L_i \cdot \left(X_{\text{Shear centre}} - X_{\text{Aerodynamic centre}}\right) \tag{8.24}$$

Where the distance between the shear centre and the aerodynamic centre is 20 mm for the canard and 28 mm for the wing.

8.5.2. Torsion during cruise

For the analysis of the torsional moment during the cruise flight in the linear regime a moment coefficient of -0.10 is assumed based on the data from [8]. This value corresponds to the most negative value for the infinite aspect ratio wing and is hence conservative. As the value for the wing with an aspect ratio of 6 is -0.08, and at the stall angle of attack closer to -0.05 this is deemed conservative.

CS-LUAS 349 Rolling Conditions specifies a load condition for torsion due to an aileron deflection. At two-third of the maximum positive load factor a full deflection of the aileron must be analysed at V_a. As the manoeuvring speed V_a is almost equal to the dive speed V_d (see section 8.3), the full deflection at V_a is more critical than the partial deflection required at V_d. According to CS-LUAS 349 the effect of the aileron on the torsion of the wing can be assumed to be modelled by an increase in the airfoil moment coefficient at the location of the aileron equal to:

$$\Delta C_m = -0.01\delta \tag{8.25}$$

Where δ is the deflection of the control surface in degrees [23]. This increment is added to the base moment coefficient, hence the moment coefficient for a certain section is $C_{m_i} = C_{m_0} + \Delta C_m$. For a 20 degree deflection at 3G the moment coefficient for the aileron deflected downwards becomes -0.30. Where the 3g condition comes from the CS-LUAS 349.b requirement, which states *"an aeroplane load factor of at least two thirds the positive manoeuvring load factor"*. The moment coefficient of NACA 64_3-418 airfoil with a 60 degree split flap deflection with a 20 percent chord ratio is given reported by Abbot and Doenhoff [3, P.584] to be -0.30. The NACA 64_3-418 is comparable in thickness and camber, the flap deflection is however larger then the aileron deflection and therefore the estimate seems in the right order.

The moment coefficients assumed for the flight conditions for both the canard and main wing can be seen in table 8.3. Only load case four and five are not applicable for the main wing.

Table 8.3: Torsional load cases

Load case number	Load case		Velocity	Moment coefficient
1	1G;	normal cruise	$V_C = 31$ m/s	-0.10
2	4.5G;	maximum pull-up	$V_D = 50$ m/s	-0.10
3	-2.5G;	maximum push-down	$V_D = 50$ m/s	-0.10
4	3G;	aileron deflection down	$V_A = 48.5$ m/s	-0.35
5	3G	aileron deflection up	$V_A = 48.5$ m/s	0.10
6	1G;	most adverse tilt (90 deg)	$V_{flap_{max}} = 35$ m/s	-0.30

With all parameters known the torsion distributions can be calculated for the different load cases. The calculations were performed in the main calculation spreadsheet. The six analysed distributions are given in figure 8.15. It can be observed that the 4.5G pull up is the most critical on the wing tip while the aileron deflection load case creates the largest absolute torsion loads on the rest of the wing. The torsion on the main wing is slightly less critical as can be seen in figure 8.16.

8.5.3. Worst case torsion during transition

The torsion on the wings during the transition is linearly dependent on moment coefficient and the dynamic pressure. As the moment coefficient scales linear with airspeed and quadratically with the dynamic pressure, a low airspeed results in a low moment irrespective of the moment coefficient. This is same as shown for the resultant force coefficient in section 8.4.1.

The most extreme case for torsion in the transition configuration would be if the wing would be stuck in its vertical position while flying at its maximum flapped speed of 35 m/s. This is the same

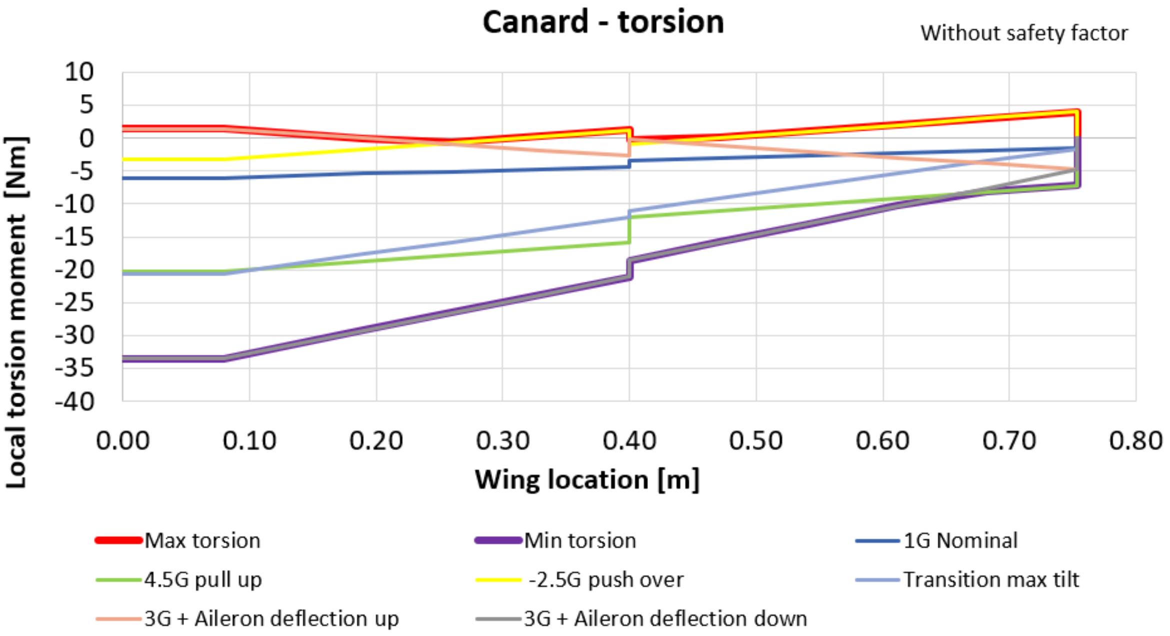

Figure 8.15: Canard torsion distribution due to different load cases without safety factor applied.

case flight configuration as for the high lift devices described in section 8.4.1. A moment coefficient of -0.40 was used to estimate the loads, based on the data from Naik and Ostawari [8] as given in figure 8.14. The maximum torsion moment in the wing and canard are -21.3 Nm and -20.6 Nm respectively, see figure 8.15 and 8.16 and for the torsion distributions.

8.5.4. Actuator loads

The total twisting moment of the wings will be put into equilibrium by the force induced on the linear actuators. The maximum force on the linear actuator that can be expected due to the torsion load conditions on the canard can be calculated by determining the required perpendicular force to the chord line, hence:

$$F_{actuator} = \frac{F_{\perp}}{\sin(\theta)} = \frac{T \cdot sf}{d \sin(\theta)} \tag{8.26}$$

Where T is the maximum torque of the described load cases, $F_{\perp}$ is the force perpendicular to the chord, 'sf' is the safety factor, θ is the angle between the actuator and the chord line and 'd' is the distance between the rotation point and the attachment point of the actuator. $d_{can} = 0.14$ m is for the canard and $d_{wing} = 0.18$ m for the wing. The force in the actuator is dependent on the angle between the chord line and the actuator axis. As the angle decreases the load increases. To minimize the force on the actuator the angle needs to be perpendicular and d must be as large as possible. The angles in the current design are given in table 8.4.

Table 8.4: Actuator extension

	Actuator angle [deg]		Actuator force multiplier [-]	
State	Canard	Wing	Canard	Wing
Retracted	≈90	≈16	$\frac{1}{\sin(90)} = 1.0$	$\frac{1}{\sin(16)} = 3.67$
Extended	≈23	≈30	$\frac{1}{\sin(23)} = 2.54$	$\frac{1}{\sin(30)} = 2.0$

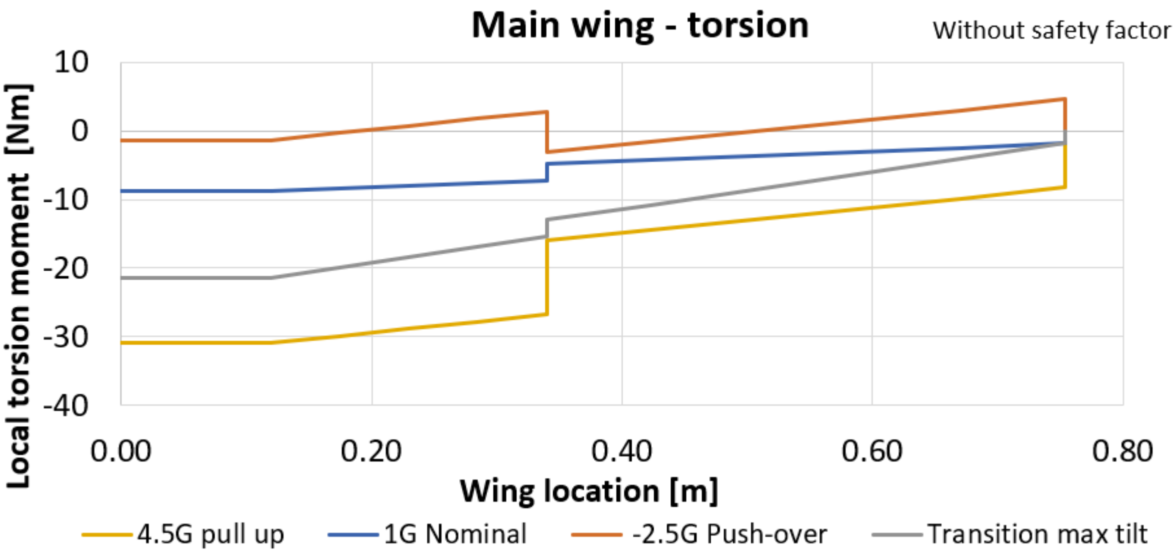

Figure 8.16: Wing torsion distribution due to different load cases without safety factor applied.

The calculations in section 8.5.2 and 8.5.3 only consider the wing until the symmetry plane. To obtain the total moment that the actuator must withstand the double value of the obtained moment distributions must be taken. The elevons can deflect both symmetrically as elevators and asymmetrically as ailerons. When deflected unsymmetrically the total torsion would be the sum of the aileron up and aileron down torsion, T_{ailerons} = -33.5 Nm + 1.4 Nm = -32.1 Nm. For the elevators the double value of the elevon down case would be applicable & $T_{\text{elevators}}$ = 2·-33.5 Nm = -67.0 Nm.

The actuator load for a symmetric full elevator deflection at 3G including safety factor would therefore be:

$$F_{\text{actuator}_{\text{canard}}} = \frac{T_{\text{elevators}} \cdot sf}{d \sin(\theta)} = \frac{-67Nm \cdot 1.5}{0.14m \cdot \sin(90deg)} = -0.72kN \tag{8.27}$$

The actuator loads for all the torsion load cases can be seen in table 8.5.

Table 8.5: Actuator loads canard and wing, without safety factors.

	Torsion [Nm]		Actuator angle [deg]		Actuator load [N]	
Load case	Canard	Wing	Canard	Wing	Canard	Wing
4.5 G pull up	-40.5	-61.8	90	16	-289	-1246
1G Nominal	-12.0	-17.6	90	16	-86	-355
-2.5 push over	-6.38	-2.6	90	16	-46	-53
Max aileron deflection	-32.1	-	90	-	-229	-
Max elevator deflection	-67.0	-	90	-	-479	-
Transition	-41.3	-42.7	23	30	-754	-474

8.6. Critical load cases

This section concludes the loads chapter by selecting the most critical load cases presented in the forgoing sections of this chapter. All the shear and moment diagrams for the canard and wing are presented in this section including all the load cases analysed. See section 8.6.1 for the critical loads on the canard, and section 8.6.2 for the critical loads of the wing. The maximum loads for the cruise configuration on the wing and canard are given in table 8.6.

Table 8.6: Maximum shear, moment and torsion loads for the cruise load cases on the canard and main wing.

	Canard			Main wing		
	Shear-z	Moment-x	Torsion	Shear-z	Moment-x	Torsion
Units	[N]	[Nm]	[Nm]	[N]	[Nm]	[Nm]
Max Pos	598	204	-20	232	68	-31
Max Neg	-332	-114	4	-129	-38	-3
Transition	303	114	-21	333	118	-21
Mass only @ 5g	97	56	-	154	68	-
Mass @-3 G	-54	-31	-	-86	-38	-
Aileron deflect. -	598	127	-	-	-	-
Aileron deflect. +	514	174	-	-	-	-
Unsymm wing loads	598	204	-	232	68	-
Unsymm wing loads	489	165	-	232	68	-

8.6.1. Canard

As discussed in chapter 7 the canard has a higher wing loading than the main wing. The loads are therefore higher on the canard, combined with the smaller structural thickness more material would be required to yield the same stresses. The highest positive and negative loads are given in table 8.7. It can be very well observed that the choice of locating the landing gear on the wing tips has large effects on the loads of the canard. The shear loading in the local x-direction and the bending moment around the local z-axis are higher than the loads of the lift induced shear and bending which act in the z-direction.

Table 8.7: Canard critical load cases

Load -direction		Most critical load case	Maximum positive load	Maximum negative load	Unit	Figure
Shear	X	Landing impact single gear	787	-3203	[N]	E.1
Shear	Z	Elevon deflection & Unsymmetrical loading	598	-598	[N]	E.2
Moment	X	Maximum positive/negative load factor	204	-114	[Nm]	E.3
Moment	Z	Landing impact	520	0	[Nm]	E.4
Torsion	Y	Aileron deflection	4.0	-34	[Nm]	8.15

8.6.2. Wing

The highest positive and negative loads on the wing are given in table 8.8. It can be observed that the loads are much lower than the loads on the canard.

8.6.3. Attachments

Both the canard and wing are supported by three attachment points. One attachment point is driven by the actuator while the other two attachment points form the main attachment around which the wings can rotate. The actuator takes up the torsion loads, these were discussed in section 8.5.4. The most critical loading for the actuator is dependent on the load, the moment arm and the angle between the chord and actuator. Due to current positioning of the actuators very small angles result

Table 8.8: Wing critical load cases

Load -direction		Most critical load case	Maximum positive load	Maximum negative load	Unit	Figure
Shear	X	Hover/hard landing	106	-38	[N]	E.5
Shear	Z	Transition/-2.5G	333	-129	[N]	E.6
Moment	X	Transition drag / -2.5G	118	-38	[Nm]	E.7
Moment	Z	One-engine off/Landing impact	64	18	[Nm]	E.8
Torsion	Y	-2.5G/4.5G	4.6	-31	[Nm]	8.16

in high loads for the wing in the cruise position. A relative small change in the angle from 23 to 40 angle could already reduce the load in the actuator by $\frac{\sin(23)}{\sin(40)} = \frac{0.391}{0.643} = 0.608$ which is a 39% reduction. The reaction loads on the main attachments of the canard and wing are given in table 8.9. It can be observed that the attachment loads on the canard are significantly larger than the attachment loads on the wing. This can be attributed to the landing impact, elevon deflection and asymmetric load case.

Table 8.9: Shear loads on the canard and wing attachment in newtons for multiple load cases.

	Canard		Load direction		Wing	
Load case	Left	Right	Wing	Fuselage	Left	Right
Pull up 4.5G	598	598	z	z	232	232
Push over -2.5G	-332	-332	z	z	-129	-129
Elevon deflection down	-366	1112	z	z	-	-
Elevon deflection up	1112	-366	z	z	-	-
Unsymmetrical wing loading 100-70	1087	-99	z	z	488	-140
Unsymmetrical wing loading 70-100	-99	1087	z	z	-140	488
Hover	148	148	x	z	90	90
Landing impact both gears	787	787	x	z	-38	-38
Landing impact left gear only	3990	-3177	x	z	-	-
Landing impact right gear only	-3177	3990	x	z	-	-
Transition	303	303	z	x	333	333
One engine off	148	148	z	z	90	90
Maximum positive load	3990	3990			488	488
Maximum negative load	-3177	-3177			-140	-140

9

Structural Analysis and Stress Calculations

This chapter presents the structural analysis on the conceptual structure of the drone prototype such that the structure can fulfil the airworthiness requirements concerning strength as described in section 8.1.1. The first section gives a brief background concerning relevant topics for the structural analysis such as the different structural approval philosophies, definitions of the reserve factor, margin of safety and the different failure mechanisms considered. Section 9.2 presents the structural idealization used for the setup of the model presented in section 9.3. The verification and validation of the structural analysis code is performed in chapter 10.

9.1. Definitions and background

Before the structural analysis is presented a couple of topics will be clarified. The first subsection gives the reader some background on the approval of airworthy aircraft structures. In section 9.1.2 the used safety factor and their definitions are given. In the subsections following, the reserve factor, the margin of safety, and the failure modes, and the used failure criterion are described.

9.1.1. Structural approval for airworthiness

The approval of an aircraft structure can be performed in a three ways, as given by Gratton [19]:

- Approval by testing
- Approval by analysis
- Approval by testing and analysis

Approval by testing is a suitable method to demonstrate compliance with the imposed certification specifications. By performing physical tests, one can be certain that the part is strong or stiff enough when the part is subjected to the required load and no failure does occur. However, not all the components in an assembly require the same safety factor. When the structure is proven by testing, the loading has to correspond to the highest safety factor found on that structure. As not all components require the same safety factor, some parts will be tested to a higher safety factor than required. Which means that some parts of the structure must be over-designed in order to prevent failure during the test. A better method would be to test the global structure to a little more than the lowest common safety factor, and to test the individual components according to their own higher safety factor when required [19]. The drawback of this method is that much more tests are required.

In the *approval by analysis* method the structure is analysed analytically only. If all the reserve factors are larger than unity the structure will not fail under the imposed loading. One has to take into account that every analysis is based on assumptions and therefore the accuracy of each method can vary. Simple methods such as tensile yielding of a constant cross-section beam are well defined and could be used to prove compliance with airworthiness specifications. On more complex structures the accuracy decreases and hence larger safety factors are used or a combination of testing and analysis has to be used to verify the method. This holds true for Finite Element Analysis (FEA) and for composite structures for example. In combined testing the analysis is validated by the physical tests to ensure compliance. [19] For this thesis use will be made of the *approval by testing and analysis*. Material tests have been performed in order to determine the properties of the fibre glass reinforcements, see chapter 6. Furthermore a wing with a simplified structure was tested to failure, see chapter 10, in order to validate the tool from this chapter.

9.1.2. Safety factors

A safety factor is a multiplier applied to a certain load in order to ensure that there is a specified amount of margin between the maximum expected load during the life cycle and the failure load. The general safety factor as specified in all airworthiness codes, for example in CS-LUAS 303, as 1.5. The safety factor is multiplied with the limit load to obtain the ultimate load. The CS-LUAS specifies the following safety factors (see table 9.1):

Table 9.1: Safety factors specified by the CS-LUAS [23].

CS-LUAS:	Name	Value	When to apply.
303	General safety factor	1.5	Always
621	Casting factors	2.0	Can be reduced to 1.25 with tests
623	Bearing factors	≥ 1	Part with free fit
625	Fitting factors	1.15	When no load tests performed
657	Hinges	6.67	Except ball & roller bearing. Total SF not below 6.67
693	Joints	3.33	For control system joints
619	Composite special factors		Each of the following if applicable:
AMC 619 2.1	Hot/wet factor	2.0	Elevated Temperature Wet - conditions apply
AMC 619 2.2	Scatter factor	>= 1.0	Or use A- /B- basis values when available
AMC 619 2.3	Manufacturing variability factor	1.2	Unless lower demonstrated
AMC 619 2.4	Special factor	>= 1.0	cover degradation due to damage

The general safety factor must always be used as specified by CS-LUAS 303. In certain cases additional factor must be used which are multiplied with the general safety factor. These additional cases are specified in the certification specifications detailed in the first column of table 9.1. For example, for a composite structure under Elevate Temperature Wet (ETW) conditions a factor of $1.5 \cdot 2.0 \cdot 1.2 = 3.6$, under normal conditions a total safety factor of $1.5 \cdot 1.2 = 1.8$ should be used. These factors seriously degrade the maximum strength that can be used for a certifiable composite structure. An aluminium structure would only require a safety factor of 1.5, excluding degradation due to damage. The difference between the required safety factors therefore varies from +20% to +140% for the normal and ETW conditions respectively. For this thesis to be conservative, a total factor of safety of 3.6 is used to account for ETW and manufacturing conditions.

9.1.3. Reserve factor and margin of safety

The reserve factor (RF) is used to indicate how much 'reserve' a structure has. If the reserve factor is lower than unity failure will occur before it is allowed. Hence none of the reserve factors in the entire structure is allowed to be smaller than one. The reserve factor is defined as:

$$\text{Reserve Factor} = R_f = \frac{\text{Failure Load}}{\text{Ultimate Load}} = \frac{\text{Failure Load}}{\text{Limit Load} \cdot \text{Safety factor}} \tag{9.1}$$

It must be emphasized that the safety factor is not equal to the reserve factor. Sometimes the margin of safety is used instead of the reserve factor. The margin of safety is simply the reserve factor minus one, and should therefore be at least zero:

$$MS = R_f - 1 \geq 0 \tag{9.2}$$

9.1.4. Failure modes

A structure can fail in different ways, as both the structure and the material can fail. The failure of a structure occurs when the structure cannot hold the loads any more due to a loss of stability, simply called buckling. The material will fail when the applied stresses are too high, and the material yields or breaks. The failure criteria used to determine the failure of the composite materials are described in section 9.1.5. Due to the failure of the material, the stiffness of the structure decreases which can induce local buckling with can have a global collapse as consequence. In this analysis only the load at the first failure is of interest. In other words it is assumed that first failure load coincides with the ultimate failure load. The different failure modes that will be taken into account are:

- Fibre tensile failure
- Fibre compressive failure
- Matrix tensile failure (including shear)
- Matrix compressive failure (including shear)
- Failure of the foam core
- Wrinkling/buckling of the skin
- Wrinkling/buckling of the web

The first five failure modes are material failures and the latter two are structural or stability failures. In composites structures many more failure types can occur, such as global buckling, shear crimping, core crushing, facesheet separation and shear buckling. To simplify the analysis these failure modes are not specifically analysed due to the following reasons:

Global buckling is assumed not to occur by itself since no spanwise load is acting on the wing. This does not mean that global collapse cannot occur. If one of the skins buckles the entire wing will bend at that location due to the absence of stringers. This failure is captured by the wrinkling estimations.

Shear crimping, a core failure mechanism, is not specifically analysed in the main program. Due to the use of spar webs combined with the thick core, the resulting failure load for shear crimping is very high. And hence will not be reached. The thick core increases the resistance against shear crimping considerably. Shear crimping for the core without shear webs has the following failure load [26, sec 10.4.2]:

$$N_{xy_{crimp}} = t_c G_{45} = 43\text{ mm} \cdot 5.0\text{MPa} = 215\text{ N/mm} \tag{9.3}$$

As the foam core is mostly isotropic the shear modulus under 45 degrees is assumed equal to the given shear modulus. Even the relatively low shear stiffness of 5.0 MPa for the thick XPS core material results in a much lower load than the failure load, which holds as well when the total safety factor of 3.6 is taken into account;

$$N_{xy_{max}} = \frac{S_{max}}{t_c} = \frac{598\text{ N}}{43\text{ mm}} = 13.9\text{ N/mm} << 215\text{ N/mm} \tag{9.4}$$

Core crushing is neglected in the analysis as no out-of-plane point loads are present. Facesheet separation and peel off tendencies are outside the scope of this analysis but good design practises are used to minimize these effects.

Shear wrinkling or *buckling* of the webs can be analysed conservatively by using the equations for wrinkling under compression (see section 9.3.2) and rotating the laminate by 45 degrees. As the shear loads are much smaller than the bending induced compression, the shear buckling is assumed to be negligible. The validity of the assumptions to neglect these failure modes can be validated by performing a load test on a simple wing geometry. See section 10.2.

9.1.5. Failure criterion: Hashin-Rotem

To predict failure in composite materials many researchers have proposed failure criteria. Common failure criteria used are the maximum stress, maximum strain, Thai-Hill, Tsai-Wu, Puck, Hashin-Rotem. The Hashin-Rotem failure criterion will be used to evaluate failure as the method is computationally fast to perform and it makes distinction between fibre and matrix failure modes. A good overview of the commonly used failure criteria can be found in Kassapoglou [26, Ch.4]

Fibre failure is defined by Hashin & Rotem [47] as:

$$\frac{\sigma_x}{X_t} = 1 \quad \text{(tensile)} \quad \& \quad \frac{\sigma_x}{X_c} = 1 \quad \text{(compressive)} \tag{9.5}$$

Matrix failure is defined to occur in tension when:

$$\frac{\sigma_y^2}{(Y_t)^2} + \frac{\tau_{xy}^2}{S^2} \geq 1 \tag{9.6}$$

And in compression when:

$$\frac{\sigma_y^2}{(Y_c)^2} + \frac{\tau_{xy}^2}{S^2} \geq 1 \tag{9.7}$$

As defined in the report of Hashin and Rotem from 1973, [47]. The reserve factors for the Hashin-Rotem failure criterion can be calculated by:

$$RF_{\text{Fibre}} = \frac{\sigma_x}{X} \tag{9.8}$$

$$RF_{\text{Matrix}} = \sqrt{\frac{\sigma_y^2}{Y^2} + \frac{\tau_{xy}^2}{S^2}} \tag{9.9}$$

Where S is the material shear strength and X and Y are the material strengths in x- and y-direction respectively. Both X and Y strength can be for tension or compression loads when applicable. The strength data used for the analysis is obtained by the material tests as presented in section 6.2. For simplicity of the code the core material also makes use of the Hashin-Rotem failure criterion.

9.2. Structural idealization

This section presents the structural idealization and the setup of the model in order to simplify the analysis of the canard structure.

As described in chapter 4, the canard is a simple non-tapered wing with an elevon. Contrary to common aircraft, where at the thickest location a spar is located, no conventional spar is used. Only a shear spar at 63% of the chord, just in front of the elevon, is used to close the cross-section to provide torsional stiffness and to provide a path for the shear loads of the control surface and the canard actuator. As the Classical Lamination Theory will be used, a simple flat skin panel is easier to analyse then a piece-wise linear airfoil shape. Hence the entire cross-section will be approximated by a wide rectangular beam constructed of a foam core with two face sheets and two closing webs.

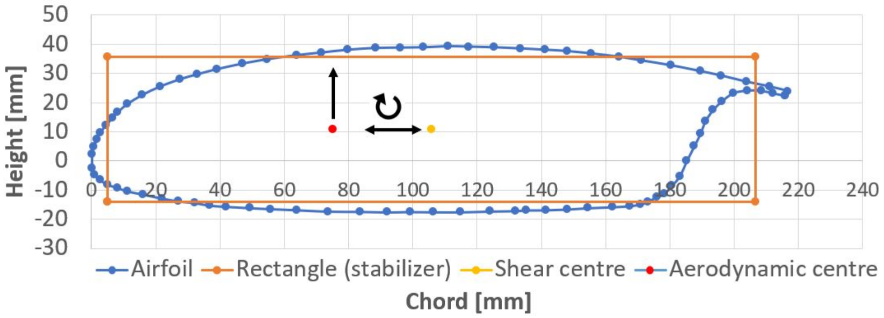

Figure 9.1: Idealized structure versus airfoil cross-section. Airfoil nominal chord = 300 mm, rectangle size: 202 by 50 mm

Figure 9.1 compares the airfoil cross-section without the elevon with the idealized cross-section to be used in the analysis.

The symmetry of the idealized beam in both the x- and z-axis allows for a simplification of the neutral axis and the shear centre, which are located on the horizontal symmetry line and the symmetry point respectively. The wingbox of the canard is sized to have the same second moment of area as the airfoil. To obtain the second moments of area of the airfoil section the tool 'section properties' of Solidworks was used. A 1 mm thick wingbox with a size of 202 mm by 50 mm was found to have equal inertia to the airfoil ($I_{xx} = 2.58{\cdot}10^5$ mm^4 & $I_{yy} = 2.32{\cdot}10^6$ mm^4). At the root the wing has a cut-out to allow the wing to rotate at this section the inertia is reduced ($I_{xx} = 1.96 \cdot 10^5$ mm^4 & $I_{yy} = 0.905 \cdot 10^6$ mm^4) and the wingbox is therefore smaller, being 136 mm by 49.5 mm. The cantilevered beam has the following boundary conditions: the wing is clamped at the wing centre line (y=0), the wing is pinned at the inner wing attachment (located at 80 mm from the centre line) and the tip is free to move.

As mentioned in the chapter 8 there are three configurations for the wings to be in: VTOL, transition and cruise. As the transition load cases were found not to be critical, this configuration was omitted. Only the pure drag loads with the wings in the VTOL position are analysed for a conservative estimation of the loads during transition, note that this load is positioned under the cruise load cases as the direction of the loads with respect to the wing is equal to the load case in cruise configuration. For each configuration three main loads are considered, a shear load, the induced bending load and a torsion load. The loads are in the frame of reference of the wing, hence for the VTOL configuration the shear is pointed to the nose of the airfoil and for the cruise condition the shear is pointed upwards. As the torsion loads are acting around the same axis, the torsion axis is equal for both configurations. Hence 5 different loads act on the structure, of which three simultaneously: a torque, a bending moment and a shear. The internal loads are provided to the code by means of a loads.txt file, which is calculated by the methods presented in chapter 8.

As the classical lamination theory assumes plane stress, it is assumed that the shear load is fully taken up by the faces parallel to the load & the core. The shear in cruise configuration will be taken up by the spar webs and the shear in the VTOL configuration will be taken up by the top and bottom skin. The same does not hold for bending where it is assumed both the skin and webs do contribute to the bending stiffness in cruise and VTOL configuration. Hence two ABD matrices will be constructed, one for the cruise configuration and one for the VTOL configuration. Henceforth also two vectors for the loads are used, see section 9.3.3.

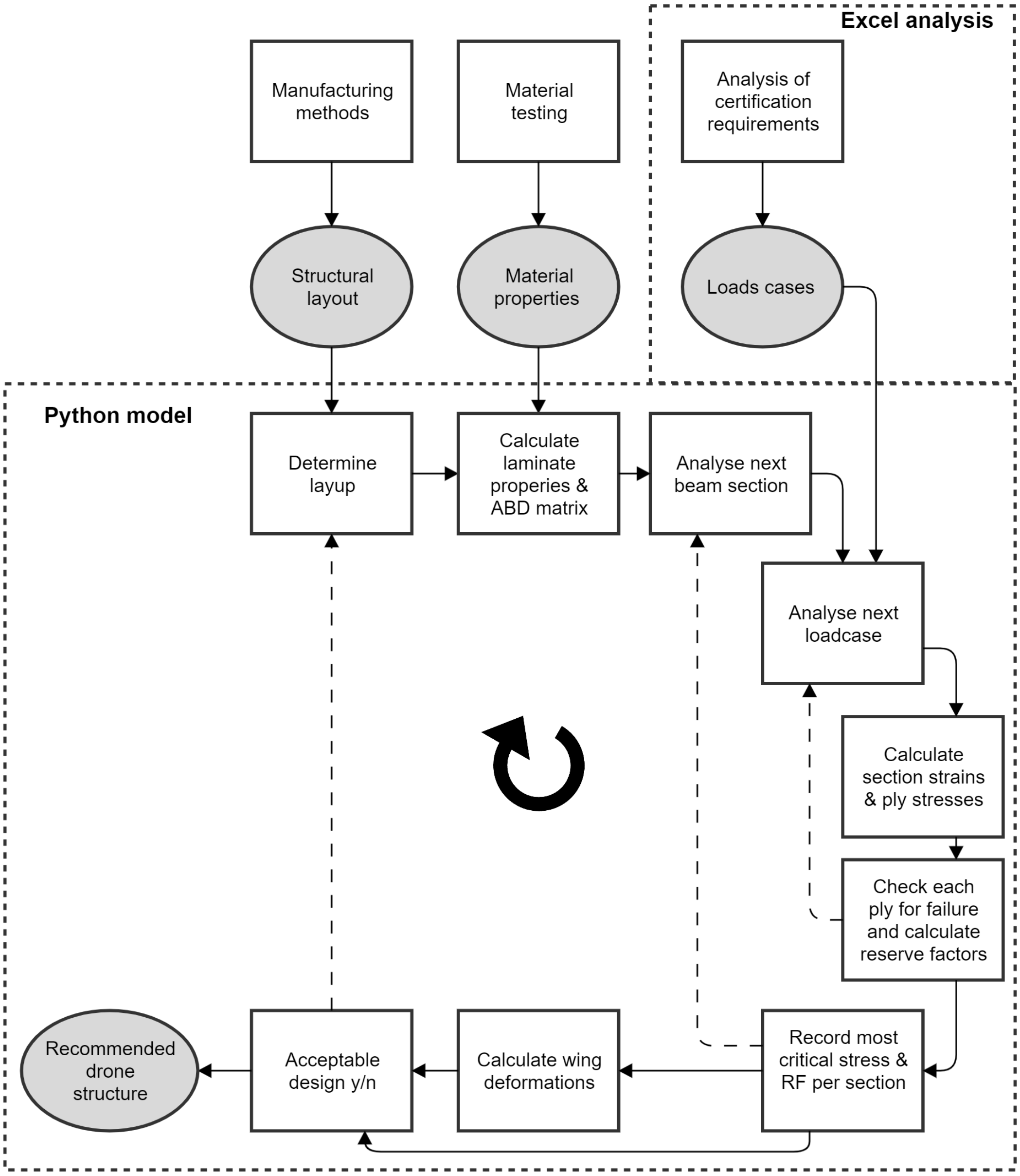

Figure 9.2: Overview of the steps taken and the Python program used in the structural analysis of the wings.

9.3. Methodology

This section describes the method used to analyse the loads of chapter 8 and to calculate the stresses, the failure types and the corresponding reserve factors. Initially the tool was created in Excel for a single loadcase and single spanwise location. The benefit of the Excel tool was that it is a simple tool with a good graphical overview of the failure of each layer. However it was found that the tool would be more useful if multiple loadcases and multiple spanwise locations could be analysed. This functionality was not easy to implement while keeping the Excel sheet simple. Therefore a Python script was written which was able to fulfil this task. Python was chosen over Matlab as Python would be equally capable as Matlab but it has the benefit of being a free software and it is used frequently within Fokker department. Figure 9.2 gives an overview of the steps that are executed in order to complete the structural analysis. The preceding steps of determining the structural layout, the material properties and the load cases have been detailed in chapter 4, 6 and 8 respectively. In the next sections, 9.3.1 to 9.3.8, the workings of the Python program are detailed.

9.3.1. Program overview

The overview of the Python program, given in figure 9.2, shows the steps that the program takes to analyse the different load cases. The program iterates through all loadcases and wing sections and determines the stresses in all the plies. The Python program was written in Python version 3.7.4.

To set up the program the following steps need to be performed manually. Firstly the beam properties must be inserted followed by the material properties. This includes beam equivalent width, height and the required safety factor. The material is added in the MaterialProperties array and follows the following convention:
['Name','Weave',$X_t, X_c, Y_t, Y_c, S, E_{xt}, E_{xc}, E_{yt}, E_{yc}, G, V_{xy}, T_{ply}, \rho$].

The main Excel tool used during the sizing of the drone was extended to automatically create the loads presented in chapter 8. The loads are automatically grouped together in the Excel sheet where they can be copied easily and inserted in a .txt file. The user must specify the right load file which can be placed in the same folder as the main Python file. After the set up the layup must be inserted. The arrays: SkinLayup, BotSkinLayup and WebLayup must be filled. The bottom skin layup is kept symmetrical to the top skin. The web layup array must also include the core if used. After the layup has been determined, the program can be run. After the results are presented the user must verify that all the reserve factors are at least 1.0. If not, then failure occurs before it is allowed and hence the layup should be altered such that the sections of interest will not fail. No option to enter different layups at different locations was yet integrated.

When the tool is run, the program executes the following steps:

1. Initialize variables, define thickness vectors, concatenate the layup vector
2. Calculate laminate properties, the critical buckling strains & ABD matrices, see section 9.3.2.
3. Loop through all beam sections while:
4. - Loop through all load cases while:
5. - Calculating the section strains & ply stresses
6. - Checking each ply for failure and calculate the reserve factors per ply
7. - Record the most critical stress & RF per section
8. Calculate wing deformations
9. Display the data output to the user in form of numerical data and graphs.

Only the steps in which calculations are performed will be elaborated upon, this include step 2,4,5,6,7 & 8. The section relating to the operation of the program are excluded for brevity. For more information look into the code and follow the comments.

9.3.2. Step 2: Calculate the section properties

For the calculation of the laminate properties the classical lamination theory (CLT) is used. The step iterates through the laminate and constructs the required ABD matrices for the cruise and VTOL configuration. For a recap on the classical lamination theory refer Appendix D, or one of the many works on composites.

As the CLT only works for a laminate in a single plane, two ABD matrices must be calculated. One for the top and bottom skin, and one for the webs and the core. In the calculation of the ABD matrices for the facesheets and webs, the width of each element was taken into account such that instead of the load per unit length the load could directly be related to the laminate strains. In the calculation of the ABD matrix elements smaller than 10^{-5} are replaced by zero, to aid in the stability during the matrix inversion. After the determination of the ABD matrices, the inverse was taken to relate load to strains. In step 4, see section 9.3.3, the loads will be multiplied with the ABD matrix of the skin or web, corresponding to the loadcase that is being analysed.

However, the torsional stiffness for a wingbox is not adequately captured by this usage of the CLT due to the large enclosed area. Hence a modification was applied to incorporate the correct torsional stiffness. To analyse a composite box beam use is made of the article *"Analysis of thin-walled composite box beam under torsional load without external restraint"* by Wu et al [46, Eq.14-16]. The process is much alike for an isotropic box beam where the twist is derived as:

$$\phi = \frac{TL}{GK} \tag{9.10}$$

Where the torsional stiffness of the entire cross-section GK is defined as:

$$GK = \frac{\omega^2}{\oint \frac{ds}{G_r t_r}} = \frac{2b^2h^2}{\frac{b}{G_1 t_1} + \frac{h}{G_2 t_2}} \tag{9.11}$$

In which b, and h are the width and height of the beam respectively and Gt is the shear stiffness times the thickness of the top skin and web respectively. Gt is given by Wu as:

$$G_r t_r = \sum_{i=1}^{n} \left(\overline{Q}_{66}\right)_i t_i - (\alpha_{16})_r \sum_{i=1}^{m} \left(\overline{Q}_{11}\right)_i t_i \tag{9.12}$$

Where α_{16} accounts for the extension shear coupling. It can be observed that the rotated ply stiffness multiplied by the thickness of each ply corresponds to the A-matrix contribution for that ply found by CLT. Hence the equation can be rewritten as:

$$G_r t_r = \sum_{i=1}^{n} \left(A_{66_i} - \frac{A_{16_i}^2}{A_{11_i}} \right) = A_{66} - \frac{A_{16}^2}{A_{11}} \tag{9.13}$$

As the ABD matrices of the skin and web laminates are separated, each ABD matrix will need to incorporate the correct amount of torsional stiffness for each element such that the total stiffness is correct. For a thin walled hollow beam the shear flow is constant. The foam core is neglected due to the low shear stiffness it provides. The torsion is related to the shear flow by $T = 2Aq$. It can be observed that the skin and web, contribute equally to the torsional stiffness as the the moment arm multiplied by the element length is equal to the width multiplied by the height. However the ABD matrix relates the torsional load to the curvature κ_{xy}. If the skins get wider the total contribution of the skins to the torsional stiffness remains $A \cdot q$. But as the loads are inserted as direct load and not as running loads, the D_{66} terms in the ABD matrices need to be adapted according to:

$$D_{66_{skin}} = \frac{T \cdot GK}{W} \tag{9.14}$$

$$D_{66_{web}} = \frac{(1-T)GK}{1-W} \tag{9.15}$$

Where T is the thickness ratio of the web and skin:

$$T = \frac{t_{skin}}{t_{skin} + t_{web}} \tag{9.16}$$

And W is the width ratio of the skin:

$$W = \frac{b}{b+h} \tag{9.17}$$

Unfortunately this method also has a drawback as the curvature κ_{xy} will not be equal for the webs and the skins. This has to be taken into account when calculating the twist angle, see section 9.3.7.

Buckling As the cross-sections have equal properties in this method, also the stress and strain at which buckling will occur in a laminate are constant. As the wing has a full foam core the buckling analysis must take the support of the foam into account. The foam significantly increases the out of plane stiffness and support of the laminate. To estimate the buckling of composite beam with a full foam core wrinkling methods for sandwich structures will be used.

Many researches have worked on the modelling of wrinkling in sandwich structures over the years. A good overview can be found in a NASA sponsored report by Northrup Grumman [37] and in Carlon and Kardomateas [28, Ch. 8]. Few sources mention the applicability of the wrinkling equation in bending problems where only one facesheet is in compression. One of the most used methods is the method of Hoff & Mautner. The critical stress for symmetric wrinkling in sandwiches, when the affected zone is less than half the core thickness (thick cores), is given as:

$$\sigma_{cr} = 0.91\sqrt[3]{E_f E_c G_{xy}} \tag{9.18}$$

Where E_c & G_{xy} are core properties and E_f is the facesheet stiffness:

$$E_f = \frac{12\left(1-\nu_{xy}\nu_{yx}\right)D_{11_f}}{t_f^3} \tag{9.19}$$

Different methods come to the same formula albeit with a different factor.

In section 10.2 of the next chapter the Python tool is validated against an ultimate load test. As the prediction is 13 percent higher than the tested failure load, a correction to the wrinkling coefficient is made by reducing it by 11.5 % from 0.91 to 0.81 as detailed in section 10.3.

9.3.3. Step 4: Loads

The fourth step is to run through all the load cases as obtained by the sizing Excel sheet. Two groups can be identified, the loads in the cruise reference frame, and the loads in the VTOL reference frame. In the cruise reference frame the following load cases are used:

- +4.5 G
- -2.5 G
- Transition
- Inertial loads at 4.5G
- Inertial loads at -2.5G
- Upwards elevon deflection
- Downwards elevon deflection
- Unsymmetrical wing loading 70%-100%
- Unsymmetrical wing loading 100%-70%

And the folowing in the VTOL reference frame:

- Hover flight
- Landing impact on both canard gear
- Landing impact on single canard gear
- One-engine-off conditions

These loads cases are described in chapter 8.

Two load vectors are defined for the loads that will be taken up by the skin and web laminates.

$$\begin{aligned} \text{Skin loads} &= [0, 0, F_{\text{X}}, M_{\text{cruise}}, 0, T] \\ \text{Web loads} &= [0, 0, F_{\text{Z}}, M_{\text{VTOL}}, 0, T] \end{aligned}$$

As can be seen the skin will take up the shear loads in Z-direction (VTOL) and the bending moment during cruise configuration while the web laminates will take up de shear loads during cruise flight and the bending loads in the VTOL configuration. Both the skin and web will be loaded due to torsion.

9.3.4. Step 5: Section strains & ply stresses

With the loads of the previous steps, the section strains are calculated in the following way:

$$\begin{bmatrix} \epsilon \\ \kappa \end{bmatrix}_{\text{Skin}} = \begin{bmatrix} A & B \\ C & D \end{bmatrix}^{-1}_{\text{Skin}} [0, 0, F_{\text{X}}, M_{\text{cruise}}, 0, T]^T \tag{9.20}$$

$$\begin{bmatrix} \epsilon \\ \kappa \end{bmatrix}_{\text{Web}} = \begin{bmatrix} A & B \\ C & D \end{bmatrix}^{-1}_{\text{Web}} [0, 0, F_{\text{Z}}, M_{\text{VTOL}}, 0, T]^T \tag{9.21}$$

Now that the section strains are known, the strains in the individual plies can be calculated.

$$\begin{bmatrix} \epsilon_x \\ \epsilon_y \\ \gamma_{xy} \end{bmatrix}_{\text{ply}} = \begin{bmatrix} \epsilon_x \\ \epsilon_y \\ \gamma_{xy} \end{bmatrix}_0 + Z \begin{bmatrix} \kappa_x \\ \kappa_y \\ \kappa_{xy} \end{bmatrix}_0 \tag{9.22}$$

Where the ply strains are evaluated at the top, bottom and middle of the ply. This is important as the top or bottom of the ply will see larger stresses due to bending. As the strains are now known in the x and y reference frame, the plies must be rotated into their local material axis. This will be performed by:

$$\begin{bmatrix} \epsilon_1 \\ \epsilon_2 \\ \gamma_{12} \end{bmatrix} = \begin{bmatrix} m^2 & n^2 & nm \\ n^2 & m^2 & -nm \\ -2nm & 2nm & m^2 - n^2 \end{bmatrix} \begin{bmatrix} \epsilon_x \\ \epsilon_y \\ \gamma_{xy} \end{bmatrix} \tag{9.23}$$

Where n = sin(θ) and m = cos(θ). The last step is transform the ply strains into ply stresses which is done by multiplying the ply strain in the material axis with the ply stiffness matrix.

$$\begin{bmatrix} \sigma_1 \\ \sigma_2 \\ \tau_{12} \end{bmatrix}_{\text{ply}} = Q_{\text{ply}} \begin{bmatrix} \epsilon_1 \\ \epsilon_2 \\ \gamma_{12} \end{bmatrix}_{\text{ply}} \tag{9.24}$$

The core is treated as any other layer but with different material properties.

At the end of this step the stresses and strains for all the plies, load cases, and sections are stored in global arrays.

9.3.5. Step 6: Check for failure & reserve factors

After the strains and stresses are calculated in the plies the reserve factors and failure criteria can be calculated. The failure type and the reserve factor are calculated in the RF function according to the failure criteria used as described in section 9.1.5. After the individual plies are checked for failure, the highest compressive strains for each skin and web are calculated. If these strains exceed the critical strain from section 9.3.2 buckling does occur, this is stored to be reported to the user, and the reserve factor is changed to the value:

$$RF_{\text{buckling}} = \frac{\text{Critical buckling strain}}{\text{Negative ply strain}} \tag{9.25}$$

When a reserve factor is lower than unity, the type of failure will be stored and reported to the user. The types of failure that can be reported are:

- Top skin buckling
- Bottom skin buckling
- Front web buckling
- Aft web buckling
- Fibre failure
- Matrix failure

9.3.6. Step 7: Record most critical stress & RF

With the all the reserve factors determined, the lowest reserve factor per ply per location and load case can be determined. This is performed by simply taking the minimum of the 3 dimensional GlobalRF array with respect to each load case and each section.

9.3.7. Step 8: Wing deformations

The next step is to calculate the wing deformations. The deflections of the beam are calculated by using the obtained curvature at different sections of the beam. The curvature of a section is assumed to be constant and is equal to the average of the local radii of curvature at the calculation points. The radius of curvature is related to the angle between two sections, with respect to its focal point, by the arc length of the section (L_0):

$$\theta = \frac{L_0}{R} = \bar{\kappa} L_0 \tag{9.26}$$

For each load case all the cross-sections will be run through. First the beam curvatures are calculated by:

$$\theta_{x_i} = \theta_{x_{i-1}} + L_0 \frac{\kappa_{x_i} + \kappa_{x_{i-1}}}{2} \tag{9.27}$$

$$\theta_{z_i} = \theta_{z_{i-1}} + L_0 \frac{\kappa_{z_i} + \kappa_{z_{i-1}}}{2} \tag{9.28}$$

Where L_0 is the non deformed distance between each section, $Y_i - Y_{i-1}$. The deformed shape of the wing is calculated by

$$X_i = X_{i-1} + L_0 \sin\left(\frac{\theta_{x_i} + \theta_{x_{i-1}}}{2}\right) \tag{9.29}$$

$$Z_i = X_{i-1} + L_0 \sin\left(\frac{\theta_{x_i} + \theta_{x_{i-1}}}{2}\right) \tag{9.30}$$

The beam shortening, in the Y-direction, is calculated depending on the load case configuration. For cruise load cases:

$$Y_i = Y_{i-1} + L_0 \cos\left(\frac{\theta_{x_i} + \theta_{x_{i-1}}}{2}\right) \tag{9.31}$$

And for VTOL load cases:

$$Y_i = Y_{i-1} + L_0 \cos\left(\frac{\theta_{z_i} + \theta_{z_{i-1}}}{2}\right) \tag{9.32}$$

For calculating the wing twist, it has to be taken into account that the ABD matrix was modified to account for using the direct loads. The coefficient T/W used also has an effect on the twisting curvature, κ_{xy}. Hence the coefficient W/T is required to calculate the correct torsion angle of each section. The twisting moment of curvature can be related to the method of Wu by observing that:

$$\frac{M_{xy} L}{d_{66}} = \kappa_{xy} L \quad = \quad \phi = \frac{TL}{G_k} \tag{9.33}$$

Taking the modification of equation 9.14 into account results requires:

$$\phi = \kappa_{xy_{skin}} L_0 \frac{W}{T} \tag{9.34}$$

The modification to equation 9.15 taken into account results in:

$$\phi = \kappa_{xy_{web}} L_0 \frac{1-W}{1-T} \tag{9.35}$$

Which results in the same angle as equation 9.34.

As common for numerical methods, when increasing the number of sections the representation of the curvature and deflections become more accurate.

9.3.8. Step 9: Data output

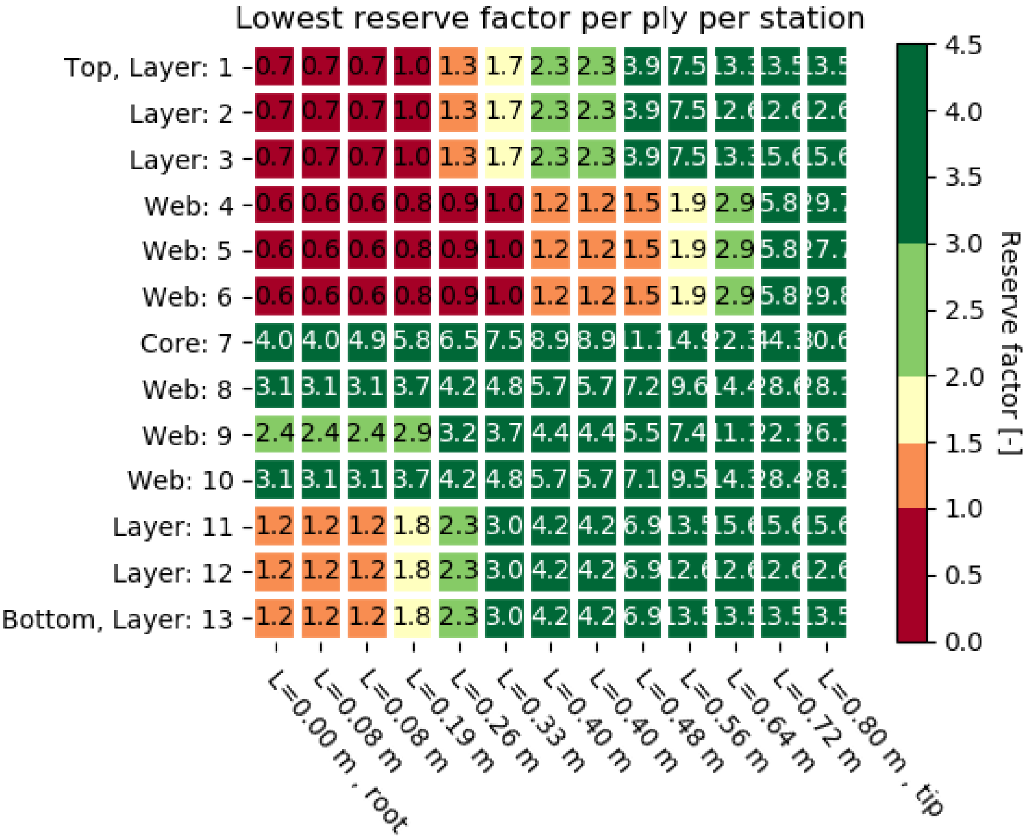

	L=0.00 m , root	L=0.08 m	L=0.08 m	L=0.19 m	L=0.26 m	L=0.33 m	L=0.40 m	L=0.40 m	L=0.48 m	L=0.56 m	L=0.64 m	L=0.72 m	L=0.80 m , tip
Top, Layer: 1	0.7	0.7	0.7	1.0	1.3	1.7	2.3	2.3	3.9	7.5	13.3	13.5	13.5
Layer: 2	0.7	0.7	0.7	1.0	1.3	1.7	2.3	2.3	3.9	7.5	12.6	12.6	12.6
Layer: 3	0.7	0.7	0.7	1.0	1.3	1.7	2.3	2.3	3.9	7.5	13.3	15.6	15.6
Web: 4	0.6	0.6	0.6	0.8	0.9	1.0	1.2	1.2	1.5	1.9	2.9	5.8	29.7
Web: 5	0.6	0.6	0.6	0.8	0.9	1.0	1.2	1.2	1.5	1.9	2.9	5.8	27.7
Web: 6	0.6	0.6	0.6	0.8	0.9	1.0	1.2	1.2	1.5	1.9	2.9	5.8	29.8
Core: 7	4.0	4.0	4.9	5.8	6.5	7.5	8.9	8.9	11.1	14.9	22.3	44.3	30.6
Web: 8	3.1	3.1	3.1	3.7	4.2	4.8	5.7	5.7	7.2	9.6	14.4	28.6	28.1
Web: 9	2.4	2.4	2.4	2.9	3.2	3.7	4.4	4.4	5.5	7.4	11.1	22.1	26.1
Web: 10	3.1	3.1	3.1	3.7	4.2	4.8	5.7	5.7	7.1	9.5	14.3	28.4	28.1
Layer: 11	1.2	1.2	1.2	1.8	2.3	3.0	4.2	4.2	6.9	13.5	15.6	15.6	15.6
Layer: 12	1.2	1.2	1.2	1.8	2.3	3.0	4.2	4.2	6.9	12.6	12.6	12.6	12.6
Bottom, Layer: 13	1.2	1.2	1.2	1.8	2.3	3.0	4.2	4.2	6.9	13.5	13.5	13.5	13.5

Figure 9.3: Graphical output of the code for layup 10. The reserve factor per ply per location is shown. Red indicates that a failure has occurred. In this case buckling occurs on the top skin and front web.

The last step is to return the generated data to the user. The program returns various data to the IPython console, such as the tip deflection, tip slope, beam twist, maximum beam stresses, maximum shear stresses for all load cases. Furthermore the lowest RF for all load cases is displayed and the failure type is returned to the user if any occurred. Furthermore seven plots are generated. Figure 9.4 graphically displays the lowest reserve factor per load case per location. This can be used to see where in the structure there is still margin left to reduce material. The second graph graphically shows the reserve factor for each ply and each section, see figure 9.3. Red shows failed layers. This can be used to see which part of the structure is expected to fail. The other five plots show the deflected beam, the local slope and the local twist angle for all load cases.

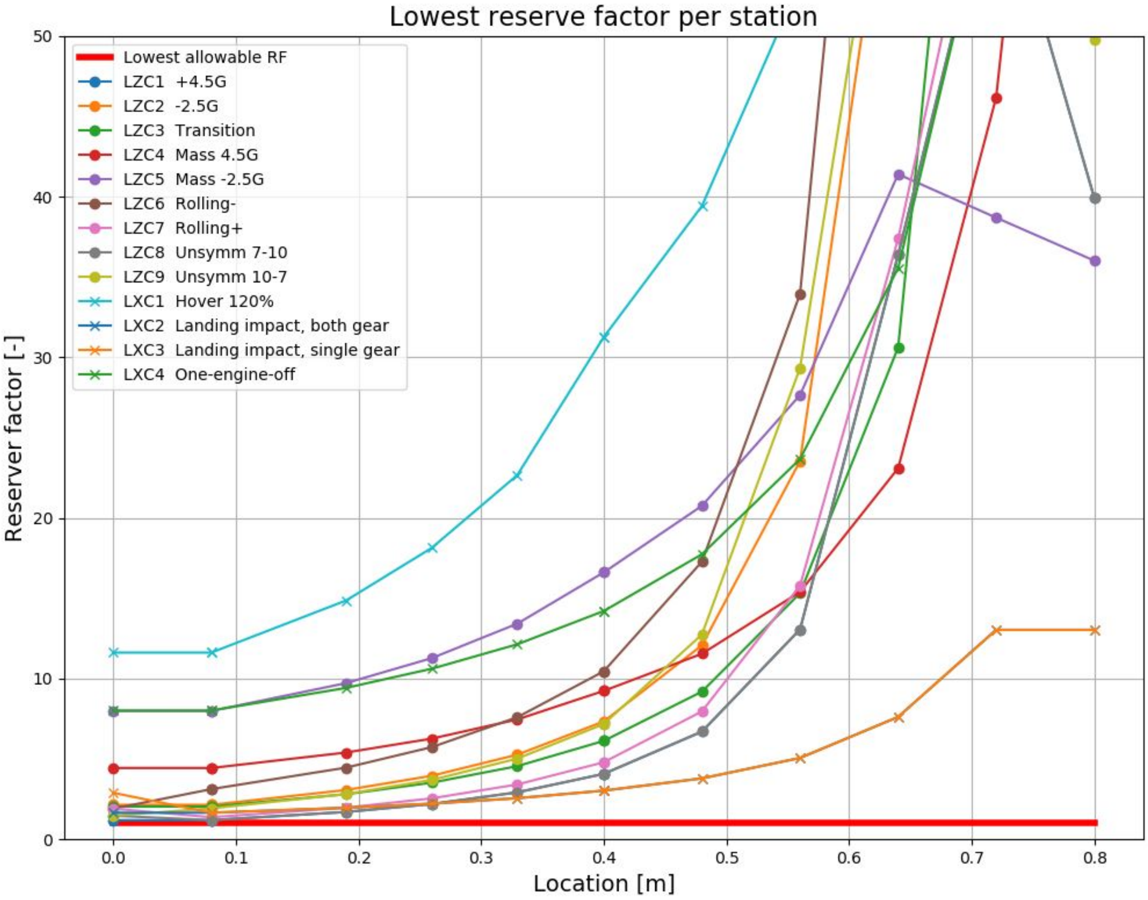

Figure 9.4: Lowest reserve factor per station for layup 7. Carbon fibre + PET core.

9.4. Structure

With the loads of the previous chapter and the Python tool described in section 9.3 the structure can be analysed and optimized. Various layups of various materials have been analysed, in table 9.2 the properties of each section can be seen. The table gives the layup used, which is detailed in table 9.3, the core material, the most inward location on the canard were this layup will not fail. Using the layup on a location closer to the root results in a reserve factor smaller than unity. Furthermore the used safety factor and the corresponding reserve factor for the location given, the most critical failure mode, an estimation of the mass per meter and the last column indicates if the cut-out in the canard has been taken into account in the analysis. For each analysis a graphical overview is generated which shows at which location and at which ply failure is expected and what reserve factor can be expected, see figure 9.3.

Table 9.2: Data of analysed layups, see table 9.3 for the specific layup.

Layup [−]	Core [−]	Location [m]	SF [−]	RF [−]	Most critical failure mode [−]	Mass/m [kg/m]	Location [−]
1	XPS	0	3.6	1.05	Front web buckling	1.38	Cutout
2	LBX	0	3.6	1.30	Front web buckling	1.43	Cutout
3	RTMX	0	3.6	1.51	Front web buckling	1.48	Cutout
4	RTMX	0	3.6	1.05	Front web buckling	1.05	Cutout
5	PET	0	3.6	1.71	Web Matrix failure	1.21	Cutout
6	PET	0	3.6	1.08	Front web buckling	0.86	Cutout
7	PET	0	3.6	1.41	Top skin buckling	0.64	Cutout
8	PET	0.08	3.6	1.40	Top skin buckling	0.81	main
9	XPS	0.19	3.6	1.04	Front web buckling	1.01	main
10	XPS	0.40	3.6	1.17	Front web buckling	0.82	main
11	PET	0	3.6	2.05	Front web buckling	1.23	main
12	XPS	0.48	3.6	1.10	Front web buckling	0.59	main
13	XPS	0.19	3.6	1.09	Front web buckling	1.09	main
14	XPS	0.40	3.6	1.16	Front web buckling	0.87	main
15	XPS	0	3.6	1.55	Top skin buckling	1.64	main
16	XPS	0	1.5	1.43	Front web buckling	0.81	main
17	XPS	0.08	1.5	0.99	Front web buckling	0.69	Cutout
18	XPS	0	1.5	1.23	Front web buckling	0.82	Cutout
19	XPS	0	1.5	2.27	Front web buckling	1.14	main
20	PET	0	1.5	3.30	Tensile failure	1.22	main
21	PET	0	1.5	1.78	Tensile failure	0.85	Cutout
22	XPS	0.40	3.6	1.03	Top skin buckling	0.41	main
23	XPS	0.56	3.6	1.04	Front web buckling	0.59	main

With these layups combinations were made such that plies can be dropped towards the wing tip. Table 9.4 indicated the different stackings that were found to be of interest. Each row in the table correspond to a stacking were the numbers indicate which layup from table 9.3 can be used at which location of the canard. Multiple interesting findings were made. Firstly, the XPS foam core in combination with the fibreglass reinforcements showed poor performance against bucking. Especially the buckling of the front spar due to single gear landing impact. A stacking with 6 plies on each skin and 11 on the webs would be required to prevent buckling. The weight of each stacking was analysed for the box beam, see table 9.5. The stacking "Easiest glass XPS" is the aforementioned stacking with a very high amount of plies which results in a very high wing estimated wing weight of 2.37 kilograms.

Table 9.3: Analysed layups. Unless otherwise specified; (x) is Interglass 92110 BID ply, x is Interglass 92145 UND ply, $_s$ means symmetry and $_2$ means 2 consecutive layers.

Layup	Skin	Web
1	$[(45),0,(45)]_s$	$[(45),0_2,45,0,(0),0,-45,0_2,(45)]$
2	$[(45),0,(45)]_s$	$[(45),0_2,45,0,(0),0,-45,0_2,(45)]$
3	$[(45),0,(45)]_s$	$[(45),0_2,45,0,(0),0,-45,0_2,(45)]$
4	[(45),0,(0),0,(45)]	[(45),0,45,-45,0,(45)]
5	[(45),0,(0),0,(45)]	[(45),0,45,-45,0,(45)]
6	[(45),0,(0)]	[(45),0,(45)]
7	$[(15),(-15)]_{carbon}$	$[(45)]_{carbon}$
8	$[(-15)]_{carbon}$	$[(45)]_{carbon}$
9	$[(45),0_2,(0)]$	[(45),0,(45)]
10	[(45),0,(0)]	[(45),0,(45)]
11	[(45),0,(0)]	[(45),0,(45)]
12	[(45),(0)]	[(45),(45)]
13	$[(45),0]_s$	[(45),0,(0),0,(45)]
14	[(45),0,(45)]	[(45),0,0,(45)]
15	$[(45),0,(45)]_s$	$[(45),0_2,45,0,(0),0,-45,0_2,(45)]$
16	Alu t = 0.4 mm	Alu t= 0.4 mm
17	Alu t = 0.508 mm	Alu t= 0.508 mm
18	Alu t = 0.635 mm	Alu t = 0.635 mm
19	Alu t = 0.635 mm	Alu t = 0.635 mm
20	Alu t = 0.4 mm + PET	Alu t = 0.4 mm + PET
21	Alu t = 0.4 mm + PET	Alu t = 0.4 mm + PET
22	$[(-15)]_{carbon}$	$[(45)]_{carbon}$
23	[(45),(45)]	[(45),(45)]

Interestingly the wing weight in the cut-out area can be drastically reduced by using a stiffer and heavier foam. This heavier foam increases the critical buckling strain considerably such that only 3 plies on the skin and web are required by using a PET foam core. The Airex T92.60 PET foam core is with 65 kg/m^3 more than twice as heavy than the 30 kg/m^3 XPS foam, but it results in a mass per meter of 0.86 kg/m compared to 1.38 kg/m for the PET and XPS foam respectively.

Moving out further to the tip results is a lot lower loads and that is were the low density XPS foam outperforms the PET foam. The lightest glass wing (" *"Glass,PET,XPS"* in table 9.5 is 1.30 kilograms, this requires a PET core up to y = 400 mm, and an XPS core on the tips. At y = 480 mm the unidirectional plies can be dropped, leaving only two plies at tip. By not using the PET core, the *"Glass+XPS"* canard is 0.15 kilograms heavier.

However two other interesting configurations were found. When generic carbon weave data from the book of Kassapoglou [26] (X = Y = 1379 MPa, S = 119 MPa, E = 69 GPa, G = 5 GPa, ν_{xy} = 0.05 & t_{ply} = 0.191 mm) is used an even lighter wing can be designed. The *"Carbon,PET,XPS"* stacking only requires 2 layers on the skin and one on the web. Resulting in a wing weight of only 0.87 kilograms which is a reduction of 63 percent compared to the initial glass wing. It must be noted however that the 0.38 mm thick skin an 0.19 mm web are prone damage by just handling it uncarefully. As this load case is not analysed it should be investigated further if used.

The other interesting configuration is a bit heavier than the carbon wing, but still lighter than the lightest glass wing. By using 2024T3 aluminium over and XPS core a light wing can be built. For the *"Alu stepped"* configuration two thicknesses are used: 0.40 mm and 0.635 mm which result in a wing

Table 9.4: Potential canard ply stacking. Each row indicates which specific layup from table 9.3 will be used at which location.

Location [m]	0	0.080	0.081	0.19	0.26	0.33	0.40	0.401	0.48	0.56	0.61	0.68	0.75	0.754
Carbon	7	7	7	8	8	8	8	8	8	8	8	8	8	8
Easiest glass XPS	1	1	1	15	15	15	15	15	15	15	15	15	15	15
Carbon, PET,XPS	7	7	7	8	8	8	8	22	22	22	22	22	22	22
Glass,PET,XPS	6	6	6	11	11	11	10	10	12	12	12	12	12	12
Glass + XPS	1	1	1	13	13	13	13	14	12	12	12	12	12	12
Alu single skin	18	18	18	19	19	19	19	19	19	19	19	19	19	19
Alu stepped	18	18	18	16	16	16	16	16	16	16	16	16	16	16
Alu + PET	21	21	21	20	20	20	20	20	20	20	20	20	20	20
Alu + PET + XPS	21	21	21	16	16	16	16	16	16	16	16	16	16	16

Table 9.5: Estimated canard weight for the different ply stackings from table 9.4 for the box beam.

Ply stacking [−]	Canard weight [kg]	Difference [%]
Carbon,PET	1.16	-51.3
Easiest glass XPS	2.37	0.0
Carbon, PET,XPS	0.87	-63.3
Glass,PET,XPS	1.30	-45.4
Glass + XPS	1.45	-39.1
Alu single skin,XPS	1.60	-32.6
Alu stepped,XPS	1.23	-48.2
Alu + PET	1.70	-28.6
Alu + PET + XPS	1.24	-47.8

weight of only 1.23 kilograms. This step however makes this concept unfeasible as the loads in the skin can only be transferred if a strap is used to join the two skins together. The single thickness *"Alu+PET+XPS"* configuration with a 0.635 mm 2024T3 skin is only slightly heavier with 1.24 kilograms but is lighter than the glass wing (1.30 kg) and is easier to manufacture. The 0.635 mm thick sheet can be easily bend and glued to the foam core, this reduces the need for fasteners which are heavy, induce stress concentrations and take time during manufacturing.

9.4.1. Proposed structural design

The different materials and ply stackings investigated in this chapter showed interesting features for the drone structure. Next to weight, also manufacturability, damage tolerance and cost play a role. Performance wise it was clear that making use of a stiffer core material at the root reduces the amount of plies required and hence the weight. The heavy PET core must be traded in for a light weight core at the tips to reduce weight. Taking into account the different requirements the following is a list of options available for the drone structure in order of preference.

1. *"Alu, PET, XPS"* 1.24 kg, light and simple structure with a 0.40 mm thick skin. Fast to manufacture with adequate tooling. Better resistant against damage. The most critical failure mode is tensile failure of the web.
2. *"Glass, PET, XPS"* 1.30 kg, light, slightly more complicated manufacturing, with a maximum skin thickness of 0.67 mm at the root and 0.39 mm at the tip. The most critical failure mode is front web buckling.
3. *"Carbon, PET, XPS"* 0.87 kg, very light, prone to handling damage with a maximum skin thickness of 0.38 mm. The most critical failure mode is top skin buckling.
4. *"Glass, XPS"* 1.45 kg , material is cheap and easy to come by. Not the lightest solution, due to

the thick layup at the root (skin = 1.33 mm & web = 2.77 mm). The most critical failure mode is front web buckling.

Both the manufacturing- and material- costs are an important aspects of the trade-off as the latter was not part of the thesis no qualitative trade-off could be made.

10

Verification & validation

This chapter presents the verification & validation of the Python program from chapter 9. In section 10.1 the generation of the correct ABD matrices is verified with literature and the code is verified with analytical beam equations. Section 10.2 describes the prediction and results of the ultimate load test that was performed on a simplified test wing to provide validation. Section 10.3 reflects on the verification and validation.

10.1. Verification

This section deals with the steps taken to verify the Python code. Two verification steps have been performed, firstly a verification of the calculation of the ABD matrices have been performed, showed in section 10.1.1, to make sure that all properties of the composites are calculated correctly. Secondly, in section 10.1.2, the results of the code are compared to analytical cantilevered beam equations to verify the code for use with an isotropic material under various loading conditions such as a tip moment, a tip load, a distributed shear load, a torsional load and a combined load case.

10.1.1. Code verification of ABD calculations

The Python function used to calculate the ABD matrices was verified with the various layups and corresponding A & D matrix terms given in Kassapoglou [26]. The reference layups and data can be found on pages: 127, 161, 165, 215, 227, 277, 356, 364, 374. The input data and results for the example on page 165B and page 215 are given in table 10.1 & 10.2. The largest error of 1.9 % was found on relative small numbers of the A_{66} & D_{66} terms for the example of page 165, layup B. The error can be attributed due to the round off error as the input data had only one significant digit. For the example of page 215 the maximum error was below 0.1%.

Table 10.1: Material input data used from Kassapoglou [26] for ABD verification in table 10.2.

Input	Page 165 B	Page 215	Units
E_x	69	137.9	[GPa]
E_y	69	11.0	[GPa]
ν_{xy}	0.05	4.83	[-]
G_{xy}	5.1	0.29	[GPa]
t_{ply}	0.19	0.15	[mm]
Layup	$[(0/90)/(\pm 45)/\overline{(0/90)}]_s$	$[45/-45/0_2/\overline{90}]_s$	[deg]

Table 10.2: Comparison of A & D matrix terms. The example of page 165, layup B show the largest error of -1.9% due to single digit significance in the input data from table 10.1.

	Page 165B		Error	Page 215		Error	Units
	Kassapoglou	Boerma	[%]	Kassapoglou	Boerma	[%]	
A_{11}	55265	55167	-0.18	113015	113088	0.06	[N/mm]
A_{12}	13822	13833	0.09	23328	23327	0.00	[N/mm]
A_{22}	55265	55166	-0.18	54670	54678	0.01	[N/mm]
A_{66}	15453	15167	-1.89	25533	25547	0.06	[N/mm]
D_{11}	4560	4530	-0.67	12893	12905	0.09	[N mm]
D_{12}	663	660	-0.47	6220	6221	0.02	[N mm]
D_{22}	4560	4530	-0.67	8265	8269	0.05	[N mm]
D_{66}	786	777	-1.15	6564	6569	0.07	[N mm]

10.1.2. Analytical beam analysis

Analytical beam equations for a cantilevered constant cross-section beam were used to verify the correct working of the Python code. The material used in the analysis was 2024T3 aluminium. The material and beam properties are given in table 10.3.

Table 10.3: Model and material data used for verification by using analytical beam equations for an applied moment, shear, distributed load and torsion.

Property	Symbol	Value	Unit
Material	-	Aluminium 2024T3	[-]
Stiffness	E	72.0	[GPa]
Shear stiffness	G	27.0	[GPa]
Poisson's ratio	ν	0.33	[-]
Beam properties			
Skin & web thickness	t	0.40	[mm]
Width	b	135.8	[mm]
Height	h	43.8	[mm]
Length	L	670	[mm]

The analytical beam equations for the tip displacement and slope can be obtained by using the elastic curvature relation for beams. Beams where dv/dx is assumed to be small and with a constant bending stiffness follow the relation:

$$\frac{M}{EI} = \frac{d^2 v}{dx^2} \tag{10.1}$$

Any of the works on 'Mechanics of Materials', for example [21], can be used to obtain or lookup the tip deflection and slope equations. As this derivation is not of interest of this thesis the final equations are given:

Table 10.4: Analytical solutions for cantilevered under different loadings

Loading	Tip slope	Tip deflection	Twist
Tip moment	$\theta = \frac{ML}{EI}$	$\delta = \frac{ML^2}{2EI}$	0
Tip load	$\theta = \frac{PL^2}{2EI}$	$\delta = \frac{PL^3}{3EI}$	0
Distributed load	$\theta = \frac{qL^3}{6EI}$	$\delta = \frac{qL^4}{8EI}$	0
Torsion	0	0	$\phi = \frac{TL}{GK}$

Superposition can be used to obtain the deflection and slope due to combined load cases.

The maximum bending stress due to the loadings are obtained by using the general beam bending equation:

$$\sigma = \frac{M\overline{y}}{I} \tag{10.2}$$

Where $\overline{y}$ is the distance between the top of the beam and the neutral axis (h/2), and I is the inertia of the beam. The shear stress in the beam is calculated by obtaining the shear flow at the top and centre of the web. The shear stress can then be calculated by:

$$\tau = \frac{VQ}{It} \tag{10.3}$$

Where V is the shear load, and Q is the moment of area, Q = $\sum \overline{y}' A'$ at the top and centre of the web respectively. As the moment of area at the centre of the web is larger than at the top the maximum shear stress is located in the centre of the web, right at the neural line.

Five cases are investigated.

1. A 300 Nm bending moment applied at the wing tip.
2. A 500 N shear load applied at the tip.
3. A distributed load of 0.746 N/mm.
4. A 30 Nm torque applied at the tip.
5. A combined load case of all four forgoing loads.

The same loads are analysed in the Python tool by supplying the tool with a load file in which the local shear, bending moment and torque are given at 50 stations along the wing. The load cases were applied in both Z and X direction, representing the loads in cruise and in VTOL configuration respectively. The analytical and the numerical results can be seen in table 10.5 where the tip deflection, the tip slope, tip twist angle, maximum bending stress, maximum shear stress and average shear stress are given for the different loading conditions.

It can be observed that most conditions correspond very well with an error of less then 1 %. Two points stand out, the distributed load case shows larger errors for the deflection, slope and stresses. This can be attributed to the finite amount of cross-sections analysed. By using more cross-section the error can be decreased. Another point of attention is the maximum shear stress in the web. The classical lamination theory used for the numerical calculation of the shear stress in the web averages the load over the entire web. Hence the maximum shear stress is not captured correctly with and underestimation of 6.6 %. The average shear stress is captured within 0.5% error. The method used seems therefore applicable but the user should keep in mind that the peak shear stress is un-conservative.

The results for the load in the VTOL configuration can be seen in table 10.6. The inertia of the beam is significantly larger in the X direction than in the Z direction, hence the absolute value of the stresses and displacements is smaller. The most notable differences are the much larger deviations of the shear stresses, up to an over prediction of 14% for the average shear stress and an under prediction of 21% of the peak shear stress in the web. The deflection and slope due to the tip load in the VTOL configuration are slightly under predicted.

Table 10.5: Model verification by using analytical beam equations for tip moment, shear, distributed load and torsion. Material 2024T3 Aluminium, 0.4 mm thick, rectangular tubular beam 135.8 mm wide and 43.8 mm high, length = 670 mm. Cruise configuration.

Load		Tip moment 300 [Nm]	Tip load 500 [N]	Distrib. load 0.746 [N/mm]	Tip torque 30 [Nm]	All loads combined	Unit [-]
Deflect.	Analytical	15.9	11.8	4.43	0.00	32.1	[mm]
	Model	15.9	11.8	4.56	0.00	32.3	[mm]
	Error	0.30	0.30	3.00	-	0.61	[%]
Slope	Analytical	2.71	1.51	0.50	0.00	4.73	[deg]
	Model	2.72	1.52	0.52	0.00	4.76	[deg]
	Error	0.30	0.32	3.43	-	0.64	[%]
Twist	Analytical	0.00	0.00	0.00	0.26	0.26	[deg]
	Model	0.00	0.00	0.00	0.27	0.27	[deg]
	Error	-	-	-	0.1	0.1	[%]
$\sigma_{x_{skin}}$	Analytical	113.4	126.7	63.33	0.00	304.7	[MPa]
	Model	113.8	127.1	64.8	0.0	305.6	[MPa]
	Error	0.31	0.31	2.31	-	0.31	[%]
$\tau_{xy_{web}}$ max	Analytical	0.00	14.8	14.8	6.23	35.9	[MPa]
	Model	0.00	13.8	13.8	6.30	33.9	[MPa]
	Error	-	-6.70	-6.70	1.06	-5.67	[%]
$\tau_{xy_{web}}$ average	Analytical	0.00	13.8	13.8	6.23	33.8	[MPa]
	Model	0.00	13.8	13.8	6.30	33.8	[MPa]
	Error	-	0.30	0.30	1.06	0.10	[%]

Table 10.6: Model verification by using analytical beam equations for tip moment, shear, distributed load and torsion. Same beam as in table 10.5, but with the loads rotated 90 degrees, this represents the VTOL load cases.

Load		Tip moment 300 [Nm]	Tip load 500 [N]	Distrib. load 0.746 [N/mm]	Tip torque 30 [Nm]	All loads combined	Unit [-]
Deflect.	Analytical	2.81	2.09	0.79	0.00	5.69	[mm]
	Model	2.83	2.07	0.79	0.00	5.69	[mm]
	Error	0.54	-1.00	0.48	-	-0.04	[%]
Slope	Analytical	0.49	0.27	0.09	0.00	0.8	[deg]
	Model	0.48	0.27	0.09	0.00	0.84	[deg]
	Error	0.61	-1.34	0.52	-	-0.15	[%]
Twist	Analytical	0.00	0.00	0.00	0.26	0.26	[deg]
	Model	0.00	0.00	0.00	0.27	0.27	[deg]
	Error	-	-	-	0.1	0.1	[%]
$\sigma_{x_{skin}}$	Analytical	61.64	68.83	34.41	0.00	165.6	[MPa]
	Model	61.95	69.18	35.28	0.00	166.4	[MPa]
	Error	0.51	0.51	2.52	-	0.51	[%]
$\tau_{xy_{web}}$ max	Analytical	0.00	5.75	5.75	6.23	17.7	[MPa]
	Model	0.00	4.56	4.56	6.30	15.4	[MPa]
	Error	-	-20.8	-20.8	1.06	-13.1	[%]
$\tau_{xy_{web}}$ average	Analytical	0.00	4.01	4.01	6.23	14.2	[MPa]
	Model	0.00	4.56	4.56	6.30	15.41	[MPa]
	Error	-	13.7	13.7	1.06	8.17	[%]

10.2. Validation

To validate the code a simple wing was built based on the canard. The wing is a based on the canard and has a full foam core, constant cross-section and constant layup along the entire span. The wing has a span of 1500mm and a nominal chord of 350 mm, but the wing was trimmed at a chordwise position of 250 mm, to account for the elevon. A closing spar was fitted to enclose the foam core. The following layup was used:

$$[(\pm 45), 0, 0, (\pm 45)]$$

Where the (± 45) plies are 163 g/m^2 Interglass 92110 bidirectional weaves and the 0 degree plies are 220 g/m^2 Interglass 92145 unidirectional weaves (with the majority of the fibres in 0 degree direction). The closing spar was made with a $[(\pm 45), 0, (\pm 45)]$ layup. The core was made from 30 kg/m^3 Soprema SL closed cell expanded polystyrene foam. The final wing weight of the test wing was 2.0 kg.

10.2.1. Prediction

As the Python code simplifies the wing cross-section as a foam filled box beam it is important to select the proper equivalent size of the box with respect to the airfoil. The choice was made to match the second moment of area of the box beam skin with the wing cross-section skin. The inertia of the wing cross-section was estimated by using the sketch tool of Solidworks. A box beam with equal thickness and equivalent inertia in the X- and Y- direction was obtained. The resulting width and height (233 x 53.1 mm) was used in the Python tool. See figure 10.1 for a size comparison between the equivalent box beam and the airfoil shape.

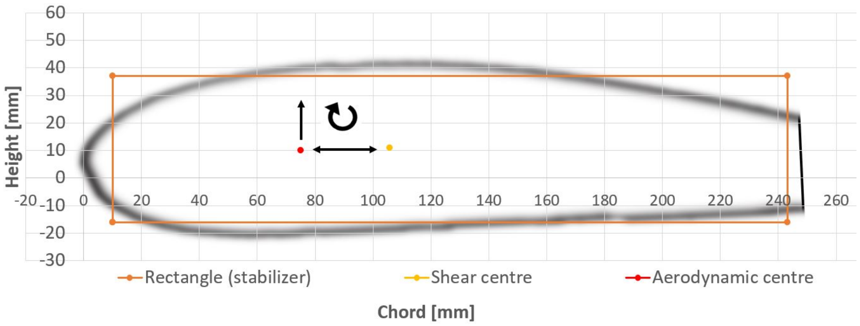

Figure 10.1: Idealized structure versus airfoil cross-section. Airfoil nominal chord = 350 mm, rectangle size: 233 by mm 53.1

The loads used for the static test article were calculated to the known failure load of the ultimate load test in the next section. The loads can be seen in figure 10.2. The wing was supported by a foam cradle shaped to the top side of the airfoil. In this supported area a linear decrease of the shear is assumed to satisfy equilibrium conditions. The shear load peaks at 2452 N at the start of the wing support and the bending moment peaks at 920 Nm at the wing root.

With the load known, and the layup inserted the program calculates the response of the test article. The tip deflection, tip slope, maximum beam stress, maximum shear stress and reserve factor are calculated. The values can be found in table 10.7. The reserve factors shows the capability of the beam to withstand the loads as inserted in the input file. If the reserve factor is larger than 1 in this validation case, the tool is over predicting strength. While a reserve factor lower than one would indicate a conservative or under predicted strength.

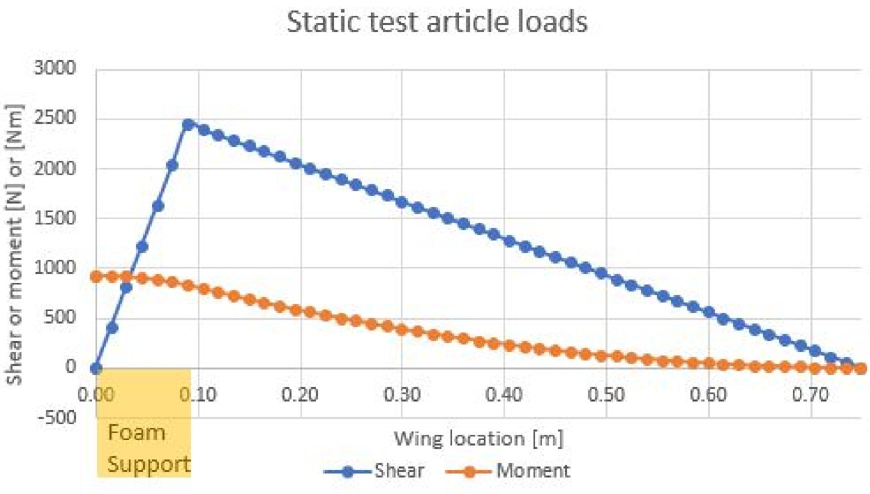

Figure 10.2: Shear and moment load in the static test article. Linear decrease in shear assumed at the supported area. Only one half of the test article is shown due to symmetry.

Table 10.7: Static test article validation results for the loads as in figure 10.2. Reserve factors are scaled to 1 for the ultimate load test.

Value	Predicted value	Tested value	Unit	Difference
Tip deflection	23.6	28.0	[mm]	-15.6 %
Tip slope	2.43	-	[deg]	-
Maximum beam stress	100	-	[MPa]	-
Maximum shear stress	14.5	-	[MPa]	-
Reserve factor w.r.t. tested value	1.13	1.00	[-]	13 %
Failure location	y = 0	y = 50	[mm]	-
Failure type	top skin buckling	top skin buckling	[-]	-

10.2.2. Ultimate load test

As the wing has no hard points a counter shape or cradle was required to hold the wing in place. With a hot-wire saw an XPS counter shape was cut which fitted exactly on top of the wing such that the wing could be placed upside down. The foam counter shape, which was 180 mm wide, was placed on two 15 cm thick wooden blocks resting on steel trestles. Tape was used to prevent the wing from sliding sideways during the test, but no further fixation was used. No strain gauges or other load sensors were used, due to the in-availability. The wing did not have finishing applied such that delaminations in the glass fibre composite could be easily spotted.

The wing was loaded symmetrically by means of adding sand bags of 25 kilogram each. On each side of the wing two sandbags could be placed side by side, with a distance of 225 and 485 mm to the centre of the wing respectively. This resulted in a maximum rectangular distributed load of 3.72 N/mm. After each bag was put in place, the tip displacement was measured. First the inner bag was put in placed, followed by the outer bag, after which the next row started on top of the inner sand bag. After each bag the tip displacement was measured by eye an a ruler with a millimetre scale.

After 10 bags were placed on each side of the wing, see figure 10.3, the wing failed catastrophically after four seconds. The failed wing can be seen in figures 10.4 to 10.6.

Three areas of damage were identified on the wing's top side, all extending from the leading to the trailing edge. It was observed that the two outer damages were secondary damages due to impact with the wooden support blocks. The centre damage (± 50 mm to the right of the wing centre) showed a clear case of top skin buckling which propagated towards the leading and trailing edge. The local buckle compressed the foam and buckled inwards, this decreased the local wing thickness after which the shear spar fractured under 45 degrees and the wing folded. No visual delaminations, or damage was visible on the bottom side of the wing.

Figure 10.3: Maximum loading on the static test article, just prior to failure

Figure 10.4: Failure of static test article

Figure 10.5: Damage on the static test article. Visible on the top side of the wing, flipped right side up. From left to right; Secondary failure - primary failure (buckling) - secondary failure.

Figure 10.6: Detailed picture of the primary failure mode: local buckling which caused collapse of the structure.

Before testing some manufacturing flaws were detected. Some dry fibres could be spotted in the unidirectional Interglass 92145 layers, but not at the location of the failure.

The deflections of the beam on both the left and right side can be seen in figure 10.7. Due to the failure of the wing the last deflection could not be measured. The value was estimated by observing an average increase of the tip deflection of 3.5 mm when the outer sand bag was loaded. Hence the final average wing deflection at the tip was estimated to be 28 millimeter.

10.2.3. Comparison between prediction and test

The test showed that the static test article wing was able to briefly sustain a load of 250 kg per wing side for a total wing weight of 2 kilograms. As can be observed in table 10.7, the Python tool over estimated the strength of the wing by 13 percent. The failure mode, top skin buckling or wrinkling was correctly predicted. The wing deflection at the tip was under estimated by 15.6 percent.

The location of the failure was predicted to be at the symmetry plane of the wing. However the test showed the location of the primary failure to be around 50 mm. This can be attributed to the fact that the location of the failure is not loaded in pure bending. The shear applied to the wing needs

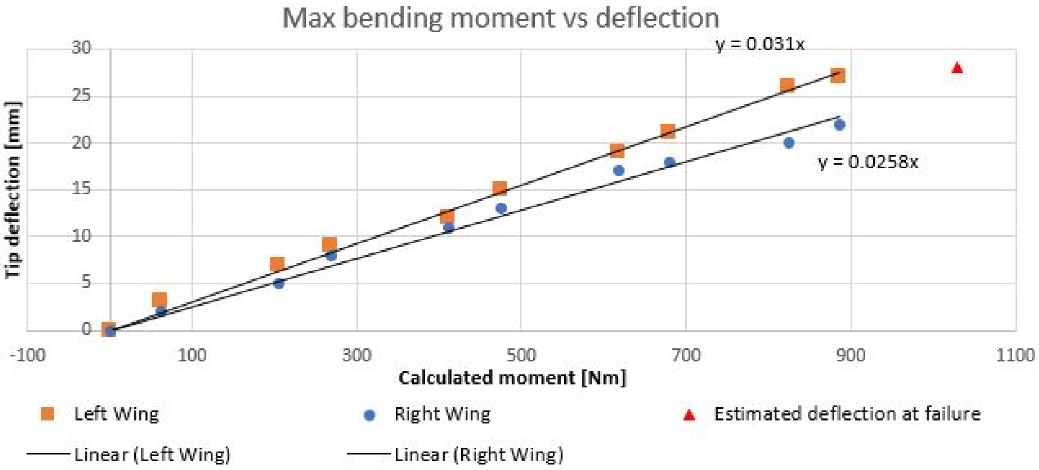

Figure 10.7: Tip deflections versus bending moment of the static test article.

to be transferred to the foam wing support in order to satisfy equilibrium. If it assumed that the shear is distributed equally over the foam support, the shear decreases linearly as given in figure 10.2. However it is likely that the shear load is higher toward the edge of the support.

Hence a large out of plane shear acts through the thickness of the wing near the location where the wing support stops (y = 90 mm). In this location both bending and shear loads are present on the cross-section. The Hoff-Mautner wrinkling estimation used does not take the shear loading into account. The out of plane shear loading causes the skin to buckle at a 11.5 percent lower load then predicted.

Another cause of the discrepancy between the prediction and test can be attributed to the uncertainty of the specific foam properties. The foam properties of the specific foam of the used supplier was unknown and hence the values have been used from a different supplier which delivers the same density of XPS foam. As long as no material properties are known, no estimate on the error value can be given. However it is assumed that the effect of the support plays a larger role in the deviation.

10.3. Reflecting on the verification and validation data

The verification showed good correspondence between the reference and calculated ABD matrices. The comparison between the program and analytical beam analysis showed a good correspondence except for the estimation of the maximum shear stress. This was because the Python program only calculates the average shear stress for the web members, as the shear stress is not constant but slightly parabolic the maximum shear stress in under predicted.

The assumption that initial failure coincides with final failure, see section 9.1.4, seems to be valid.

Validation by an ultimate load test on the static test article showed poor correspondence. The predicted tip deflection was underestimated by 16 percent. The failure mode was predicted correctly as buckling, however the failure occurred at a 11.5 percent lower load then predicted. The discrepancy can be partially attributed to the incorrect assumption of the stress state at the support which is not assumed in the buckling equation.

The effect of the out of plane load is not captured by the wrinkling estimation of Hoff and Mautner. A quick fix would be to reduce the coefficient in the Hoff and Mautner equation, see equation 9.18, to account for this effect. Reducing the 0.91 coefficient by 11.5 percent results in a new coefficient of 0.81. This values falls within the range of common wrinkling values, as the Cox and Riddell wrinkling estimation uses an coefficient of 0.76 [37]. As wrinkling tests historically have been shown to show a large variability, quite some spread is present on these coefficients. Further testing would be advisable to prove that the reduced coefficient does predict the failure load correctly.

The new corrected wrinkling equation to increase the correspondence between the prediction is therefore:

$$\sigma_{cr} = 0.81\sqrt[3]{E_f E_c G_{xy}} \tag{10.4}$$

11

Discussion

The results from this study present a detailed investigation into the structure, the loads of the tandem tiltwing prototype and the structural analysis of its canard. The loads cases are based on the JARUS certification specifications for unmanned aircraft systems. This provides the first step into proving that the structure that will be built is airworthy. In the process of the load estimation conservative estimations have been made to guarantee a safe structure. A specific feature of the vehicle improving structural safety is the inability of the aircraft to overstress its structure in the air below the never exceed speed. Only at the maximum dive speed can the maximum aerodynamic load be attained.

The most critical loads are the single side landing gear impact which drives the design for the canard attachment brackets, the maximum positive load case and the unsymmetrical load case. For the wing the maximum shear loads occur due to the transition load case. The latter is very unlikely as this requires the aircraft to fly with the wings perpendicular to the flow at stall speed.

The dynamics of the landing gear were not taken into account. Taking the angular acceleration of the vehicle into account, and/or performing a drop test will improve the accuracy of the result. And it will result in less conservative loads, as the current estimation is based on static equilibrium which is conservative.

The validation test performed on the static test article showed that the tool estimated the wing to be 13 % stronger than the test. The correct failure mode was predicted as top skin buckling. The Wrinkling estimation by Hoff and Mautner assumes a pure bending state, during the test also an out of plane shear was present which reduced the critical buckling strain. By altering the coefficient of the wrinkling estimation see equation 10.4 the estimation should be more accurate. This is however a crude method, to correct for the test. This does not necessarily mean that the estimation is now correct. It would be advisable to perform another test preferably without the out of plan shear load to improve the reliability of the tool.

When a test is performed with hardpoints installed on the shear spar at the cut-out, differences can be expected as well as the effect of stress concentrations is not captured. Hence it is advisable for the design of such hard points that more detailed analysis is used which take these effects into account.

The aluminium wing analysed in chapter 9, is worth investigating into more detail as the tool shows that a wing weight lower than the fibre glass is possible. This is partially due to lower required safety factor for the aluminium but also due to the higher material stiffness. Furthermore the manufacturing of the aluminium wing seems to be cheap and fast process compared to the composite solutions.

The safety factor used for the composites is high, hence that the aluminium structure is comparable to the glass fibre structure. If a lower safety factor can be agreed with the competent authority, lighter structures can be designed resulting in a better vehicle performance.

12

Conclusions

This chapter draws conclusions on the research into the development of a lightweight structure for a VTOL tandem tiltwing drone prototype.

- The moldless composite construction technique was found to be the most suitable construction technique for the prototyping phase of the project. This method entails that a foam core is hot wire cut into shape after which the facesheets are applied on the outside. The foam core fill the entire volume of the wing and provides support to the facesheet to prevent buckling. Due to the minimal tooling required the method is low in cost and changes to the sign can be quickly implemented when required.
- Tensile, compression and shear testing was performed on three types of fibreglass reinforcements impregnated with epoxy resin. With these results the materials could be characterised, which was used during the design of the wing.
- The sizing Excel sheet was modified to calculate the shear, bending moment and torsion diagrams for 9 cruise flight load cases and 4 VTOL load cases for both the wing and the canard. These loadcases are based on the CS-UAS and CS-LUAS certification specifications and provide a first step for certification.
- The loads during the transition flight, hover flight and cruise flight were analysed. The loads during the transition flight phases are low compared to maximum positive load factor and landing gear impact loads, which were the most critical load cases for the cruise and VTOL configuration respectively. The transition load cases are therefore not critical in the design.
- A tool was developed in Python to quickly (within one second) analyse the aforementioned load cases and estimate the strength of the composite canard. The Hashin-Rotem failure criterion was used for material failure and the Hoff & Mautner wrinkling condition was used to predict buckling.
- Verification of the tool showed good correspondence with analytical beam equations for a metallic box beam.
- Validation by means of an ultimate load test on a constant cross section sparless fibreglass wing with a span of 1500 mm was performed. The wing was able to sustain 500 kg of load spread equally on both sides of the support. The wing failed in top skin buckling, the failure mode was predicted correctly by the tool. However the tool over estimated the strength of the wing by 13 % and underestimated the wing tip deflection by 16%.

- With the tool 9 ply stackings for the canard were analysed. It was found that the lightest wings consisted of a 65 kg/m^2 Airex T92.60 PET foam core at the root and a XPS core at the wing tip. The carbon was found to be the face material resulting in the lightest wings (T_{max} = 0.38 mm). However the single layer facesheets are not recommended as damage due to handling is likely (T_{min} = 0.19 mm).
- The fibreglass and aluminium wings with PET and XPS foam did not differ much with respect weight witch each other; 1.24 and 1.30 kilograms for aluminium 2024T3 versus the fibreglass wing respectively. The aluminium facesheet can be the thinnest sheet commonly available with 0.40 mm thick, while the glass wing requires a skin thickness of 0.67 mm at the wing root.

Bibliography

[1] A. Chatterjee, J.W. Gillespie Jr. Room temperature-curable VARTM epoxy resins: Promising alternative to vinyl ester resins. *Applied Polymer science*, 115(2):665–673, 2010. DOI: 10.1002/app.30740.

[2] A. Crugnola, N. Schott & D. Rosato. Out-of-autoclave here to stay for high-quality composites. Published on website: `http://exclusive.multibriefs.com/content/out-of-autoclave-here-to-stay-for-high-quality-composites/engineering`. Retreived on 7/02/2019.

[3] I. H. Abbott and A. E. von Doenhoff. *Theory of Wing Sections: Including a Summary of Airfoil Data*. Dover Publications, Inc, 1959. ISBN 0-486-60586-8.

[4] ArmaCell. ArmaForm®Core. Published on website: `https://local.armacell.com/fileadmin/cms/pet-foams/TDS/ArmaForm_Core/Core_TDS_0076_201800806.pdf`, 2018. Product data sheet.

[5] ASTM International. Astm d6641 / d6641m-16e1, standard test method for compressive properties of polymer matrix composite materials using a combined loading compression (clc) test fixture, 2016. DOI: 10.1520/D6641_D6641M-16E01.

[6] ASTM International. Astm 3039m/d3039m-17, standard test method for tensile properties of polymer matrix composite materials, 2017. DOI: 10.1520/D3039_D3039M-17.

[7] ASTM International. Astm d3518 / d3518m-18, standard test method for in-plane shear response of polymer matrix composite materials by tensile test of a ±45° laminate, 2018. DOI: 10.1520/D3518_D3518M-18.

[8] D. Naik C. Ostowari. Post-Stall Wind Tunnel Data for NACA 44xx Series Airfoil Sections. Solar Energy Research Institute, January 1985. DOI: 10.2172/5791328.

[9] Flake Campbell. *Manufacturing Processes for Advanced Composites.* , October 2018.

[10] Co-Z Development Corp. The Cozy Mark IV - Plans - Section I. Distributed to buyers only, December 1995.

[11] The Dow Chemical Company. STYROFOAM^{TM} panel core 20 freezer extruded polytstyrene foam insulation. Published on website, `www.dupont.com/content/dam/Dupont2.0/Products/Performance-Building-Solutions/literature/179-08123.pdf`. Product information.

[12] E. Cetinsoy et al. Design and construction of a novel quad tilt-wing UAV. *Mechatronics*, 22(6): 723–745, 2012. DOI:10.1016/j.mechatronics.2012.03.003.

[13] EASA. Notice of Proposed Amendment 2017-05 (A). Published on the EASA website, www.easa.europa.eu/document-library/notices-of-proposed-amendment/npa-2017-05, 2017.

[14] EASA. Opinion No 01/2018. Published on the EASA website, `www.easa.europa.eu/document-library/opinions/opinion-012018`, 2018.

[15] Evonik Resource Efficiency GmbH . Product Information ROHACELL ®. Published on website, `https://www.rohacell.com/product/peek-industrial/downloads/rohacell%20a%20product%20information.pdf`, 2019. Datasheet.

[16] Diab Group. Divinycell P, Technical Data. Published on website, `https://www.diabgroup.com/~/media/Files/Products/Core-material-products-English/P%20September%202018%20rev27%20SI.pdf`, 2018. Datasheet.

[17] S. Gudmundsson. *General Aviation Aircraft Design*. Butterworth-Heinemann, first edition, 2014.

[18] Gurit. Gurit® PVC structural foam core. Published on website, `www.gurit.com/-/media/Gurit/Datasheets/gurit-pvc.pdf`, 2018. Full general datasheet.

[19] Guy Gratton. *Initial Airworthiness*. Springer, 2018. ISBN 978-3-319-11409-5. DOI:10.1007/978-3-319-11409-5.

[20] R. Harshe. A review on advanced out-of-autoclave composites processing. *Advances in composite materials for structural applications*, 95(3):207–220, 2015. ISNN: 0970-4140.

[21] R.C. Hibbeler. *Mechanics of materials*. Prentice Hall, eight edition in si units edition, 2011.

[22] Suong V. Hoa. Comprehensive Composite Materials II. *Reference Module in Materials Science and Materials Engineering*, 2:1–23, 2018. Ch. 2.1 DOI: 10.1016/B978-0-12-803581-8.10074-8.

[23] JARUS. CS-LUAS Recommendations for Certification Specification for Light Unmanned Aeroplane Systems. Published on the JARUS website, 23-12-2016.

[24] JARUS. Certification Specifications for Light Unmanned Rotorcraft Systems (CS-LURS). Published on the JARUS website, 30-10-2010.

[25] JARUS. Recommendations for Certification Specification for Unmanned Aircraft Systems. Obtained per email, February 2019. Draft version, available for external consultation.

[26] Christos Kassapoglou. *Design and Analysis of Composite Structures*. John Wiley & Sons Ltd, 2nd edition edition, 2013.

[27] Sotiris Koussios. 11. interlaminar stresses design rules 2018. University lecture, 2018. Lecture slides.

[28] G.A. Kardomateas L.A. Carlsson. *Structural and Failure Mechanics of Sandwich Composites*, volume 121 of *Solid Mechanics and its Applications*. Springer, 2011. DOI: 10.1007/978-1-4020-3225-7.

[29] L.A. Khan, A.H. Mahmood, Z. Khan. Post curing effect of poly epoxy on visco-elastic and mechanical properties of different sandwich structures. *Polymer Composites*, 34(4):477–481, 2013. DOI: 10.1002/pc.22436.

[30] L.A. Khan et al. Cure characterization of Cycom 977-2A carbon/epoxy composites for quickstep processing. *Polymer Engineering and Science*, 54(4):887–898, 2014. DOI: 10.1002/pen.23629.

[31] Koji Muraoka, Noriaki Okada, and Daisuke Kubo. Quad tilt wing vtol uav: Aerodynamic characteristics and prototype flight test. 04 2009. ISBN 978-1-60086-979-2. doi: DOI:10.2514/6.2009-1834\href{https://doi.org/10.2514/6.2009-1834}{10.2514/6.2009-1834}. ISBN: 978-1-60086-979-2, DOI: 10.2514/6.2009-1834.

[32] Micheal C. Y. Niu. *Airframe stress analysis and sizing*. Hong Kong Conmilit Press Limited, first edition, 1997.

[33] William Norton. *Vought/Hiller/Ryan XC-142A Tiltwing VSTOL Transport*. Steve Ginter, May 2006.

[34] Hans Poulis. Lecture series: Adhesive Bonding, as part of the AE4ASM107 Joining course. University Lecture, 2017.

[35] R.Boerma. Bird strike analysis on loaded structures and the CTO challenge, 2018. Internship report.

[36] Robert M. Jones. *Mechanics of Composite materials*. Taylor & Francis Inc., second edition, 1999.

[37] U. Mbanefo R.P. Ley, W. Lin. Facesheet wrinkling in sandwich structures. NASA Technical Reports Server, January 1991. Northrop Grumman Corp, report: NASA/CR-1999-208994.

[38] B. Rutan. *Moldless composite homebuilt sandwich aircraft construction*. Rutan Aircraft Factory Inc., third edition, 1983.

[39] Rutan Aircraft Factory. Structure.PDF, 1996. available on the Rutan Aircraft Factory CD-ROM Encyclopedia.

[40] Dr J. Schlimbach. Presentation: OOA Manufacturing - An industrial perspective of Quickstep. Presentation available on `www.youtube.com/watch?v=lrhfKcx9A5A`. Retreived on 6/02/2019.

[41] R. E. Sheldahl. *Aerodynamic Characteristics of Seven Symmetrical Airfoil Sections Through 180-Degree Angle of Attack for Use in Aerodynamic Analysis of Vertical Axis Wind Turbines*. Sandia National Laboratories, March 1981.

[42] A. Brent Strong. *Fundamentals of Composites Manufacturing - Materials, Methods, and Applications (2nd Edition)*. Society of Manufacturing Engineers (SME), 2008. ISBN 978-0-87263-854-9.

[43] The European Commission. Legislation. *Official Journal of the European Union*, 62(L152), 2019.

[44] The European Parliamant and the Council of the European Union. Regulation (EC) No216/2008. Published on EUR-Lex, `www.eur-lex.europa.eu/eli/reg/2008/216/oj`, 2008.

[45] T.H.G. Megson. *Aircraft Structures for Engineering Students*. Butterworth-Heinemann, fifth edition, 2013.

[46] Yaping Wu, Yuanlin Zhu, Yuanming Lai, Xuefu Zhang, and Shizhong Liu. Analysis of thin-walled composite box beam under torsional load without external restraint. *Thin-Walled Structures*, 40(4):385–397, 2002. ISSN 02638231. DOI: 10.1016/S0263-8231(01)00064-7.

[47] A. Rotem Z. Hashin. A fatigue failure criterion for fiber reinforced materials. *Journal of Composite Materials*, 7:448–464, 1973. doi: DOI:\href{https://doi.org/10.1177/002199837300700404}{10.1177/002199837300700404}. URL `https://doi.org/10.1177/002199837300700404`. DOI: 10.1177/002199837300700404.

A

Material testing

This appendix describes the steps taken to obtain representative material and lamina data of three types of fibre glass impregnated with a thermoset epoxy matrix. The properties that need to be determined are:

- X_t, tensile strength in fibre direction (0 degrees)
- X_c, compressive strength in fibre direction (0 degrees)
- Y_t, tensile strength in transverse direction (90 degrees)
- Y_c, compressive strength in transverse direction (90 degrees)
- S, shear strength

Furthermore the stiffnesses E_x, E_y and G_{xy} and Poisson's ratios need to be known. The determined properties are used in the calculation of the laminate properties in the structural analysis of chapter 9.

A.1. Methodology

Three different testing methods were used to determine the in-plane properties of the composites. The tests were:

ASTM D3039M [6]	Tensile testing
ASTM D6641M [5]	Compression testing
ASTM D3518M [7]	In-plane shear testing

A.1.1. ASTM D3039-17 Tensile testing

In this test a coupon of 250mm x 25mm is tested in tension until failure. A bi-directional extensometer was used to determine the strain accurately in longitudinal and transverse direction. With both longitudinal and transverse strain the Poisson's ratio of the lamina/laminate can be determined. Before failure the extensometer was manually removed to prevent damage. The rest of the test was continued with the strain determined from the bench displacement. See the ASTM standerd [6] for more information. A rate of 1 mm/ minute was used. This and all other tests were performed at room temperature (23 degC and 50 % humidity).

A.1.2. ASTM D6641 Compression testing

A miniature version of the D6641 compression fixture was available for compression testing. The smaller fixture required 80mm x 13mm specimen where the standard size D6641 fixture used 140mm x 13mm samples [5]. Due to this small size no strain gauges could be fitted and all data was determined by the strain derived from the bench displacement. If a bigger fixture was used two strain gauges, one on either side of the specimen, could be used to determine if buckling would occur before compressive failure. As the specimen thickness was prepared to prevent buckling when tested with the normal size ASTM D6641 fixture no buckling will occur in the miniature D6641 compression fixture with the smaller gauge length.

A.1.3. ASTM 3518M In-plane shear testing

The same fixture and specimen size is used for in-plane-shear tests as for the ASTM D3039 tests. Also the bi-axial extensometer was used to determine the longitudinal and transverse strain, from which the shear strain can be determined by subtracting the longitudinal strain from the transverse strain as given in the ASTM [7]:

$$\gamma = \epsilon_{y_i} - \epsilon_{x_i} \tag{A.1}$$

After removal of the extensometer no strain data was available except for the longitudinal strain determined by bench displacement. The maximum shear strength was determined by using the following relation:

$$\tau_{12} = \frac{P_{max}}{2A} \tag{A.2}$$

Where P_{max} is the maximum load on the specimen below 5% engineering shear and A is the average cross-sectional area.

A.2. Production of specimens

The three glass fibre materials that were chosen are:

- Interglass 92110 - bi-directional 163 g/m^2
- Interglass 92125 - bi-directional 280 g/m^2
- Interglass 92145 - unidirectional 220 g/m^2

The fibres will be embedded in an aviation approved thermoset epoxy:

- Resin: EPIKOTE LR285
- Hardener: EPIKURE LR285

The resin and hardener were mixed in a ratio of 100 to 40 by weight (resin-hardener respectively).

The coupons required for the tests can be seen in table A.1. The choice for the tests was straight forward as the ASTM 3039M and ASTM 6641M are standard tests and the fixtures were available. For shear testing the ASTM 7078M fixture would be preferred as shear testing with unidirectional material in the tensile test fixture (ASTM 3518M) would not result in the most accurate results. Unfortunately no good fixtures were available and hence a ±45 layup was chosen to be tested with the ASTM 3518. Laminates with ±45 degree layups can be tested properly with this standard.

Table A.1: Required test coupons

Material	Tensile (250x25mm) ASTM 3039M	Compressive (140x13mm) ASTM 6641M	Shear (250x25mm) ASTM 3518M
Interglas 92110 BID	5x $[(0/90)_5]$	5x $[(0/90)_{12}]$	5x $[(+45/-45)_5]$
Interglass 92125 BID	5x $[(0/90)_5]$	5x $[(0/90)_8]$	5x $[(+45/-45)_5]$
Interglass 92145 UND	5x $[0_5]$	5x $[0_9]$	5x $[+45,-45]_3$
	5x $[90_5]$	5x $[90_9]$	-

The assumption is made that the bi-directional cloth has the same properties in the 0 degree direction as in the 90 degree direction. Therefore only 0 degree specimens are required for the specimen with bidirectional cloth. For a proper material characterisation both the 0 and 90 degree set must be tested, as well as an enlarged sample set to improve the observed significance level.

Four laminates were produced by hand layup, consisting of all the layups specified above. Three panels were made according to figure A.1. Locally additional plies were added to increase the thickness of the laminates to prevent buckling during the compression testing. The thicknesses for the nominal panels are 0.9, 1.2 and 1.5 mm for the Interglass 92110, 92145 and 92125 respectively. With additional plies the thicknesses became 2.3, 2.2 and 2.5 mm thick for the compression samples. The shear test samples were created from the nominal panels and were rotated by 45 degrees. For the UND shear tests a separate panel was produced with six layers of unidirectional fibres of ± 45 degrees as the ASTM 3518 required a plus and minus 45 degree direction.

An additional smaller plate was created with left over material to simulate a possible skin laminate made with one layer of 92145 under zero degrees and one layer of 92110 under 45 degrees. Locally additional plies were placed to yield additional thickness for the compression samples.

The laminates were cured without the assistance of a vacuum as the mouldless composite design does not use a vacuum. Henceforth material properties represent the absolute minimum values that can be obtained with this material during the construction of the prototype. With the assistance of the vacuum a higher fibre volume fractions and hence higher strengths can be obtained.

After curing the panels were cut a couple of weeks later. The material was rough cut on the band saw and cut to final dimensions with an accurate diamond blade to leave a smooth edge.

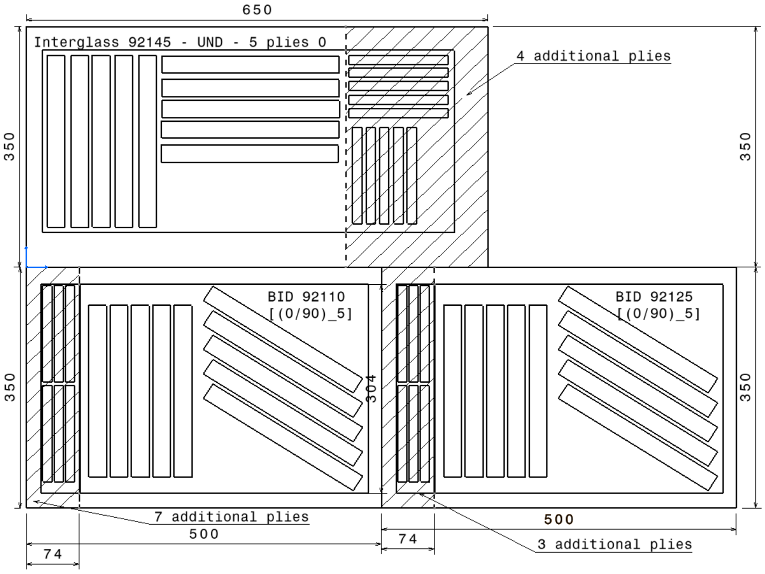

Figure A.1: Laminate sizes required for the different reinforcements for the required coupons.

A.2.1. Laminates

With the obtained data the strength and stiffness of arbitrary laminates can be determined by means of the classical lamination theory. An additional laminate was made which was deemed a possible candidate (as sandwich face sheets), consisting of two layers: one layer of 92145 UND under zero degrees and one layer of 92110 BID under 45 degrees. Four tensile specimen were produced such that predictions could be verified.

All the laminates were hand laminated on a flat surface. With a squeegee the excess resin was removed. No vacuum pressure was used during curing. The date of manufacturing was the 15th of

May 2019. The quality of the laminates is deemed adequate an not exceeding the quality that can be obtained during production. Hence the obtained data is deemed conservative.

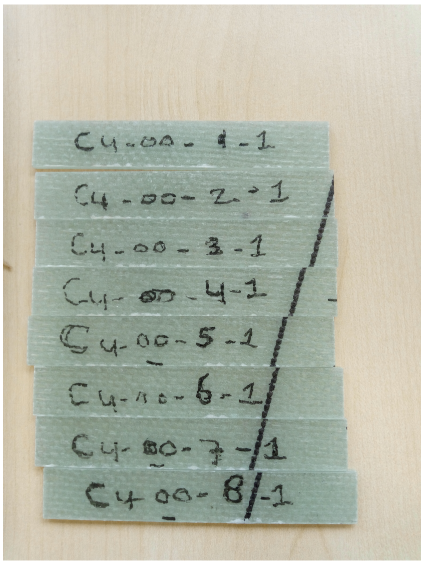

Figure A.2: Compression (Interglass 92145 - 0 degree) samples ready for testing.

A.3. Testing and results

The testing of the specimens was conducted on: 5 Juli 2019 and 8 Juli 2019 at the material laboratory at Fokker Hoogeveen. During the testing the temperature and humidity were 23 degrees Celcius and 52 % respectively. The test bench was a Instron 5982 connected to the Bluehill 3 software. For measuring the sample thickness and width digital callipers were used which automatically transferred the results to the software.

In total twelve different tests were performed, 5 tensile tests, 4 compression tests and 3 shear tests. No tabs were used during all tests. In hindsight paper tabs should have been used as some quite some samples failed in the grip area.

A.3.1. ASTM D3039-17 Tensile testing

The tensile tests were performed on the tensile fixture which gripped the specimens with hydraulic clamps. Especially for the tensile tests on the 90 degree unidirectional specimen the high clamping force was reduced in order to prevent grip early failure within the grip area. However no real reduction was found. Paper tabs would be beneficial during these tests to introduce the load more evenly. See figure A.3a for a specimen loaded during tensile testing.

The testing of the 0 degree specimens unidirectional samples resulted in explosive failures where the failure propagated along multiple paths longitudinal direction spanning from grip to grip. One specimens was omitted to the premature failure in the clamp area.

The fifth sample during the Interglass 92125 failed due to a local thickness increase of a additional fibre in the grip area causing high stress concentrations. This sample was omitted.

A.3.2. ASTM D6641 Compression testing

The compression tests were performed on a miniature ASTM 6641 fixture, and hence shorter samples were required. No strain measurement was available due since no strain gauges could be located in between the fixtures. Hence the failure strain and stiffness are less reliable then the values from the tensile testing. Furthermore no tabs were used. Especially at the 0 degree unidirectional

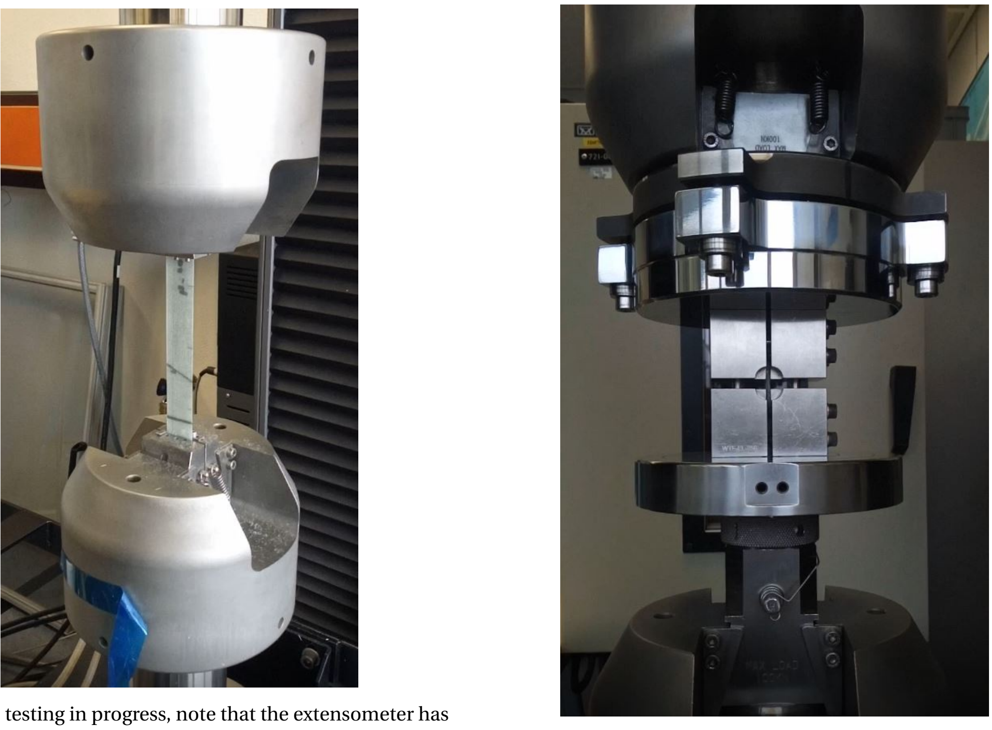

(a) Tensile testing in progress, note that the extensometer has already been removed.

(b) Compression testing in progress.

Figure A.3: Tensile and compression testing

specimens some specimens failed within the grip area. For the compression testing setup see figure A.3b.

A.3.3. ASTM 3518M In-plane shear testing

The in-plane-shear tests were performed on the same fixture as the one used for the tensile tests. In contrary to the tensile test, the shear test features an increase in the strain rate from 1mm/min to 10mm/min at a location of 1% strain. Large deformations occurred before final failure. As the bi-directional extensometer had to be removed the failure stress and failure load in tensile direction is determined. The shear stress is half the tensile load reached. See figure A.4 for the tensile versus strain data of the Interglass 92110 samples during the ASTM 3518M test. Note the high deformation before ultimate failure, which is common for in plane shear tests.

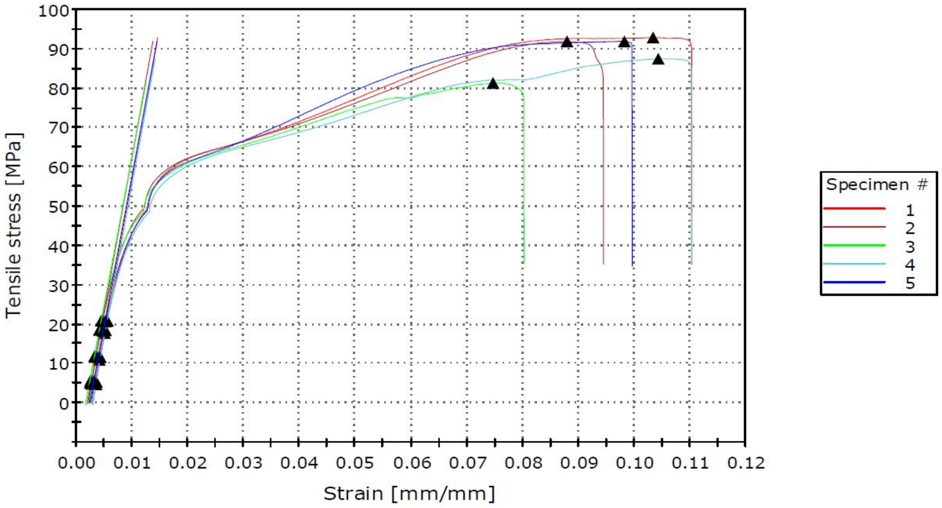

Figure A.4: ASTM 35108M In-Plane Shear testing. Tensile stress versus strain, note that the ultimate shear stress is half the ultimate tensile stress during this test.

A.4. Results

From each test a PDF test report was produced by the software as well as .CSV files of the individual samples containing all the load, stress and strain data. For brevity these reports are not included. A summary of all the relevant strength data can be seen in the following tables:

Table A.2: Material mean and minimum test values

	Mean values			Minimum values			Units
Material	Interglass 92110 BID	Interglass 92125 BID	Interglass 92145 UNI	Interglass 92110 BID	Interglass 92125 BID	Interglass 92145 UNI	
X_t	270.6	235.4	437.7	263.2	222.6	414.9	[MPa]
X_c	244.7	355.7	438.2	200.3	345.3	391.0	[MPa]
Y_t	270.6	235.4	32.6	263.2	222.6	28.0	[MPa]
Y_c	244.7	355.7	96.4	200.3	345.3	87.4	[MPa]
S	88.9	104.3	76.6	82.1	98.6	68.8	[MPa]
E_{x_t}	17.3	18.3	25.1	16.8	18.1	24.2	[GPa]
E_{x_c}	22.8	26.7	36.4	17.5	25.1	34.2	[GPa]
E_{y_t}	17.3	18.3	6.13	16.8	18.1	6.1	[GPa]
E_{y_c}	22.8	26.7	17.1	17.5	25.1	10.9	[GPa]
G	2.44	2.83	2.60	2.41	2.78	2.5	[GPa]
ν_{xy}	0.12	0.15	0.29	0.11	0.14	0.3	[-]
ν_{yx}	-	-	0.08	-	-	0.1	[-]
ν_{45}	0.59	0.58	0.57	0.57	0.56	0.5	[-]

A.5. Remarks

Not all specimens failed in gauge sections, especially the unidirectional sample testing. Since glass is a relatively low stiffness materials lower stiffness tabs such as paper tabs could be used next time to properly introduced the loads and reduce the scatter.

The specimens were made by means of hand layup, without the assistance of a vacuum. In combination with the ply thickness given by the seller the fibre volume contents were estimated to be between 31 and 35%. The material properties represent the minimum values attainable, improved processes should increase the strength of the specimen.

B

Creation of the flight envelope

In this appendix the creation of the flight envelope is detailed. The flight envelope is a diagram that plot load factor against airspeed. The flight envelope defines the boundary on the combination of airspeed and load factor for which the strength of structure must be shown to comply with.

The flight loads from the CS-LUAS are only applicable for fixed-wing aircraft, hence they only apply to the cruise phase of the flight. The flight envelope is a combined diagram of the manoeuvre diagram and the gust loading diagram. Background information on the flight envelopes can be found in a variety of literature such as Gudmundsson [17, Sec. 16.4], Megson [45, Ch. 14], Niu [32, Sec. 3.4] and of course CS-LUAS.333 [23] itself.

The **manoeuvre diagram** is bounded by the minimum and maximum load factors obtained from CS-LUAS.337 (Limit Manoeuvring Load factors), the dive speed and the accelerated stall boundary. The accelerated stall limit is derived from a rewritten form of the lift equation:

$$n_{acc_{stall}} = V^2 / V_{stall}^2 \tag{B.1}$$

Since the stall lift coefficient for normal and inverted flight are different, the stall speeds are also different. Resulting in different accelerated stall limits for positive and negative load factors.

The **gust envelope** is calculated at the chosen cruise speed, V_c, and the dive speed, V_d. In this case V_c is chosen to be 42 m/s and V_d to be 50 m/s. The V_{ne} is 45 m/s which is just a little less than $V_d/1.1$. Between the cruise and dive speed the gust load factor can be linearly interpolated. CS-LUAS.333 refers to the AMC (Acceptable Means of Compliance) LUAS.341 Gust Load Factors in which the acceptable means of compliance to CS.LUAS.333 is given. *"In absence of a more rational analysis the gust load factors must be compute as follows:"*

$$n = 1 + \frac{k_g \rho_0 U de V C_{L_\alpha}}{2(W/S)} \tag{B.2}$$

Where k_g is the gust alleviation factor:

$$kg = \frac{0.88\mu g}{5.3 + \mu g} \tag{B.3}$$

For canard and twin wing aircraft a k_g of 1.2 can be used in absence of a more rational analysis [23], or the above equation can be used as long as the equation above yields conservative factors. For the time being $k_g = 1.2$ is used to be conservative. In the above equation μg is the aeroplane mass ratio and is given as:

$$\mu g = \frac{2(W/S)}{\underline{\rho} \bar{C} C_{L_\alpha} g} \tag{B.4}$$

Where ρ is the density of the air, $\overline{C}$ is the mean geometric chord length and g is the gravitational acceleration.

Now that the manoeuvre and gust loading boundaries are determined the flight envelope can be assembled. See figure 8.8 & 8.9 (or B.2 & B.1) for the flight envelopes at OEW & MTOW respectively. The green shaded area is the normal operating regime up until the design cruise speed of the aircraft. The yellow area is the area from V_c until the never exceed speed (V_{NE}). The red area spans from V_{NE} to dive speed (V_D). The blue area is the flap extension area. No flaps are used in the design but the wing rotation mechanism is in this case counted as a high lift device.

Now that the flight envelope's are determined an interesting observation can be made. The maximum load achievable is only attainable at airspeeds above the never exceed speed. Below this speed the load is limited by the accelerated stall boundary. To reach the maximum loads is not simple as the hydrogen fuel cells do not provide enough power to fly at such speeds in level flight. The maximum speed achievable on hydrogen power is around 30 to 35 m/s. Only in a dive or on battery power can these speeds be possibly achieved where the maximum load can be reached. Gusts at these cruise velocities will not overstress the aircraft since the wings will stall before they can reach the loads factors that cause an overstress. The highest load factors are determined by gust load factors and result in a maximum positive load factor of 4.98 and a maximum negative load factor of -3.18 for flying at OEW. For flights at MTOW the maximum load factors are 4.07 & -2.48 at speeds above V_{NE}.

For the sake of completeness the flight envelopes are displayed again in figure B.1 and B.2.

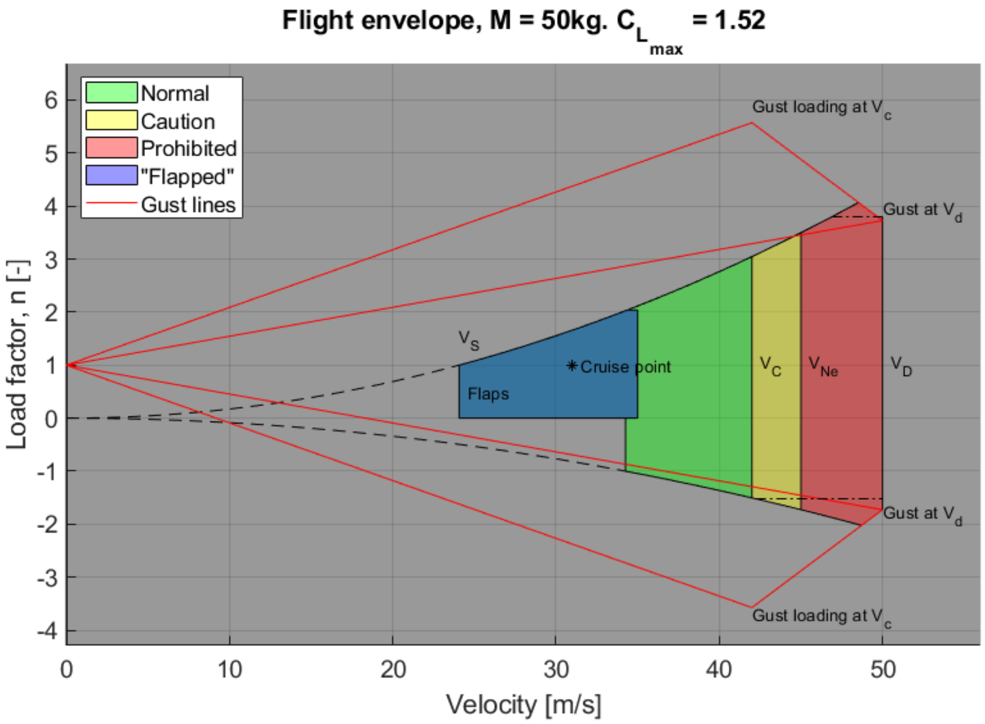

Figure B.1: Flight envelope for MTOW. Including manoeuvring load diagram and gust loading diagram.

B.1. Maximum wing loads

To calculate the loads on the individual wings, not the aircraft maximum lift coefficient is used but the maximum lift coefficient of the canard and wing respectively. The maximum lift coefficients for both wings are estimated to be 1.76 each.

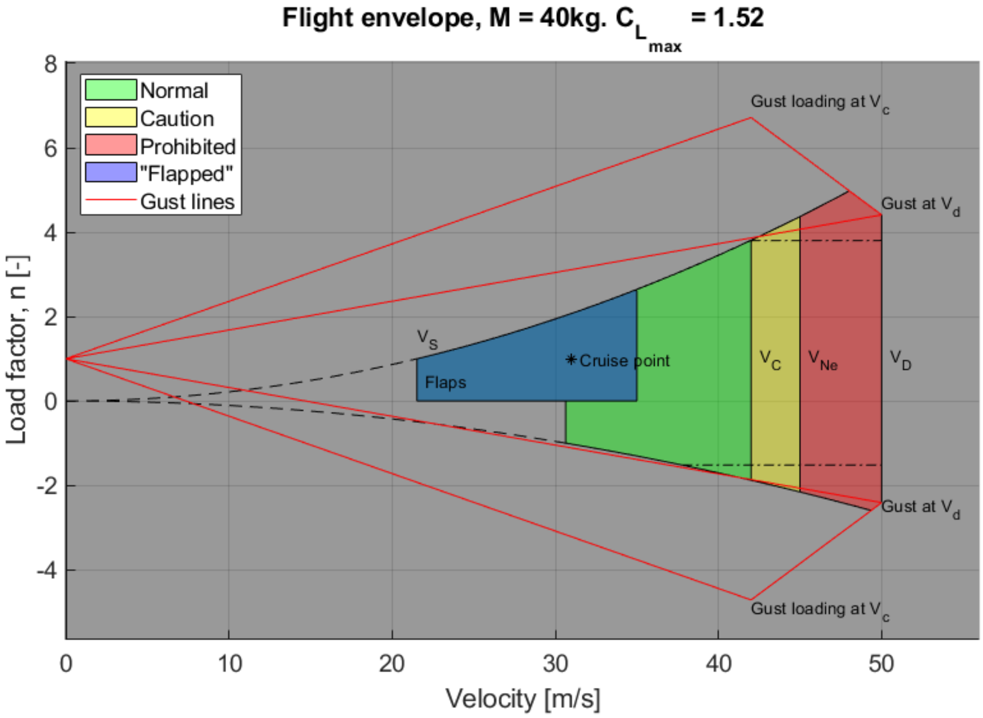

Figure B.2: Flight envelope for empty weight. Including manoeuvring load diagram and gust loading diagram. Note the higher gust loading due to the decreased wing loading.

C

Post-stall evaluation of FlightStream

During the transition flight phase the airflow is separated from the airfoil. This region, the post-stall region, is governed by separated flow and is more difficult to predict. In this appendix the FlightStream vorticity solver is compared against wind tunnel data to observe if the software captures the post stall aerodynamics effect and can predict proper lift coefficients.

The report by Naik and Ostowari [1985] on the *"Post-Stall Wind Tunnel Data for NACA 44XX Series Airfoil Sections"* [8] is used to compare the data on an NACA 4418 airfoil. The report by Sheldahl and Klimas [1981] on the *"Aerodynamic Characteristics of Seven Symmetrical Airfoil Sections Through 180-Degree Angle of Attack for Use in Aerodynamic Analysis of Vertical Axis Wind Turbines"* [41] is used to compare the data on an NACA 0015 airfoil.

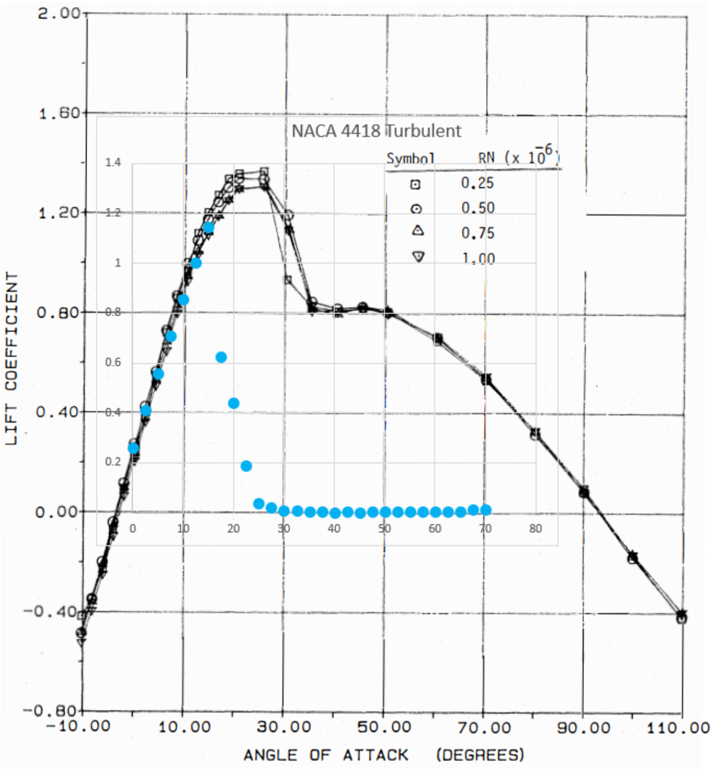

Figure C.1: Comparison of FlightStream 11.2 analysis of a NACA 4418 wing A=50 & Re = 500000 with reference data A = 9. Windtunnel data: [8]

C.1. Method

This section describes the method followed used to obtain the post-stall lift coefficient data.

In OpenVSP a rectangluar wing with a 200 mm chord and a 5000 mm semi span was created. Which results in an aspect ratio of 50 for the complete wing. This high aspect ratio was used to represent a 2D airflow as close as possible. An STL file was used to transfer the geometry in FlightStream. A trailing edge was defined on the trailing edge of the wing and the solver settings were adjusted such that 36.52 m/s would result in a Reynolds number of 500000. The turbulent correction model and the flow-separation options were enabled. The solver sweeper was used to sweep from 0 to 70 degrees in steps of 2.5 degrees. Each configuration took around 10 iterations and 15 seconds to solve using 8 logic processors.

A reference velocity of $\sqrt{\frac{2}{\rho}} = 1.2778$ was used to set the output of the lift in Newtons. The obtained results were stored in a .txt file which were read in Excel for the post processing. Lift coefficients were obtained by dividing the lift by $\frac{1}{2}\rho v^2 S$. The graph sizes were adjusted to fit on top of the references figures.

[1]

C.2. Observations

The following observations can be made from the results in figure C.1 & C.2: The lift curve slopes are under predicted. For comparable aspect ratios in figure C.1 the aspect ratio of 9 provides the best fit of the data. But is still does under predict the stall angle and hence the stall lift coefficient. The post-stall lift of the airfoil is not recovered.

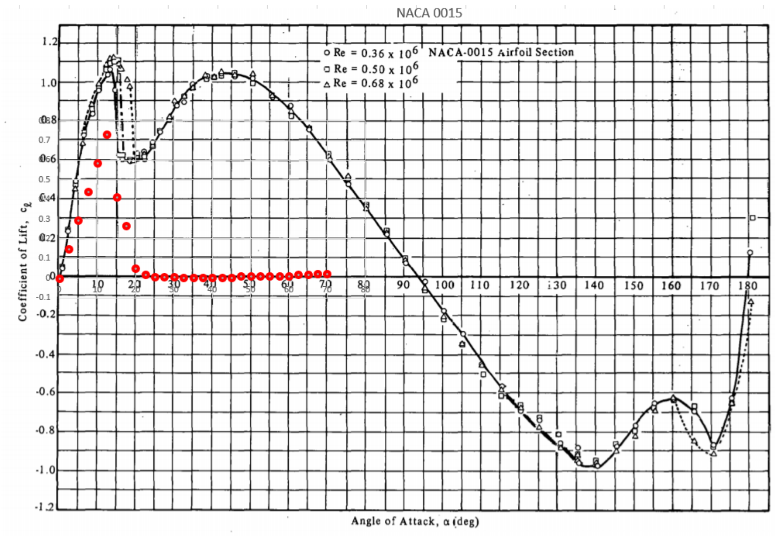

Figure C.2: Comparison of FlightStream 11.2 analysis of a NACA 0015 wing A=50 & Re = 500000 with reference data. Windtunnel data: [41]

C.3. Conclusion

The FlightStream vorticity solver does predict stall but it does not predict the expected lift at high post stall angles. Therefore the post-stall analyses with the FlightStream solver are unfit for determining the loads on the structure during transition.

---

[1] The FlightStream files of the simulation are: "$NACA0015\_PostStall\_Analysis.fsm$" & "$NACA4418\_PostStall\_Analysis.fsm$".

The new FlightStream version 11.4 has an improved model which better predicts the post stall behaviour, it does however require a much more refined mesh. An investigation into the usability should be made. According to the manufacturers the post stall behaviour should be usable and only some non linear behaviour should still be modelled and could further improve the accuracy.

FlightStream version 11.6 continues to improve with an immersed boundary detection. This means that OpenVSP geometry can be used with no pre-processing. In previous version a proper, non-intersecting, model would be required. With the immersed boundary detection a wing inside the fuselage will be detected and that section will be ignored.

D

Classical Laminate Theory

This appendix details a short summary of the classical laminate theory. The classical laminate theory is a well known theory for calculating the behaviour of composite laminates and it described in may works such as [26] & [36].

In the classical lamination theory it is assumed that the laminate is in a state of plane stress, i.e. all the stresses are in the plane of the laminate. Firstly the laminate stiffness matrix (C_0) must be calculated. This matrix relates the laminate strains to the stresses in the laminate:

$$\begin{bmatrix} \sigma_x \\ \sigma_y \\ \tau_{xy} \end{bmatrix} = \begin{bmatrix} \frac{E_x}{1-\nu_{xy}\nu_{yx}} & \frac{\nu_{xy}E_y}{1-\nu_{xy}\nu_{yx}} & 0 \\ \frac{\nu_{xy}E_y}{1-\nu_{xy}\nu_{yx}} & \frac{E_y}{1-\nu_{xy}\nu_{yx}} & 0 \\ 0 & 0 & G_{xy} \end{bmatrix} \begin{bmatrix} \epsilon_x \\ \epsilon_y \\ \gamma_{xy} \end{bmatrix} \tag{D.1}$$

Next the laminate stiffness matrix is rotated to yield the rotated stiffness matrix (C_θ):

$$\overline{C}_\theta = \overline{M C_0} \overline{M}^T \tag{D.2}$$

$$= \begin{bmatrix} m^2 & n^2 & 2mn \\ n^2 & m^2 & -2mn \\ -mn & mn & m^2-n^2 \end{bmatrix} \begin{bmatrix} \frac{E_x}{1-\nu_{xy}\nu_{yx}} & \frac{\nu_{xy}E_y}{1-\nu_{xy}\nu_{yx}} & 0 \\ \frac{\nu_{xy}E_y}{1-\nu_{xy}\nu_{yx}} & \frac{E_y}{1-\nu_{xy}\nu_{yx}} & 0 \\ 0 & 0 & G_{xy} \end{bmatrix} \begin{bmatrix} m^2 & n^2 & 2mn \\ n^2 & m^2 & -2mn \\ -mn & mn & m^2-n^2 \end{bmatrix}^T \tag{D.3}$$

Where m = $\cos(\theta)$ and n = $\sin(\theta)$.

Now the $\overline{A}$, $\overline{B}$, and $\overline{D}$ matrices are calculated by calculating the contribution of each ply in the laminate, where z_k & z_{k-1} are the location of the top and bottom of each respective ply.

$$\overline{A} = \sum_{k=1}^{n} \overline{C}_\theta \left(z_k - z_{k-1}\right) \tag{D.4}$$

$$\overline{B} = \sum_{k=1}^{n} \frac{\overline{C}_\theta}{2} \left(z_k^2 - z_{k-1}^2\right) \tag{D.5}$$

$$\overline{D} = \sum_{k=1}^{n} \frac{\overline{C}_\theta}{3} \left(z_k^3 - z_{k-1}^3\right) \tag{D.6}$$

(D.7)

The units of the matrices are $\overline{A}$ [N], $\overline{B}$ [Nmm], $\overline{D}$ [Nmm^2]. This results in three 3 by 3 matrices. The ABD matrix is formed from these three matrices and relates the mid-plane strains and curvatures to the loads on the laminate.

$$\begin{bmatrix} \overline{N} \\ \overline{M} \end{bmatrix} = \begin{bmatrix} \overline{A} & \overline{B} \\ \overline{B} & \overline{D} \end{bmatrix} \begin{bmatrix} \overline{\epsilon_0} \\ \overline{\kappa} \end{bmatrix} \tag{D.8}$$

As the loads are known on the laminate the inverse of the ABD matrix is required to calculate the strains and curvatures.

$$\begin{bmatrix} \overline{\epsilon_0} \\ \overline{\kappa} \end{bmatrix} = \begin{bmatrix} \overline{A} & \overline{B} \\ \overline{B} & \overline{D} \end{bmatrix}^{-1} \begin{bmatrix} \overline{N} \\ \overline{M} \end{bmatrix} \tag{D.9}$$

For small deflections the strain in each ply due to the curvature is linearly related to the distance from the mid-plane. Hence the individual ply strains can calculated by multiplying by:

$$\begin{bmatrix} \epsilon_x \\ \epsilon_y \\ \gamma_{xy} \end{bmatrix} = \begin{bmatrix} \epsilon_{x0} \\ \epsilon_{y0} \\ \gamma_{xy0} \end{bmatrix} + \frac{z_{k-1} + z_k}{2} \begin{bmatrix} \kappa_x \\ \kappa_y \\ \kappa_{xy} \end{bmatrix} \tag{D.10}$$

Now the strains need to be rotated in the coordinate system of the ply itself to obtain the strains in the fibre directions:

$$\begin{bmatrix} \epsilon_1 \\ \epsilon_2 \\ \gamma_{12} \end{bmatrix} = \begin{bmatrix} m^2 & n^2 & mn \\ n^2 & m^2 & -mn \\ -2mn & 2mn & m^2 - n^2 \end{bmatrix} \begin{bmatrix} \epsilon_x \\ \epsilon_y \\ \gamma_{xy} \end{bmatrix} \tag{D.11}$$

Such that consequently the stresses in fibre direction can be calculated:

$$\begin{bmatrix} \sigma_1 \\ \sigma_2 \\ \tau_{12} \end{bmatrix} = \overline{C_\theta} \begin{bmatrix} \epsilon_1 \\ \epsilon_2 \\ \gamma_{12} \end{bmatrix} \tag{D.12}$$

With the stresses known in the all the plies, the plies can be checked for failure by using the failure criterion described in section 9.1.5.

E

Additional graphs of chapter 8

This appendix contains the additional graphs of chapter 8 detailing all the load cases analysed in each load direction.

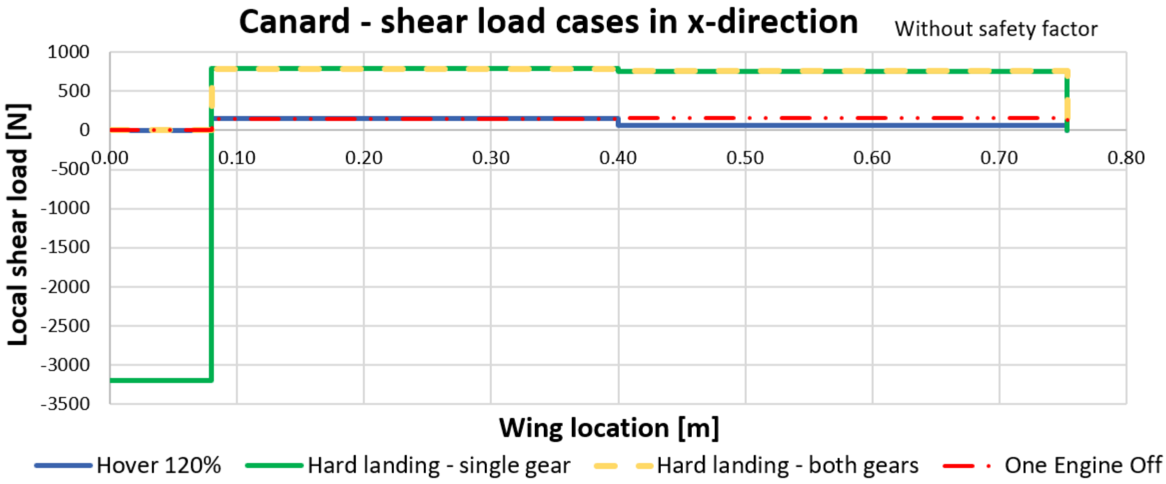

Figure E.1: Canard: Most critical shear load cases in the x-axis.

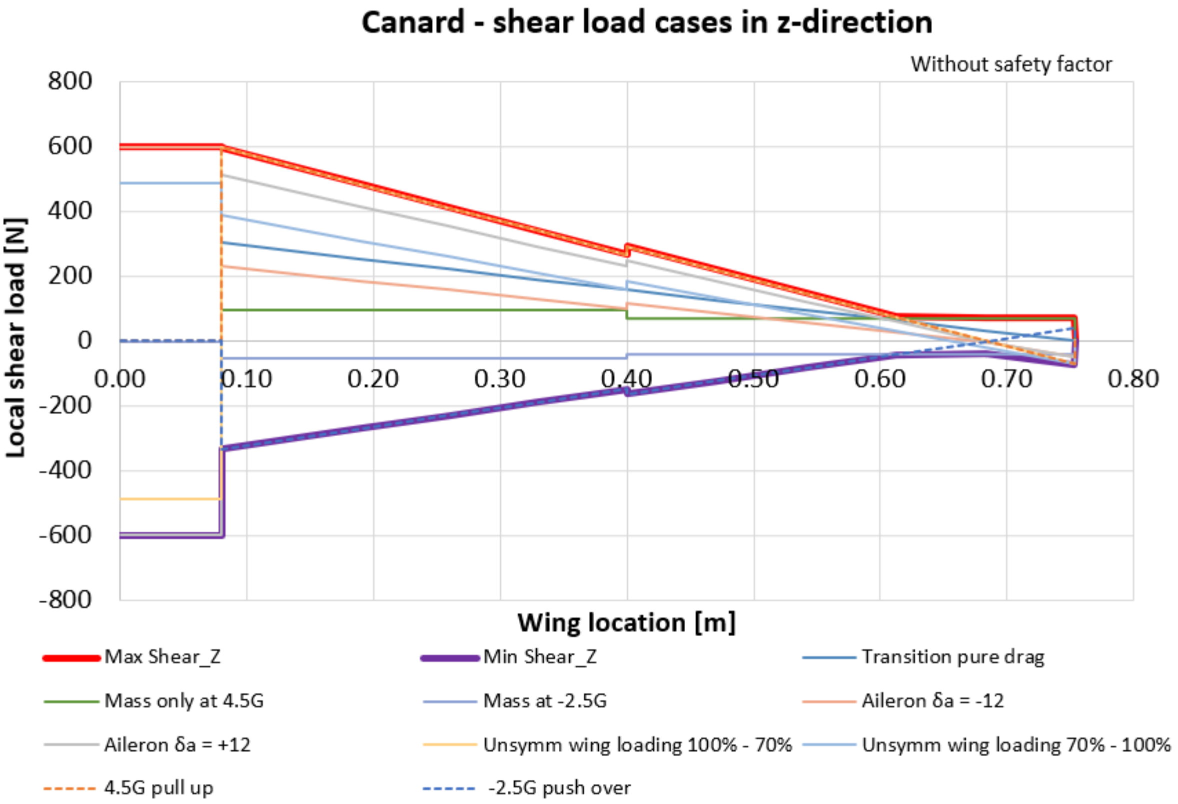

Figure E.2: Canard: Most critical shear load cases in the z-axis.

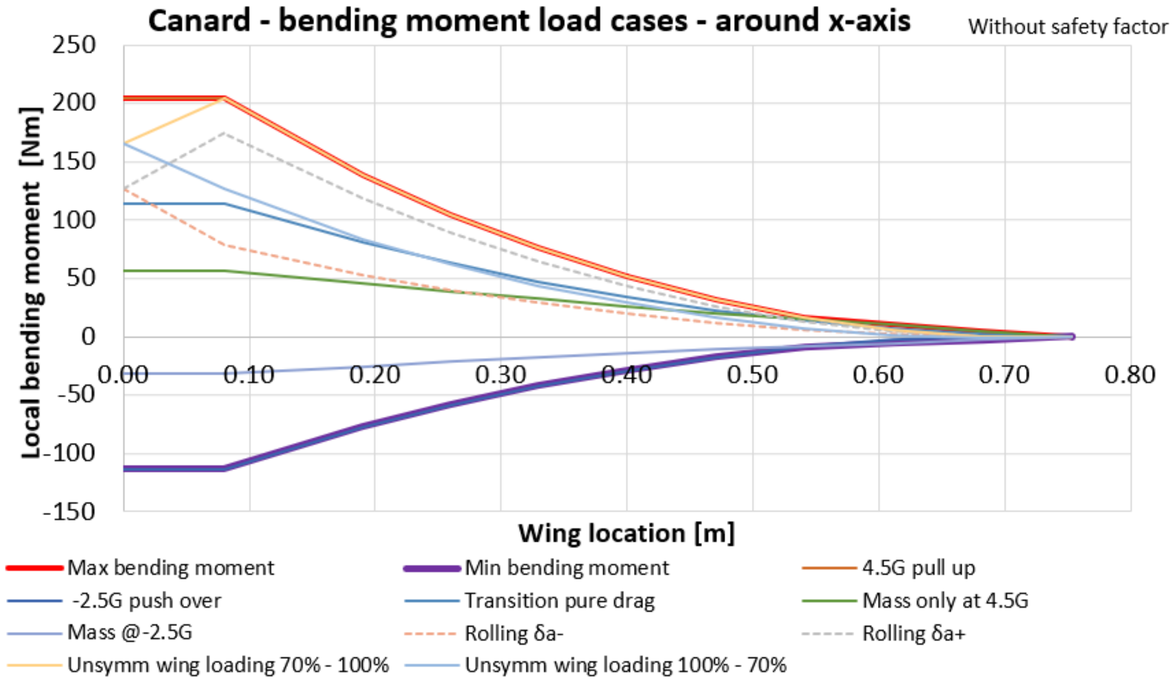

Figure E.3: Canard Wing: Most critical bending load cases around the x-axis.

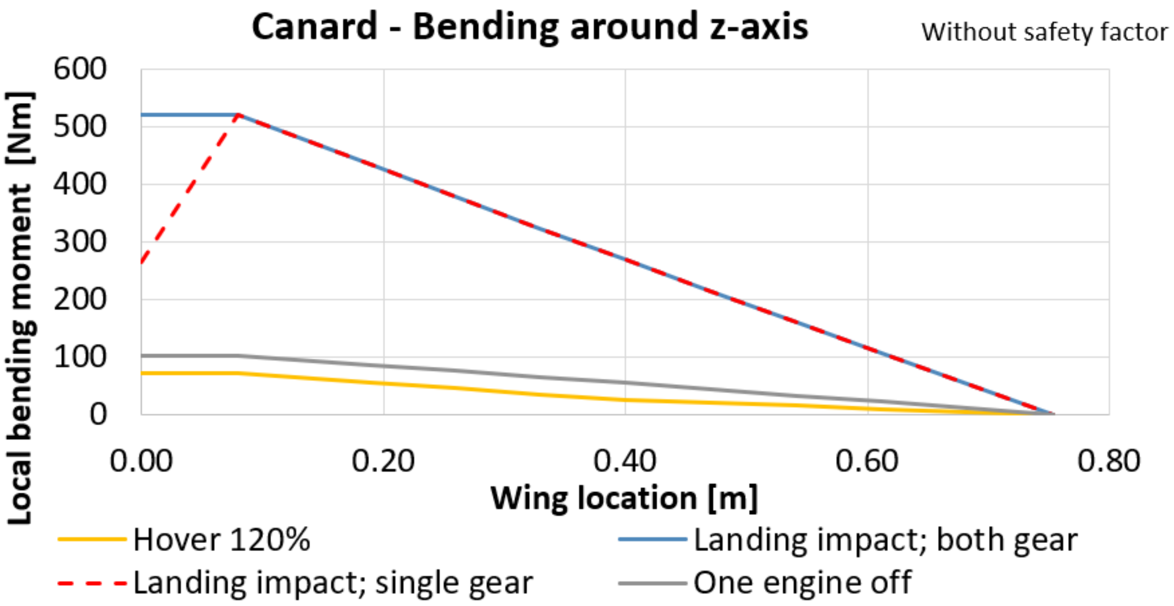

Figure E.4: Canard Wing: Most critical bending load cases around the x-axis.

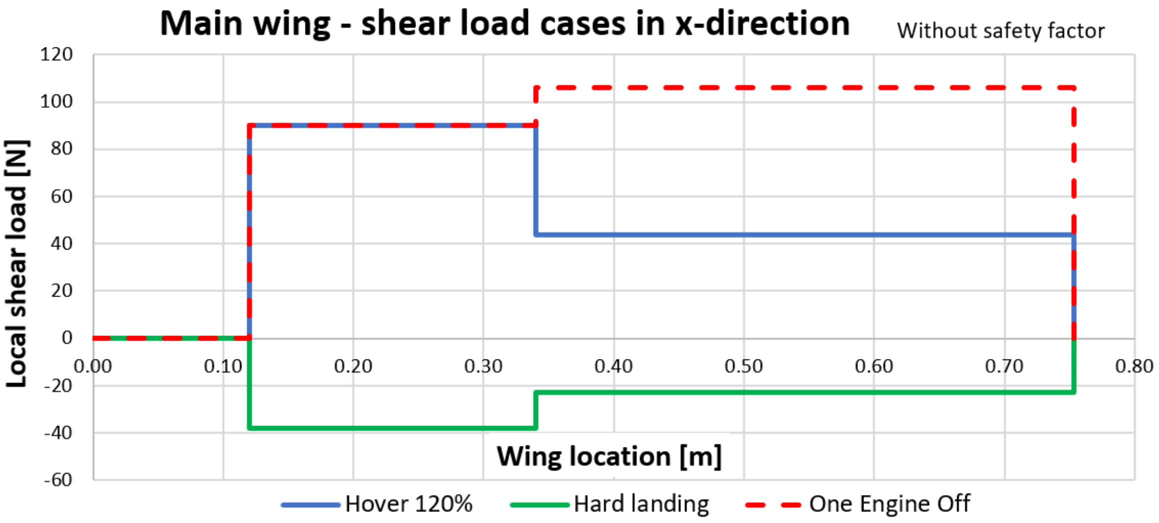

Figure E.5: Main Wing: Most critical shear load cases in the x-axis.

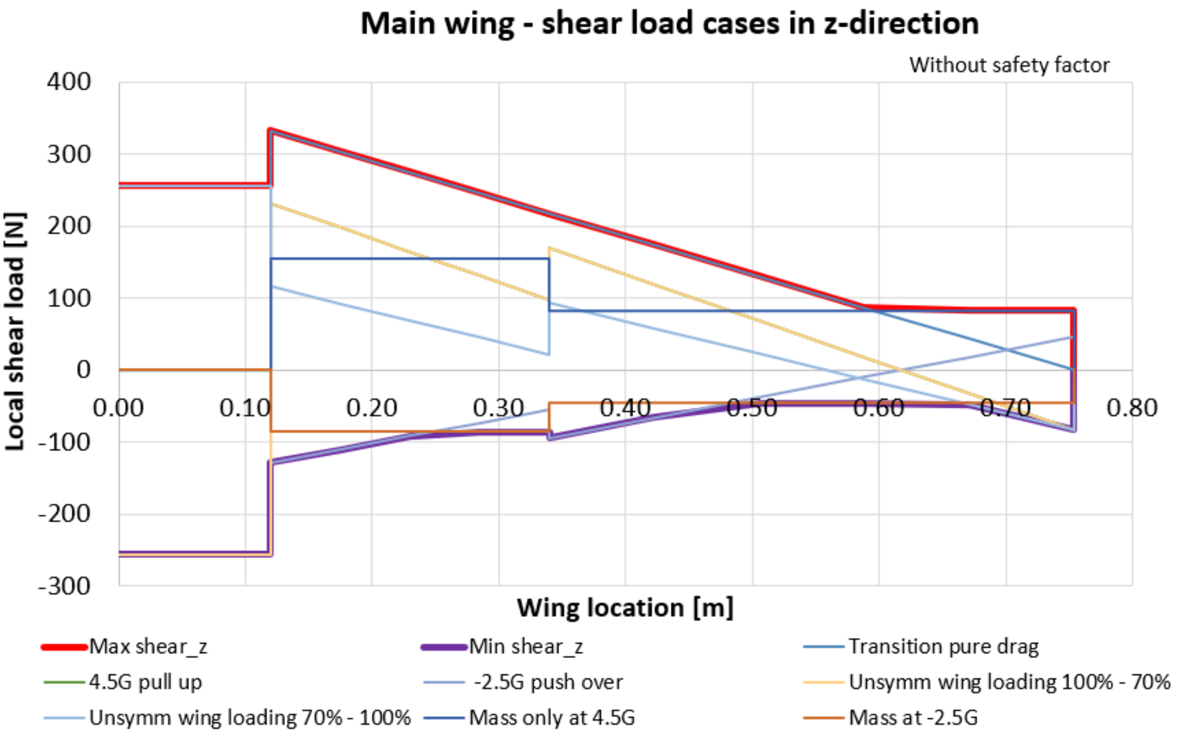

Figure E.6: Main Wing: Most critical shear load cases in the z-axis.

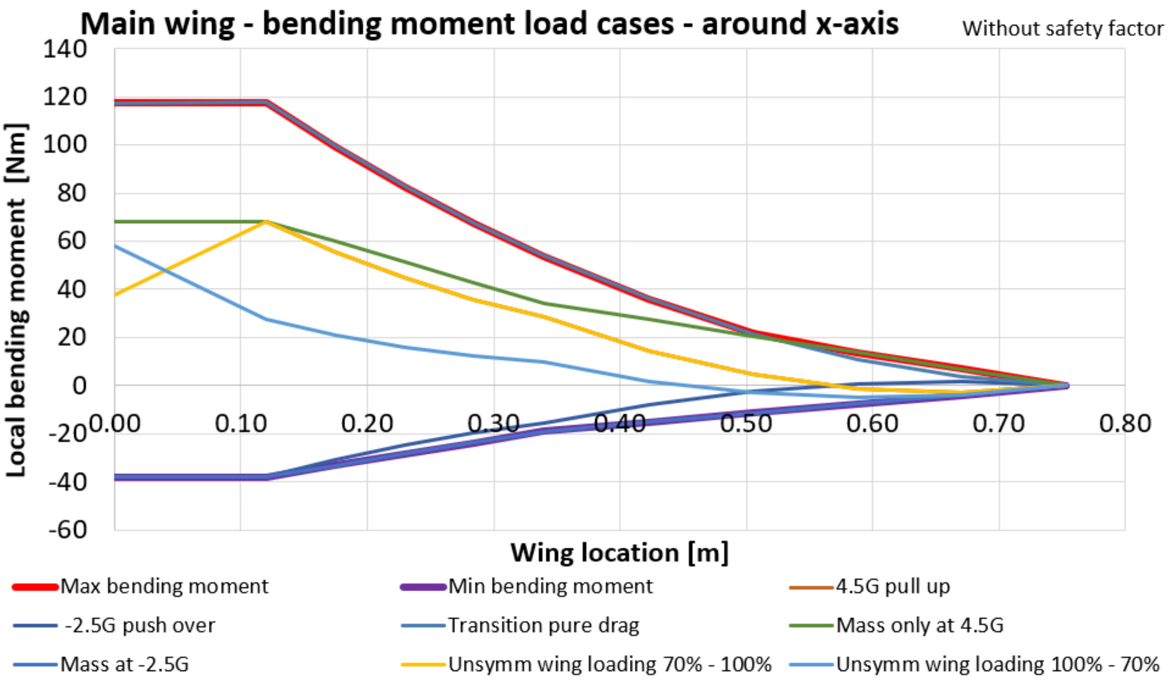

Figure E.7: Main Wing: Most critical bending load cases around the x-axis.

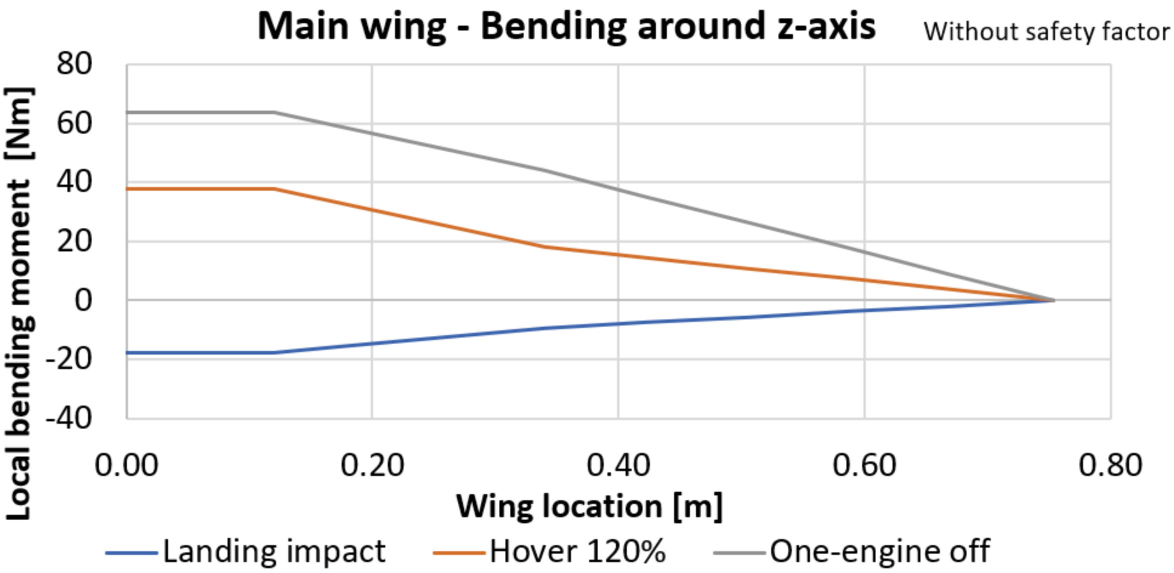

Figure E.8: Main Wing: Most critical bending load cases around the x-axis.